COMPREHENSIVE STUDY OF OPTIMAL SYNERGETIC SKIP ENTRIES WITH DYNAMIC THRUST VECTORING CONTROL

THESIS

Jeremiah M. Webb, First Lieutenant, USAF

AFIT-ENY-MS-19-M-251

DEPARTMENT OF THE AIR FORCE
AIR UNIVERSITY

AIR FORCE INSTITUTE OF TECHNOLOGY

Wright-Patterson Air Force Base, Ohio

AFIT-ENY-MS-19-M-251

COMPREHENSIVE STUDY OF OPTIMAL SYNERGETIC SKIP ENTRIES

WITH DYNAMIC THRUST VECTORING CONTROL

THESIS

Presented to the Faculty

Department of Aeronautics and Astronautics

Graduate School of Engineering and Management

Air Force Institute of Technology

Air University

Air Education and Training Command

in Partial Fulfillment of the Requirements for the

Degree of Master of Science in Astronautical Engineering

Jeremiah M. Webb, BS

First Lieutenant, USAF

21 March 2019

AFIT-ENY-MS-19-M-251

COMPREHENSIVE STUDY OF OPTIMAL SYNERGETIC SKIP ENTRIES

WITH DYNAMIC THRUST VECTORING CONTROL

Jeremiah M. Webb, BS
First Lieutenant, USAF

Approved:

_____   _____
Maj Robert Bettinger, PhD (Chairman)   Date

_____   _____
Lt Col Kirk Johnson, PhD (Member)   Date

_____   _____
Capt Joshuah Hess, PhD (Member)   Date

AFIT-ENY-MS-19-M-251

Abstract

The atmospheric skip entry has been studied since London's presentation in 1962 describing a more fuel efficient means of altering the orbital inclination of satellites. Since London, research over the decades since has traversed many aspects of this field with varying degrees of success. The present research employs the use of modern optimal control software, complex dynamics with minor simplifications, and thrust vectoring to re-approach the aerocruise atmospheric skip entry. Using the aerodynamics of the X-34, the aerocruise problem is first compared to the un-powered aeroglide where it is shown that the aerocruise is capable of increasing the inclination change by an average of $10°$, and can be used more effectively when constraints on heating and deceleration rates are applied. A typical assumption of aerocruise maneuvers, that thrust be opposite of drag proved to not be the optimal solution. Optimal thrust angle solutions tend to guide the thrust vector in the direction of the atmospheric turn, and approximately $10°$ in the direction of lift. This research shows that thrust vectoring could be utilized in trans-atmospheric vehicle (TAV) design to increase the inclination change during an atmospheric maneuver. In addition, various vehicle parameter changes are studied and their results analyzed for the purpose of TAV design. Compared to the exo-atmospheric plane change the thrust vectoring aerocruise grants an additional $28.3°$ of inclination change; a ΔV savings equivalent to $3.67\ km/s$.

Acknowledgements

Dad said, "Never do anything half-ass." May this body of work reflect my whole ass effort, and be dedicated to his memory. WRT 2/9/1971 - 5/15/2018

<div align="right">Jeremiah M. Webb</div>

Table of Contents

List of Figures

List of Tables

COMPREHENSIVE STUDY OF OPTIMAL SYNERGETIC SKIP ENTRIES
WITH DYNAMIC THRUST VECTORING CONTROL

I. Introduction

1.1   General Issue

Orbit determination and prediction of spacecraft in low Earth orbit (LEO) has become increasingly accurate since the mid-twentieth century. However, challenges to space operations persist in the form of collision risks with orbital debris and other resident space objects, as well as the prospects of operating in a contested space environment. For the latter, anti-satellite (ASAT) weapons pose a primary threat to space systems as demonstrated in 2007, when the Chinese intercepted and destroyed a weather satellite in LEO. [2]. More recently, the U.S Joint Chiefs of Staff Report on Space Operations called for protective measures against the threats that ASATs pose on LEO spacecraft [3]. Traditionally, spacecraft avoidance and evasion measures have traditionally been thought of as purely exo-atmospheric maneuvers with the primary means of maneuver delivering phasing or inclination change effects. When executed in vacuum inclination changes, become extortionate ΔV maneuvers. Since research began in the 1960's, the validity of performing trans-atmospheric maneuvers has been proven as a potential way to lower propellant costs.

The upper atmosphere offers conditions that, if exploited, can increase a spacecraft's maneuverability and decrease the overall ΔV expenditure. For purposes of this research, a sub-category of spacecraft that can perform these maneuvers will be called "trans-atmospheric vehicles" (TAVs) [4]. Specifically, TAVs are designed to conduct

missions in LEO and fly at hypersonic velocities within the atmosphere. TAVs have the ability to perform skip entries, a maneuver that lowers the perigee altitude of an orbit to skim the upper layers of the Earth's atmosphere where aerodynamic maneuvers can be used to alter orbital parameters of the initial orbit. Synergetic skip entries, refer to skip entries that also employ thrusting during the atmospheric portion of flight. Research in this area has primarily focused on control laws that involve the bank angle and angle of attack. The present research will add thrust cant angles to the control law with the ability to alter the direction of thrust referred to as *thrust vectoring*.

1.2 Research Motivation

TAVs have the potential to increase the uncertainty of orbit determination of low earth satellites. The present research was conducted to improve the simulation of synergetic skip entries to determine the full range of possibilities for such spacecraft. TAVs are famous for their unique aerodynamic characteristics defined by their slender body, and short wingspan [4]. The optimization of their design has obtained high lift, low drag characteristics perfecting their ability to make atmospheric re-entry maneuvers. In addition, these vehicles may benefit from thrust vectoring. Determining the potential of these maneuvers will be fulfilled by the following research objectives:

- Develop and verify a model that simulates re-entry trajectories. This model will be referred to as the *dynamics model*.

- Employing the use of GPOPS-II optimization software, determine the maximum inclination change that is achievable using the dynamics model. Compare skip entries to synergetic skip entries with thrust vectoring.

- Create a comprehensive study of synergetic skip entries with thrust vectoring that can be used in design considerations for TAVs. The study will include varying fuel mass, vehicle mass, specific impulse I_{sp}, maximum thrust, deceleration rate, heating rate, and total heat load.

- Compare and contrast synergetic skip entry thrust vectoring maneuvers to exo-atmospheric inclination change maneuvers considering both the de-orbit and re-orbit ΔV required.

1.3   Methodology

The dynamics model produces solutions by integrating six nonlinear, coupled ordinary differential equations that govern the kinetics and kinematics of orbital flight and atmospheric re-entry. As verification of the models accuracy, the Apollo-10 re-entry profile initial conditions will be used as inputs to the model, and the solution will be compared to the actual re-entry trajectory. After verification, the model will be transferred for use in GPOPS-II MATLAB® software where the TAV aerodynamics model will be used to analyze various constraint cases.

Based on a set of given, initial conditions an aerodynamic atmospheric turn performed during a skip entry will be simulated through the sensible atmosphere. The pre and post entry flight paths will not be simulated; however the flight path angle and altitude will be all be restricted to ensure realistic values of a skip entry are maintained. These restrictions are as follows:

- The simulation will begin and end at the approximate upper limit of the sensible atmosphere, 110 km. The simulation will not be bounded to remain below this mark during the simulation.

3

- The entry flight-path angle (ϕ) will be bounded between $[\phi \mid -\pi \; \epsilon \; 0]$ while the exit conditions will be the additive inverse.

A comparison will be conducted of different simulation conditions with the objective of maximizing inclination. Table 1 shows the variations of the constraints that will be studied.

Table 1. Parameters for Comparison Analysis

Parameter	Value
Heating Rate, $\dot{q}$	0.75-10 $\frac{MW}{m^2 s}$
Maximum Thrust, T_{max}	500-10,000 N
Specific Impulse, I_{sp}	150-1000 s
Heat Load, Q	150-1000 $\frac{MJ}{m^2}$
Acceleration, a_{decel}	2-8 g
Specific Impulse, I_{sp}	300-2000 s
Vehicle Mass,	4500 - 15500 kg
Fuel to Mass Ratio,	6 - 41%

Additionally, the thrust vectoring aerocruise will be compared to the un-powered aeroglide. Both simulations will utilize GPOPS-II with the objective of achieving maximum inclination change with the same constraints. Varying constraint cases will be compared and analyzed. Finally, a skip entry simulation using constraints comparable to the X-34 hypersonic vehicle will be compared to an exo-atmospheric maneuver assuming both cases expend all available propellant mass to perform the maneuver. A Hohmann transfer will be used to conservatively calculate de-orbit and re-orbit ΔV expenditures for the skip entry.

1.4 Thesis Overview

Research objectives are outlined in Chapter I, with Chapter II reviews relevant research of aeroassisted maneuvers with a focus on optimization techniques used in GPOPS-II and similar software. In Chapter III, the dynamics model is defined and verified with the simulation case of the Apollo 10 re-entry. A thorough description of the controls, objective function, and constraints used in GPOPS-II and the opti-

mal control problem are also presented in Chapter III. The final section of Chapter III will define the aerodynamics model used in all simulations underpinning this research. Chapter IV presents the relevant research conducted to answer the objectives described in the first chapter. Chapter IV will detail how varying vehicle capability and constraints alters the simulation and how these variations affect the performance of the simulation. Finally, Chapter V summarizes and provides conclusions to the overall research, describes the way forward for further research, and discusses the relevance of the present research.

II. Literature Review

2.1 Chapter Overview

The purpose of this chapter is to highlight relevant research related to synergetic atmospheric maneuvers and control optimization of dynamical systems.

2.2 Atmospheric Maneuvers

In 1961, Howard London presented "Change of Satellite Orbit Plane by Aerodynamic Maneuvering" where he detailed how a spacecraft may save ΔV by skipping into and out of the atmosphere. London's research sparked a wave of research in non-terminal re-entry dynamics. Costly exo-atmospheric inclination changes motivated London and others to explore new ways to reduce the ΔV required for orbital plane changes. The function for a simple plane change shown below, is a function of the orbital velocity, flight-path angle, and inclination change for a given spacecraft:

$$\Delta V_{simple} = 2V \cos\gamma \sin\left(\frac{1}{2}|\Delta i|\right) \tag{2.1}$$

London points out that an impulsive inclination change found by Eq. 2.1 of $60°$ is comparable to the initial ΔV required to launch into orbit [5].

F.S Nyland writing for the RAND Corporation detailed how a skip maneuver could be divided into five phases of flight: descent phase, ΔV_1; pullout phase; un-powered glide phase, ΔV_2; ascent phase, ΔV_3; and injection phase, ΔV_4. Overall, the total ΔV for the maneuver is the summation of the ΔV corresponding each phase of the trajectory. The descent phase considers a spacecraft in a circular orbit that must enter a ballistic trajectory by a propulsive maneuver. The pullout phase is a transitional phase that Nyland considered in order to match the incoming flight-path angle with

a flight-path angle required to enter the third phase of flight. The spacecraft may perform this action by maintaining a constant lift-to-drag ratio as it enters the upper atmosphere. Nyland considered the pullout phase completed when the vehicle reached a zero flight-path angle indicating the perigee of the re-entry orbit. The spacecraft then enters the un-powered glide phase, where the bank angle is used to orient the lift vector to enter an aerodynamic turn. At the end of this phase the spacecraft would not have enough velocity to exit the atmosphere and must power itself out of the atmosphere. The ascent phase accounts for the additional ΔV required for injection into a new orbit and the final maneuver is used to re-circularize this orbit. Nyland continued his research by considering a synergetic plane change where continuous thrusting would be employed through the glide phase to counter the affects of drag. He considered an optimal thruster cant angle for minimizing propellant expenditure as being

$$\tan(\delta) = D/L \tag{2.2}$$

where δ is the cant angle, D is drag, and L is lift force. Nyland concluded that a synergetic maneuver followed the same flight-path as the non-thrusting case, but at higher altitudes. This increased altitude results in lower heating rates due to the decrease in atmospheric density. As research into skip entries progressed, researchers predominately followed the five stages identified by Nyland; however the activities in each phase created a new vocabulary for identifying each type of possible maneuver in search of the optimal solution.

An aeroglide maneuver is a glide through the atmosphere utilizing aerodynamic forces during the glide phase. Propulsive energy begins the maneuver and re-circularizes the orbit in the injection phase. Alternatively, the aerocruise maneuver utilizes thrust during the glide phase where thrust is typically set equal and opposite of drag. Also using thrust, an aerobang maneuver refers to a maximum thrusting case throughout

8

the glide phase. This maneuver typically eliminates the need to perform an insertion burn. In more recent research the aerocruise is used as blanket term for any thrusting in the atmosphere since the thrust is often optimized. This research will use the latter definition of aerocruise [6].

2.3   Research of Synergetic Skip Entries

Synergetic skip entries have been researched for varying circumstances through the past few decades. This section highlights a portion of this research and discusses how it has advanced since the days of London and Nyland.

First, NASA employed a multiple shooting iteration scheme on a Space-Shuttle orbiter class vehicle in 1973. This simulation used the aerodynamics and vehicle characteristics of the Space Shuttle to compare inclination change produced by exo-atmospheric and aeroassisted maneuvers. With constraints on heat rate and heat load considered, the researchers concluded that plane changes over $5°$ were more efficiently achieved by an atmospheric maneuver than the simple plane change [7].

A few years earlier Roessler, with the Swiss Federal Institute of Technology in 1967 researched the propulsive maneuver using a fourth-order Runge-Kutta method optimizing by the steepest descent method. His research started the maneuver with an initial inclination of $30°$ and found the minimal ΔV needed to make specified inclination changes. He found that decreasing the inclination was less costly than increasing the inclination by the same degree, concluding that the Earth's oblation affected the achievable results [8]. Working in 1990, Vinh and Ma presented the exact non-dimmensional equations necessary for an optimal numerical solution of a contracting orbit making trans-atmospheric maneuvers at each pass through perigee. They concluded that a short-duration pass with a high deceleration and a long duration maneuver with low deceleration had the same results [9].

9

Some aeroassisted research took more practical approaches to the aeroassited problem by investigating potential missions for this manuever option. Bettinger and Black conducted a comparative study of phasing, atmospheric skip entry, and simple plane change maneuvers by examining the ΔV required to overfly certain ground targets. Their study concluded that skip entry maneuvers required less than 0.5 km/s of ΔV. In addition, the method showed that aeroassisted maneuvers could in general be used to overfly diverse ground targets with a lower time-of-flight and less energy than purely exo-atmospheric maneuvers [10].

Focusing more on optimization, Rao, Tang, and Hallman considered the multiple-pass aeroassisted orbital transfer from geostationary orbit to LEO with a large inclination change. Their problem was constructed as a multiple phase optimal control problem using Sparse Optimal Control Software (SOCS). SOCS uses a direct, rather than indirect, numerical method for solving optimal control problems. This research showed the accuracy of direct methods to provide accurate solutions to problems of this type [11].

This section has shown the diverse application of aeroassisted maneuvers throughout the past few decades of research and how it has evolved overtime. The next section will study direct optimization techniques, specifically GPOPS-II, and how to set-up problems in optimization software.

2.4 Optimization Techniques of Synergetic Re-Entry

Writing a survey of numerical methods for optimal control, Rao describes various techniques for solving optimal control problems using indirect and direct numerical methods. An indirect method uses calculus of variations to determine the first order optimality condition, which leads to a boundary-value problem. The boundary-value problem is solved to find potential optimal trajectories termed extremals, where low-

est cost extremal represents the optimal condition. By contrast, in a direct method the state or control is discretized by a preferred method and converted to a nonlinear programming problem (NLP) which is then solved using well documented NLP optimization techniques [12]. This research will utilize the optimal control software GPOPS-II created by Patterson and Rao. A complete summary and explanation of GPOPS-II can be found in [13]. As an overview, GPOPS-II, uses a "Legendre-Guass-Radau quadrature orthogonal collocation method where the continuous-time optimal control problem is transcribed to a large sparse non-linear programming problem (NLP). An adaptive mesh refinement method is implemented that determines the number of mesh intervals and the degree of the approximating polynomial within each mesh interval to achieve a [user] specified accuracy." This research will utilize the NLP solver IPOPT, which is a gradient- based method for solving non-linear optimization or non-linear programming problems. A complete description of these types of problems and their role in solving the optimal control problem can be found in [12]. Further discussion of the optimal control problem will be documented in Chapter III. The rest of this section will discuss methods for solving problems with GPOPS-II and other optimal control problems, found in literature, that assisted with the solution for the present research.

The optimal control problem can be solved by defining the differential equations that define the motion (states), the controls to be optimized, path constraints of the problem, the initial and final time, integrals, and the static parameters that minimize the cost functional subject to dynamic constraints, event constraints, inequality path constraints, and integral path constraints [14]. Defining some of the constraints and controls of problems becomes something of an art in GPOPS-II, where knowing the right techniques can make all the difference. A survey paper of solving spacecraft trajectory optimization problems was conducted in [15] where a complete breakdown

of the problem, and various solution methods are presented. Of particular interest in this survey, are the various methods for defining the cost functional, or objective functional. Different techniques have been utilized in various research to translate physical desires or trade spaces into mathematical relationships that better define the cost functional. Such methods are described in the survey, and will be cited further in the present research in applicable sections.

Fuhr and Rao researched a similar problem to the present research in their study of aerothrust versus aeroassisted orbital transfer of small spacecraft. They defined the problem using a traditional formulation of the six states required to define the motion: radius of the orbit, latitude, longitude, velocity, flight-path angle, and azimuth. For a control law, Fuhr and Rao used research from [11], which is given below:

$$u_1 = C_l \cos(\sigma) \tag{2.3}$$

$$u_2 = C_l \sin(\sigma) \tag{2.4}$$

where u_1 and u_2 are bound by the path constraint

$$0 \leqslant u_1^2 + u_2^2 \leqslant C_{lmax}^2. \tag{2.5}$$

Using this formulation is necessary because the bank angle (σ) wraps and is difficult to bound between 0 and 2π when solved as a separate control variable. Including the lift coefficient as a positive constant reduces the number of controls in the problem. The lift coefficient and the angle-of-attack are related by

$$C_l = C_{l\alpha}\alpha, \tag{2.6}$$

where $C_{l\alpha}$ is a constant of the airfoil being simulated in the problem. The bank angle can be solved in this formulation by

$$\sigma = \tan^{-1}\left(\frac{u_2}{u_1}\right) \qquad (2.7)$$

This method for solving the control variables of a skip entry maneuver significantly improves computation time by creatively combining controls, and using path constraints to ensure GPOPS-II is accurately solving for the control within the bounds of the problem.

Fuhr and Rao constrained the transatmospheric maneuver using [16] formulation of the stagnation point heating rate due to atmospheric heating

$$\dot{Q} = \bar{\dot{Q}}\left(\frac{\rho}{\rho_s}\right)^{0.5}\left(\frac{v}{v_c}\right)^{3.15} \qquad (2.8)$$

where $\bar{\dot{Q}}$ is a reference heat-transfer rate $\bar{\dot{Q}} = 199.87$ MWm^{-2}, v_c is the Earth radius circular speed of a spacecraft, $v_c = \sqrt{\mu/R_\oplus}$, ρ is the density at the current time and altitude, ρ_s is the sea-level density, v is the velocity at the current time. The stagnation heating load can be solved by integrating equation 2.8 from the time of atmospheric entry to atmospheric exit. In GPOPS-II the integral bounds of this equation can be set between zero and the maximum stagnation heating load. For a heating rate constrained problem $\dot{Q}$ can be constrained using the following path constraint;

$$0 \leqslant \dot{Q} \leqslant \dot{Q}_{max}. \qquad (2.9)$$

Fuhr and Rao researched the minimum fuel problem for a given final inclination. The first phase optimized the ΔV needed to de-orbit, while the second phase optimized the path through the atmosphere. The final phase optimized ΔV required for orbit raising and re-circularizing. The first and final phases were solved by formulating the

ΔV as a parameter subject to constraints using the ideal rocket equation relating the parameter to the mass ratio, thus making it possible to have a unique objective through all phases. It will be shown in Chapter III that the present research benefits greatly from the formulation Fuhr and Rao used for the control and heating constraints [17].

2.5 Summary

This chapter showcased historical and contemporary research of the skip entry maneuvers, as well as the optimal control problem associated with such maneuvers and methods used to set up these problems in modern computing software. Despite a wide range of physical parameters considered in the aeroassisted maneuver, no research has been found that considered thrust vectoring except in cases of a single cant angle along the direction of drag as in Nyland's original research. Furthermore, no research considered a free thrust vector not bounded to the vertical in-plane direction. Modern optimization methods were discussed thoroughly, and their techniques will be utilized in the present research to expand the aeroassisted problem by including thrust vectoring.

III. Methodology

3.1 Assumption and Limitations

The purpose of this chapter is to overview the assumptions, limits, and algorithms used to model the re-entry dynamics governing the present research. The Apollo 11 re-entry trajectory will be simulated and compared to the NASA post-flight analysis for verification of the overall dynamics model. The atmospheric density, gravity potential, and re-entry heat flux will be detailed, along with information on the optimization and numerical integration tools being utilized. This research made thorough use of Ashish Tewari's *Atmospheric and Space Flight Dynamics* text and associated re-entry dynamics model [18].

3.1.1 Planetary Model and Constraints

The Earth is not a perfect spheroid and, as a result does not maintain a spherical gravity potential. The oblateness of Earth's shape can be approximated by computing the non-radial components of the gravitational acceleration with the following vector

$$g = g_r \hat{e}_r + g_\phi \hat{e}_\phi \tag{3.1}$$

described from the local horizontal frame. In Eq. 3.1 $\hat{e}_r$ is the direction along the radial vector pointing from the center of the Earth to a point mas,s and $\hat{e}_\phi$ is the southward direction, perpendicular to $\hat{e}_r$. This equation can describe the spherical Earth by setting $g_\phi = 0$ and approximating g_r by Newton's law of gravitation between two masses, which simplifies to:

$$g = g_s \left(\frac{R_\oplus}{r} \right)^2 \tag{3.2}$$

15

where g_s is the gravitational acceleration at sea-level. For this research the components of gravity will be described by equations for g_r and g_ϕ and use Jeffery constants 2-4 for Earth which represent the spherical harmonics of an axisymmetric planetary mass distribution. These constants are given below:

$$J_2 = 1.08263e^{-3} \tag{3.3}$$

$$J_3 = 2.532153e^{-7} \tag{3.4}$$

$$J_4 = 1.6109876e^{-7} \tag{3.5}$$

The gravitational components in Eq 3.1 are defined by

$$g_r \frac{r^2}{\mu} = (1 - 1.5J_2(3\cos^2(\phi) - 1)\left(\frac{R_\oplus}{r}\right)^2 - 2J_3\cos(\phi)(5\cos^2(\phi) - 3)\left(\frac{R_\oplus}{r}\right)^3 \tag{3.6}$$
$$- \frac{5}{8}J_4(35\cos^4(\phi) - 30\cos^2(\phi) + 3)\left(\frac{R_\oplus}{r}\right)^4$$

$$g_\phi = \frac{3\mu}{r^2}\left(\frac{R_\oplus}{r}\right)^2 \sin(\phi)\cos(\phi)\left(\frac{R_\oplus}{r}\right)^2 \tag{3.7}$$
$$\left[J_2 + 0.5J_3(5\cos^2(\phi) - 1)\left(\frac{R_\oplus\cos(\phi)}{r}\right) + \frac{5}{6}J_4(7\cos^2(\phi) - 1)\right]$$

where ϕ is Earth's geodetic latitude measured in the inertial fixed Earth frame [19].

The dynamics model must include an approximation of the atmospheric density used in calculating the aerodynamic affects of re-entry. The exponential atmosphere can be described by

$$\rho = \rho_0 e^{-\beta h} \tag{3.8}$$

where ρ_0, β are the sea level density and atmospheric inverse scale height respectively. This model provides a reasonably accurate depiction of the atmosphere according to the *1976 U.S Standard Atmosphere* and is computationally efficient [20] [21].

The relevant planetary constants used in this research are in Table 2.

Table 2. Earth's Planetary Constants

Constant	Value
Gravitational Parameter, μ	3.98574405e14 $\frac{m^3}{s^2}$
Earth's Radius, $R_\oplus$	6378145 m
Gravitational Acceleration sea level, g_s	9.80665 $\frac{m}{s}$
Scale Height, β	.14 km^{-1}
Density at Sea-level, ρ_s	1.225 $\frac{kg}{m^3}$
Earth's Rotation Rate, $w_\oplus$	7.2921158e^{-5} $\frac{rad}{s}$

3.1.2 Dynamic Equations of Motion

From Newtons's Second Law the forces and accelerations of motion must be described for synergetic re-entry. Figure 1 shows the aerodynamic, thrust forces (f_T), and the thrust cant angles (μ,ϵ) for an example spaceplane-class vehicle. The angle of attack (α) can be described as the angle between the velocity and the longitudinal plane. The longitudinal plane symmetrically splits the airframe along the chord of the vehicle and is aligned with the velocity vector when the angle of attack is zero. Figure 2 shows how the angle of attack changes the direction of the lift (L) and drag (D) vectors while Fig. 3 shows how the bank angle (σ) alters the lift and side force (f_y) vectors.
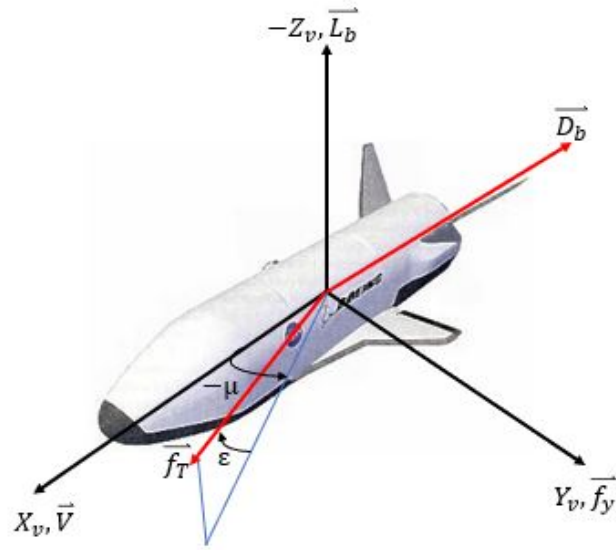
Figure 1.   Aerodynamic Forces and Vehicle Reference Frame Definition for Sample TAV
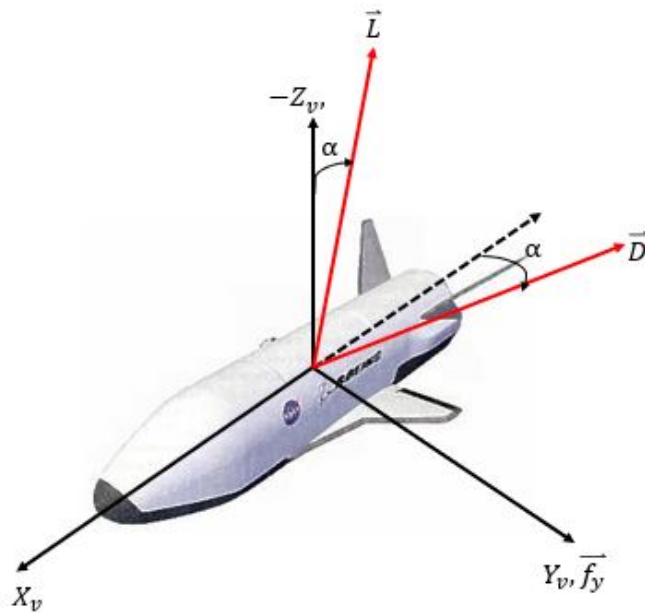
Figure 2.   Angle-of-Attack Description
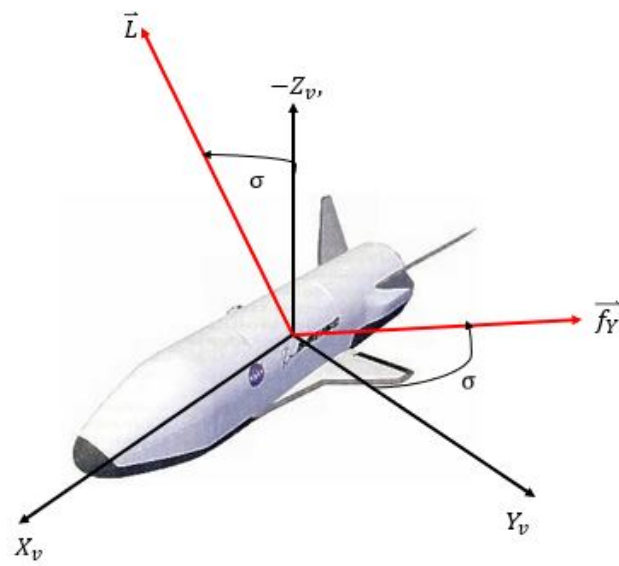
Figure 3. **Bank Angle Description [1]**

The six components of the position and velocity vectors can describe the motion of a moving object in three dimensional space. The position vector is defined by the radial vector $\vec{r}$ that extends from the center of the planet to a point mass. The components of the radial vector can be resolved to Earth's inertial frame by using angles describing latitude (δ) and longitude (λ). The velocity vector can be resolved into two components from the local horizon frame into two angles. The first is azimuth (A) which describes the angle between the direction of the velocity vector and North. The second is the flight-path angle (ϕ), which describes the velocity vectors deviation from the vehicle's local horizontal frame. If the azimuth is 90° and the flight-path angle is 0, a spacecraft would be travelling along the Earth's equatorial plane.

Tewari describes the kinematic equations of motion for a re-entering spacecraft relative to a rotating planet as

$$\dot{r} = V \sin \phi \tag{3.9}$$

$$\dot{\delta} = \frac{v}{r} \cos \phi \sin A \tag{3.10}$$

$$\dot{\lambda} = \frac{V \cos \phi \cos A}{r \cos \delta} \tag{3.11}$$

From the Earth centered fixed frame, three rotations involving latitude and longitude, define the local horizon frame as shown below where R denotes a coordinate rotation and the subscript describes the axis of rotation,

$$C_{LH} = R_2[-90°]R_2[90 - \delta]R_3[\lambda] \tag{3.12}$$

$$C_W = R_2[\phi - 90°]R_1[-A] \tag{3.13}$$

The local horizon frame is used in Tewari's formulation of the dynamics to describe the time derivative of the inertial velocity and derive the kinematic relationships. A wind axis (Eq. 3.13), defined by two rotations from the planet centered frame is used

to define the external forces acting on a point mass which are used in Newton's second law to write the dynamic equations of translational motion for re-entry.

$$m\dot{V} = f_T \cos \epsilon \cos \mu - D - mg_c \sin \phi + mg_\delta \cos \phi \tag{3.14}$$
$$- mw_\oplus^2 r \cos \delta (\cos \phi \sin \delta - \sin \phi \cos \delta)$$

$$mV \cos \phi \dot{A} = m\frac{v^2}{r} \cos^2 \phi \sin A \tan \delta + f_T \sin \mu + fy \tag{3.15}$$
$$- mg_\delta \sin A + mw_\oplus^2 r \sin A \sin \delta \cos \delta$$
$$- 2mw_\oplus V (\sin \phi \cos A \cos \delta - \cos \phi \sin \delta)$$

$$mV\dot{\phi} = m\frac{v^2}{r} \cos \phi + f_T \sin \epsilon \cos \mu + L - mg_c \cos \phi \tag{3.16}$$
$$- mg_\delta \sin \phi \cos A + mw_\oplus^2 r \cos \delta (\sin \phi \cos A \sin \delta$$
$$+ \cos \phi \cos \delta) + 2mw_\oplus V \sin A \cos \delta$$

$(r, \delta, \lambda, V, \phi, A)$ complete the TAV's state description. These equations can be integrated with respect to time and describe the motion of a spacecraft in orbit through re-entry.

The variable L and D are representative of the lift and drag on the TAV but do not always equate to the lift or drag of the body (L_b, D_b). In the former case L and D are defined by,

$$L = L_b \cos \alpha \cos \sigma - D_b \sin \alpha \tag{3.17}$$
$$D = D_b \cos \alpha + L_b \cos \sigma \sin \alpha \tag{3.18}$$
$$f_Y = L_b \sin \sigma \tag{3.19}$$

Equations (3.17), (3.18),(3.19) represent the forces of a body that are perpendicular and opposite to velocity in the vehicle frame, rotated to the wind axis frame through the angles β, α, σ. For this research it is useful to note that β here is the side slip angle and not the atmospheric inverse scale height. This research will ignore any effects from the side slip angle, while still considering μ as an in-plane thrust angle. In cases where thrust vectoring does not occur, $\epsilon = \alpha$ and $\mu = \beta$ which implies thrusting occurs only in the longitudinal axis. A description of this axis is illustrated in Fig. 4. However, this figure does not indicate the direction of the velocity vector, because the velocity vector and its direction are described by ϕ and A. The angle-of-attack has no effect on the velocity vector in this research other than its manipulation of the lift and drag forces. For the TAV's body, L_b and D_b are defined by the standard equations for lift and drag, respectively,

$$L_b = qSC_l \tag{3.20}$$

$$D_b = qSC_d \tag{3.21}$$

$$q = \frac{1}{2}\rho V^2 \tag{3.22}$$

where q is the dynamic pressure, S is the drag reference area, C_l is the lift coefficient, and C_d is the drag coefficient.

Figure 5 is used to define what this research will refer to as the "Lift" direction. The figure shows that positive ϵ angles place some thrust in the primary direction of the bodies lift vector being offset by the angle-of-attack α.
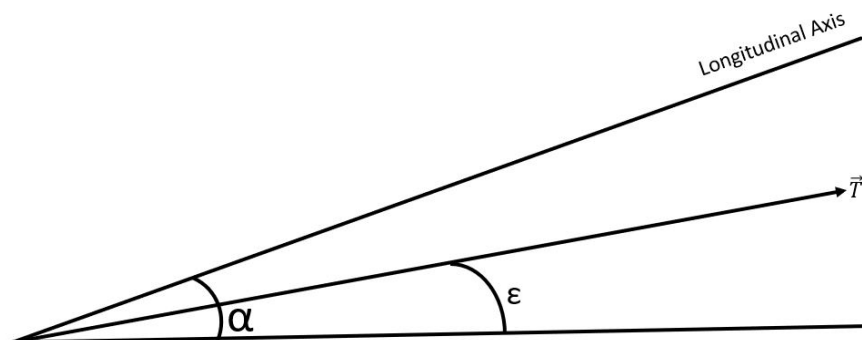
Figure 4. Pictorial Representation of α and ϵ
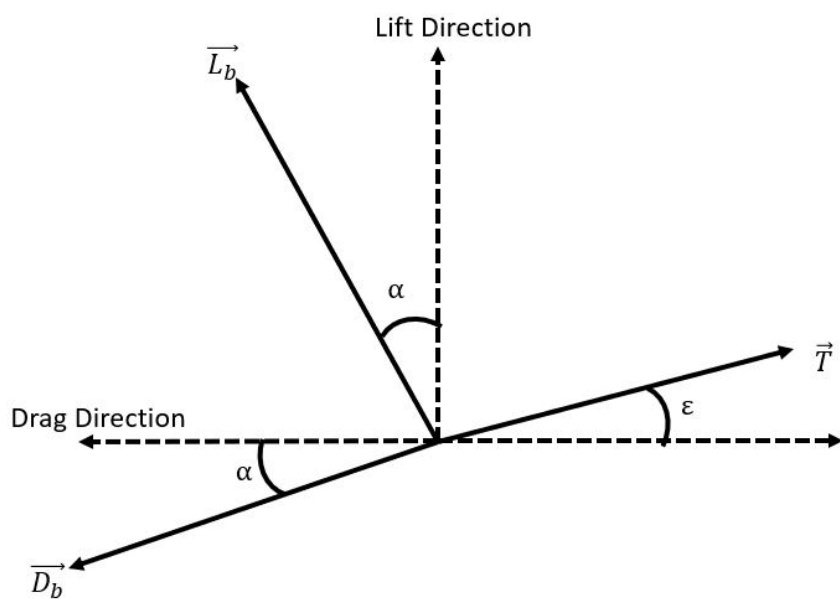
Figure 5. Lift and Drag Direction Definition

3.1.3 Model Verification: Apollo 10 Re-Entry Simulation

To demonstrate the accuracy of these equations the re-entry dynamics model, the Apollo 10 re-entry will be simulated and compared to NASA mission data. Hick's compiled the NASA data from references [22] [23] to create data entries for analysis in his text *Introduction to Astrodynamic Re-Entry*. The re-entry conditions are shown in Table 3, and the vehicle parameters are listed in Table 4. Hicks used an approximation for constant lift and drag coefficients which reduces complexity without adding a significant amount of error.

Table 3. Apollo 10 Entry Conditions

State	Value
Radius, r_e	6498.270 km
Flight path angle, ϕ_e	$-6.6198381°$
Heading Angle, ψ_e	$18.0683°$
Velocity, $^R V_e$	11.06715 km/s
Longitude, λ_e	$174.24384°$ East
Latitude, δ_e	$23.51457°$ South

Table 4. Apollo 10 Vehicle Characteristics

State	Value
Mass, m	5498.22 kg
Lift Coefficient, C_l	.40815
Drag Coefficient, C_d	1.2569
Reference Area, S	12.017 m^2

From Table 3, the heading angle is the compliment of the azimuth used in Tewari's formulation. NASA's data was recorded in the inertial frame while Tewari's equations

are derived from the relative rotating frame. Ignoring the rotation of the Earth in this simulation is the quickest way to adjust the results for comparison without a significant loss of accuracy. The states were integrated using a Runge-Kutta integration scheme from $t_0 = 0$ to the recorded time of touchdown $t_f = 498\ s$. Hick's equations of motion [24] were also integrated with the results plotted on Fig. 6 for comparison to Tewari's formulation. The plots for altitude, velocity, deceleration, and flight-path angle are shown below. Not shown, NASA recorded the final longitude at $164.65°W$, compared to the final longitude of this simulation of $164.10°W$.

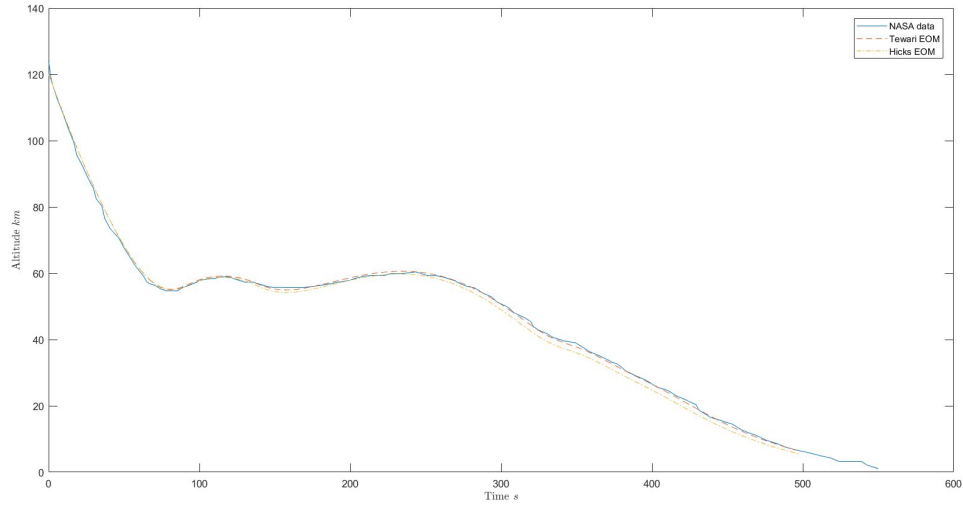**Figure 6.   Apollo 10 Altitude Comparison**

25
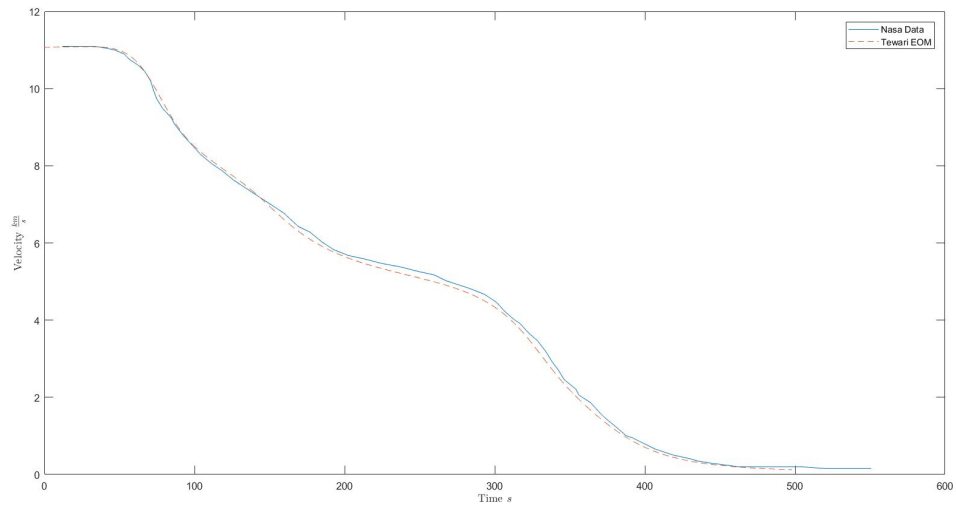
Figure 7.   Apollo 10 Velocity Comparison
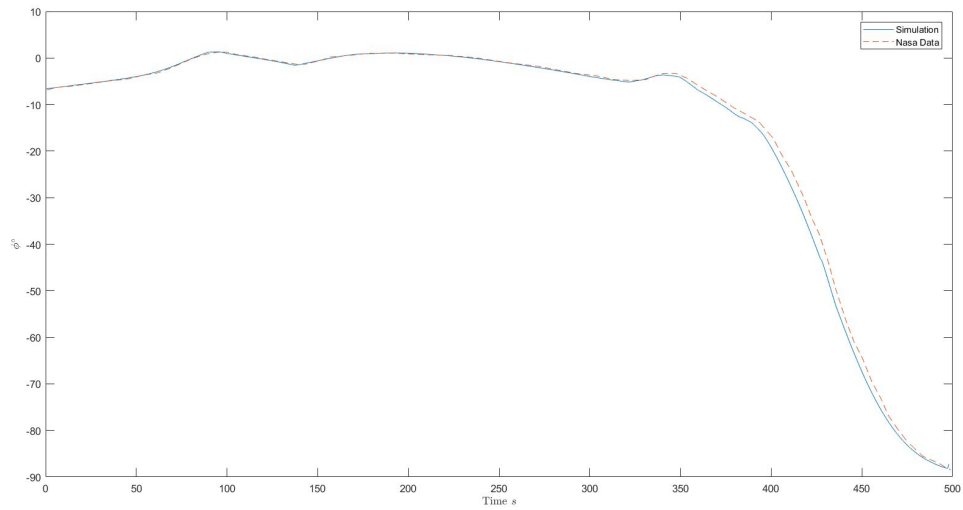
Figure 8.   Apollo 10 flight-path angle Comparison
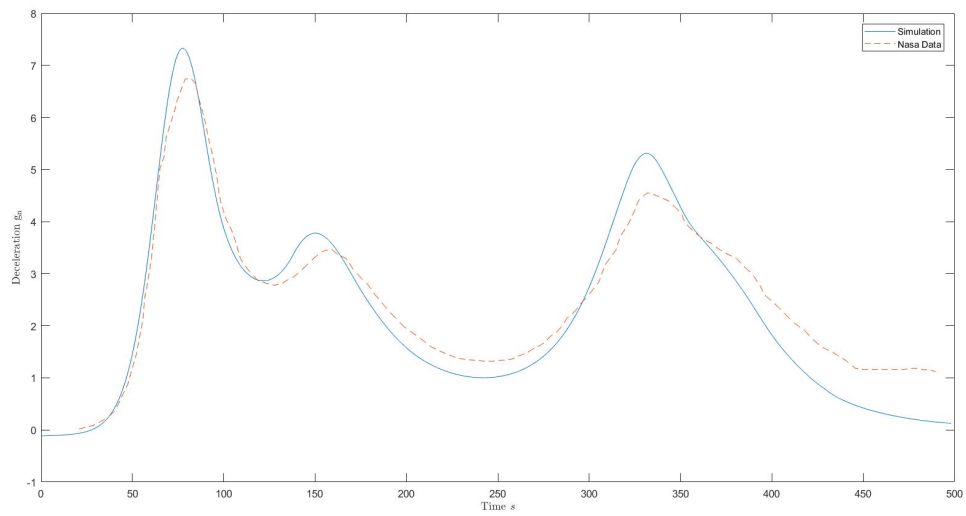
Figure 9. **Apollo 10 Deceleration**

Possible areas of error between the NASA data and the simulation are:

- The use of a constant C_l and C_d

- Ignoring the rotation of the Earth

- The simplicity of the exponential atmospheric model

- Inaccuracies in the NASA reports. Hicks describes that that the NASA reports have multiple values recorded for the same parameters

- Hicks compilation of data for comparison by directly reading from the charts provided in the NASA reports

- The bank angle data points were only available for some portions of the flight; therefore, the points needed to be interpolated in the simulation to accurately capture the motion.

- Error inherent in the integration method

Hicks provides more detail about how some of the model assumptions affect the outcome of the solution and re-works the simulation to remove some of the errors. The results of these reductions are noted in [25]. Cumbersome improvements to the simulation yield only minor error reductions. The purpose of this section was to demonstrate the accuracy of the dynamics model before proceeding to the present research. This objective is satisfied without the need of including these cumbersome changes to the simulation.

Before proceeding to the present research, the Apollo 10 simulation offers additional information that can be used to validate the results presented in Chapter IV. The lift, drag, and side forces calculated in the simulation are presented in the following figure. Their magnitudes can be compared to the magnitudes of the present

research to validate the results of the aerodynamic model simulation. As shown in fig. 10, the drag force follows a similar trajectory trend as the deceleration plot given in fig. 9. This validates our simulation further since the deceleration of Apollo 10 was principally caused by the changing drag force through the atmosphere.
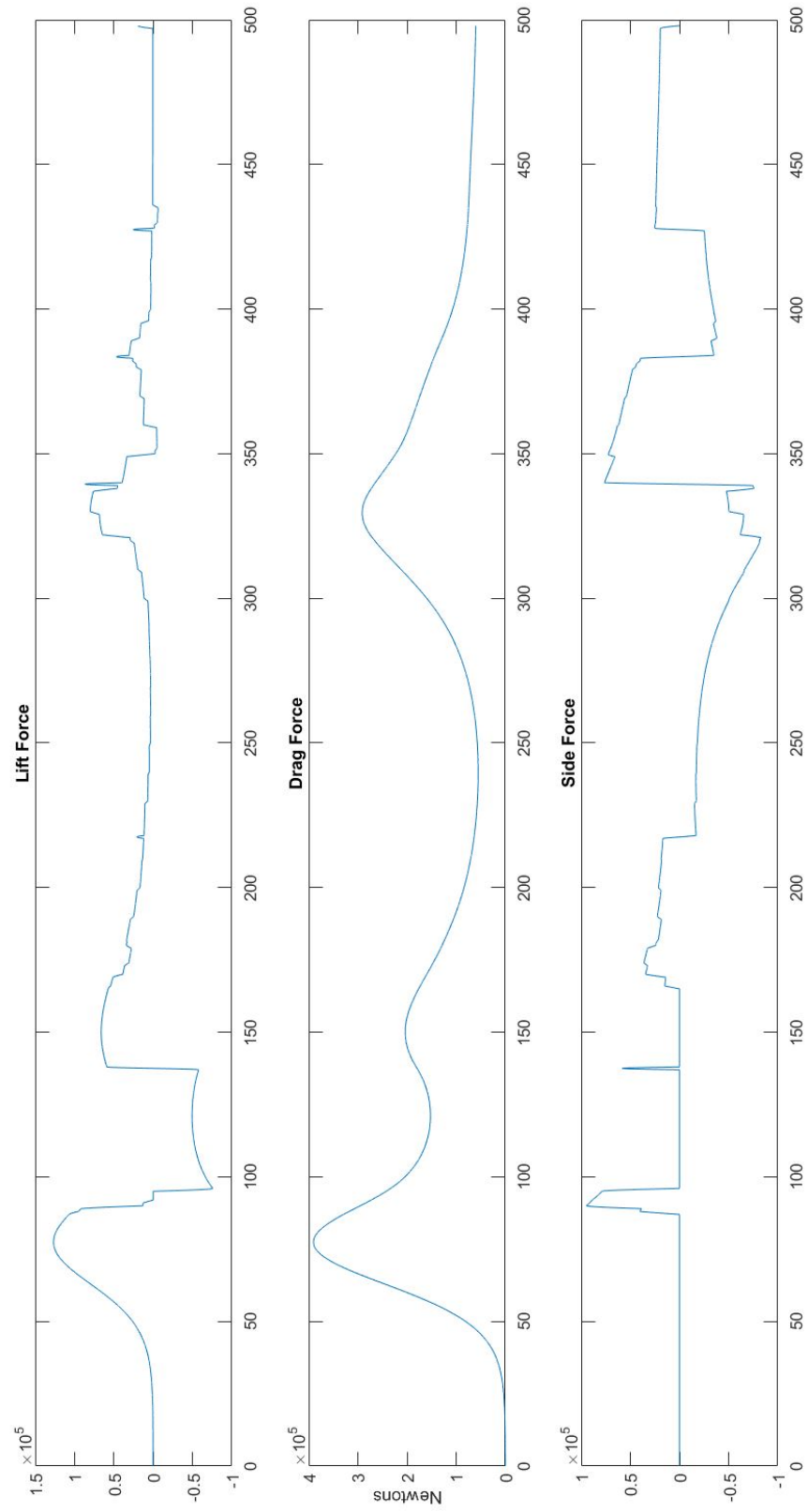
Figure 10. Apollo 10 Aerodynamic Forces

30

Additionally the heating model, Eq.2.8, was integrated for the Apollo 10 simulation. These results can be used to both validate and constrain the present research.
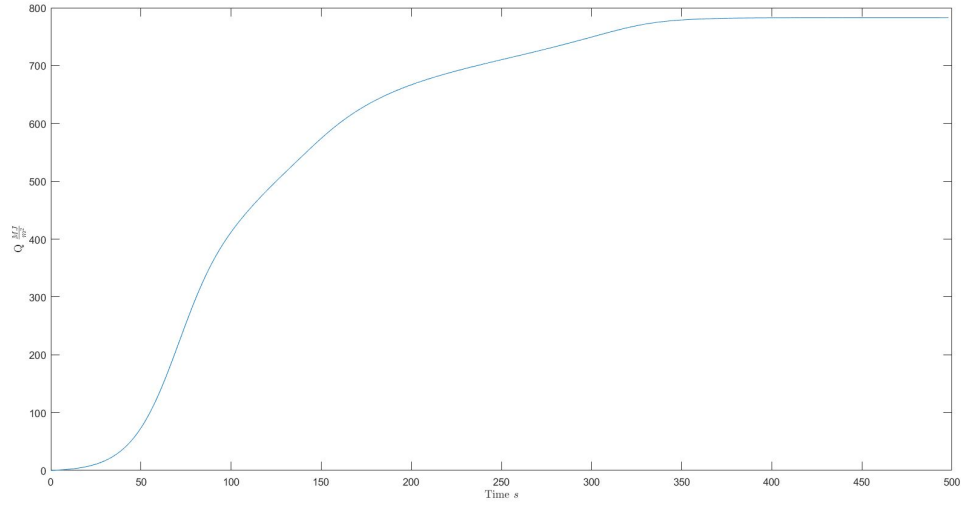
Figure 11. Apollo 10 Total Heat Load

3.2 Optimal Control Problem

The purpose of this section is to describe the optimal control problem and how the present research is set-up within GPOPS-II. As described by Eqs.(1-6) in [13], the optimal control problem needs a defined state X, control u, initial time t_0, final time t_f, integrals q, and static parameters that minimize the functional J subject to the dynamic constraints $\dot{X}$, event constraints e, inequality path constraints $p_{min} \leqslant p \leqslant p_{max}$, and integral constraints $q_{min} \leqslant q \leqslant q_{max}$.

3.2.1 Formulation of the State Vector and State Constraints

The state vector is defined as

$$X = \begin{bmatrix} r \\ V \\ \phi \\ A \\ \lambda \\ \delta \\ m \end{bmatrix} \tag{3.23}$$

where m is the mass and has been added to the state vector for thrusting cases. The rate of mass loss is computed from the ideal rocket equation as,

$$\dot{m} = -\frac{f_T}{I_{sp}g_s} \tag{3.24}$$

Where f_t is the magnitude of thrust, I_{sp} is the specific impulse, and g_s is Earth's gravitational force at sea level.

The dynamic constraints are defined by the derivatives of the state vector and their respective bounds in each phase of flight. The initial state will defined by the following conditions:

- The initial altitude will begin at the edge of the sensible atmosphere which is somewhat ambiguous and will be defined in the present research as, $h_0 = 110$ km

- The initial velocity will be 7.5 km/s which is a reasonable re-entry speed for a spacecraft in LEO

- The initial flight-path angle will be $\phi_0 \leqslant 0$ to force re-entry

- For continuity of simulations in the present research, the vehicle will be travelling along the equator and will reach the edge of the sensible atmosphere at the intersection of the prime meridian and equator. $A = \frac{\pi}{2}$, $\lambda_0 = 0$, $\delta_0 = 0$

The constraints of the states after t_0 will be defined below in Table 5. The state constraints on r and ϕ at t_f will be, $110 \leqslant r_f \leqslant r_{max}$ km and $0 \leqslant \phi_f$, so that the spacecraft is exiting the atmosphere at the final time. The constraints placed on the flight-path angle were chosen to save computation time, and are far outside the optimal solution allowing for decreased computation time without constraining the problem unnecessarily.

Table 5. State Constraints

Parameter	Value
Position, r	$R_\oplus \leqslant r \leqslant 200(km)$
Velocity, V	$4 \leqslant V \leqslant 9(\frac{km}{s})$
Flight Path Angle, ϕ	$-20° \leqslant \phi \leqslant 20°$
Azimuth, A	$0 \leqslant A \leqslant 360°$
latitude, δ	$-90° \leqslant \delta \leqslant 90°$
longitude, λ	$0 \leqslant \lambda \leqslant 150°$
mass, m	$mass_{min} \leqslant m \leqslant mass_{max}$
time, t	$0 \leqslant t \leqslant 2000s$

3.2.2   Parameterization of the Controls

The optimization of a synergetic skip entry is not without an extensive list of potential controls. The control variables are: engine cant angles μ and ϵ, the angle of attack α, bank angle σ, and the thrust magnitude f_T. Except α, the angle controls will experience angle wrapping issues which can become cumbersome to handle in computer computations. As shown in Chapter II other researchers have solved this problem in various forms. With this in mind, the present research found the following formulation computationally efficient and effective:

$$u_1 = f_T \cos \epsilon \cos \mu \tag{3.25}$$

$$u_2 = f_T \sin \mu \tag{3.26}$$

$$u_3 = f_T \sin \epsilon \cos \mu \tag{3.27}$$

$$u_4 = C_l \sin \sigma \tag{3.28}$$

$$u_5 = C_l \cos \sigma \tag{3.29}$$

Using this formulation improves computation and overcomes angle wrapping issues. In this formulation, the control bounds are represented by the inequality path constraints,

$$0 \leqslant u_1^2 + u_2^2 + u_3^2 \leqslant f_{T_{max}}^2 \tag{3.30}$$

$$0 \leqslant u_4^2 + u_5^2 \leqslant C_{l_{max}}^2 \tag{3.31}$$

This parameterization method is not without its limitations. It makes it difficult if not impossible to constrain the cant angles; however, it is a useful formulation for indirectly adding, α, as a control. The angle of attack can be efficiently solved for if the lift coefficient is a linear function of α. The lift coefficient can be found at any time by the squared trigonometric relationship of sine and cosine as in Eq. (3.31). Similarly, the magnitude of thrust can be solved for as in Eq.(3.30).

The bank angle can be found without quadrant ambiguity since we know the sine and cosine, and their respective signs by taking the inverse tangent:

$$\sigma_c = \tan^{-1}\left(\frac{u_4}{u_5}\right) \tag{3.32}$$

Table 6. Bank Angle Quadrant Correction

sine	cosine	Bank Angle
-	-	$\sigma = \pi + \sigma_c$
-	+	$\sigma = 2\pi + \sigma_c$
+	-	$\sigma = \pi + \sigma_c$
+	+	$\sigma = \sigma_c$

The cant angles μ and ϵ can be solved for with a similar scheme. First, a potential solution for the angles must be found. These potential solutions will be denoted by the subscript p. The cant angle μ_p can be found by taking the inverse sine of (u_2/f_T). Next, ϵ_p can be found by taking the inverse tangent of (u_3/u_1) since the cosine of μ will cancel from the quotient of these two solutions. From here, the control parameterization needs to be compared to the potential solutions by recalculating u_1 and $u3$ using μ_p and ϵ_p.

$$u_{1p} = f_T \cos \epsilon_p \cos \mu_p \tag{3.33}$$

$$u_{3p} = f_T \sin \epsilon_p \cos \mu_p \tag{3.34}$$

When comparing our potential solution to the actual solution:

- If $u_{1p} = -u_1$ and $u_{3p} = -u_3$ then the wrong angle for μ has been calculate and needs to be corrected by $\mu = \pi - \mu_p$. The calculation of u_{2p} is not required, because it will always be equal to u_2. Changing μ by the addition of π does not change the value of u_2, because the value of the inverse sine has not changed.

- If $u_{1p} = -u_1$ and $u_{3p} = u_3$, then the value of ϵ_p is incorrect and must be change by $\epsilon = \pi - \epsilon_p$. This changes the sign of u_{1p} while maintaining the correct sign of u_3.

- If $u_{1p} = u_1$ and $u_{3p} = -u_3$, then the value of $\epsilon = -\epsilon_p$. This will change the sign of u_{3p} while maintaining the sign of u_{1p}

Following this scheme solves for all the controls without quadrant ambiguity.

3.2.3 The Objective Functional

The objective functional captures the intent of the present research, which is to understand how variable thrust vectoring can affect the inclination change of a single

skip entry. Therefore, the objective function must take the form,

$$J = \text{maximize } (\Delta i). \tag{3.35}$$

It has been shown in reference [5] and [17] that the inclination change of skip entry can be calculated from the states as

$$i = \cos^{-1}[\cos \delta \sin A] \tag{3.36}$$

using this formulation Eq. 3.35 can be rewritten to represent the final inclination of the maneuver,

$$J = -\cos^{-1}[\cos \delta_f \sin A_f] \tag{3.37}$$

where the negative is needed to calculate the maximum of the objective functional, and sub-script "f" indicates the final time value of the states.

Due to the boundary conditions imposed on azimuth, the nature of endo-atmospheric versus exo-atmospheric flight, and the classic definition of inclination, the inclination change calculated herein will not correspond to the actual final orbital inclination that would be calculated as an orbital parameter at the termination of atmospheric flight. Instead, the angle solved for by Eq. (3.37) is an angle measured from the Equator to the point mass measured clockwise from the equatorial plane. For purposes of this research, "inclination" will have this definition; alternatively, "orbital inclination" will be defined in the more classical sense as the angle between the equatorial plane to the orbital plane at the ascending node. If a solution results in, $i_f \geqslant 90°$ then the vehicle has gone from travelling West-East (prograde) to an East-West (retrograde) orbit. This can be achieved by turning into the Southern Hemisphere if the initial orbit is aligned with equatorial plane. It should be expected that most solutions will travel into the Southern Hemisphere, because the azimuth has been defined as

being the angle measured from the North Pole clockwise from $0 \leqslant A \leqslant 2\pi$. This eliminates negative solutions for azimuth which improved computation time. The energy expended travelling into the Southern Hemisphere is equal to the energy that would be expended traveling into the Northern Hemisphere because the gravity vector is symmetric about the equator. To be clear, a change in inclination would be mathematically the same using either definition.

3.2.4 Further Constraining the Optimal Control Problem

To this point, the states, controls, the objective, and their constraints have been presented. This formulation will be true for all cases considered. This section will describe additional constraints that will be used to further understand the problem being researched herein.

3.2.4.1 Heating Constraint

The heating constraint can be described by Eq. (2.8). Total heating can be found by the integral from the entry to the final time.

$$Q = \int \dot{Q} dt, \tag{3.38}$$

An integral constraint can be placed on Eq.(3.38) to bind the total heating during the maneuver, and a path inequality constraint will limit the heating rate during re-entry.

3.2.4.2 Acceleration Limits

The primary component of acceleration will be in the tangential direction described by the negative of Eq. (3.14). This equation can be bound in GPOPS-II

using a path constraint inequality of the form,

$$0 \leqslant a_{decel} \leqslant a_{decelmax} \tag{3.39}$$

Re-entry deceleration rates are usually described in terms g-forces (g_n) where the acceleration term is normalized by the acceleration due to gravity as:

$$a_{decel} = \frac{-\dot{V}}{\sqrt{g_r^2 + g_\delta^2}} \tag{3.40}$$

3.3 Aerodynamic Model for Simulation

The aerodynamic model chosen for the simulations analyzed in Chapter IV follows the X-34, a suborbital reusable rocket demonstrator flown in 2001 [26]. A linear curve was approximated for C_l, while a parabolic curve fit was used for C_d as a function of α expressed in radians by Eqs. (3.41) and (3.42), respectfully. The data points used to generate the curves from [26] are in Table 7. Finally, figure 12 shows the plotted data and the curve fit used to simulate this data.

$$C_l = 2.6632\alpha + .2078 \tag{3.41}$$

$$C_d = 3.9394\alpha^2 - .01572\alpha + .1043 \tag{3.42}$$

Table 7. Lift and Drag Coefficient Values for X-34

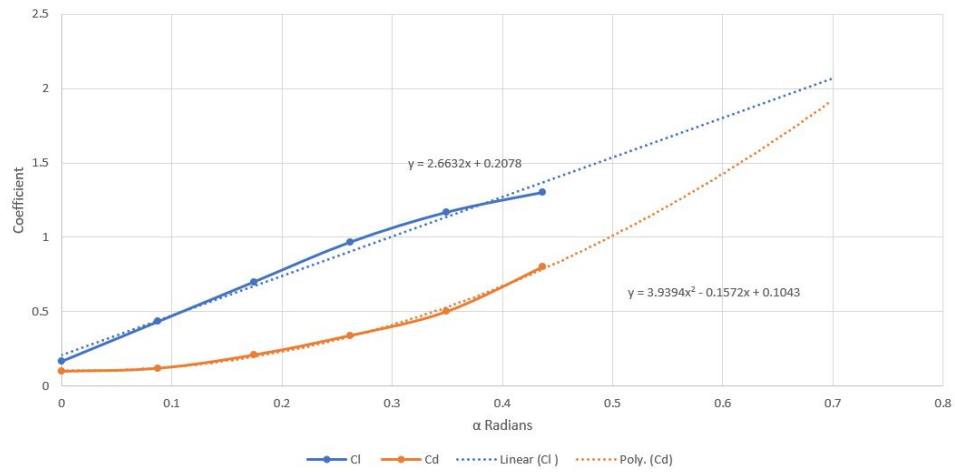| α	C_l	C_d
0	0.17	0.1
0.087	0.43	0.12
0.175	0.7	0.21
0.262	0.97	0.34
0.349	1.17	0.5
0.436	1.3	0.8 height

Figure 12. X-34 Aerodynamic Coefficient Data

3.4 Summary

This chapter defined the dynamics model used to describe the motion of a spacecraft from orbit through re-entry. This model was verified for accuracy by comparing a simulated trajectory solution, to actual data from the Apollo 10 re-entry capsule. Next, a complete description of the optimal control problem was given. The states, controls, and objective function were all defined along with additional constraints to be research in Chapter IV. Finally, the aerodynamics model and its limitations used in the present research was shown. Chapter IV will describe how this methodology was used to study the synergetic skip entry with dynamic thrust vectoring control.

IV. Results and Analysis

4.1 Overview

Analysis of a comprehensive set of parametric cases is studied in this chapter. The goals of the cases are to understand how varying TAV parameters alters the solution of a thrust vectoring synergetic skip entry and how thrust vectoring may alter the effectiveness of skip entries to change the inclination of an orbiting TAV. The first section will compare two cases of skip entry: An unpowered aeroglide, and a thrust vectoring aerocruise. The subsequent sections will exclusively study thrust vectoring aerocruise cases. Next, the thrust vectoring aerocruise will be compared to a purely exo-atmospheric inclination change using constraints based on the X-34. Following this comparison, a formulation for constrained thrust vector problem will be described, and a performance comparison made to the unconstrained solution. Finally, a summary of the collaborative work will tie the results together in a conclusion. TAV constraints in each case studied in the following sections are presented in Table 8; any exceptions to these constraints will be described in the relevant sections.

Table 8. TAV Properties

Parameter	Value
Specific Impulse, I_{sp}	$310s$
Thrust, T	$3000N$
Reference Area, S	149.2 m^2
Deceleration Limit	8 g_n
Max Heating Load, q	$1000\frac{MJ}{m^2}$
Heating Rate Limit, $\dot{Q}$	$10 \frac{MW}{m^2}$
Initial FPA, ϕ_0	$-20° \leqslant \lambda \leqslant 0°$
Initial Velocity, V_0	$7.5\frac{km}{s}$
mass, m	$4000 \leqslant m \leqslant 4500 \text{ kg}$

4.2   Aeroglide vs Aerocruise

This section will highlight calculated simulation differences between the aeroglide and aerocruise skip entry maneuvers. The aeroglide was described in Chapter II as being an un-powered pass through the upper atmosphere where the bank angle and angle-of-attack could be used to alter the inclination of a TAV. This maneuver will be compared to the thrust vectoring aerocruise, described as powered flight through the upper atmosphere. Nine cases were researched for each type of maneuver, with each case being progressively more restrictive to TAV capabilities, i.e., deceleration limits, heating rate, etc. Table 9 shows the variations between the cases studied. The constraints on the first case are set arbitrarily high so that this case acts as an unconstrained solution. The aeroglide maneuver sets a capability baseline for the simulation, where we can compare the additional Δi achievable by incorporating thrust vectoring.

Table 5 (given in Chapter III) lists the state constraints to the simulations with the exception that to improve the computation time the flight-path angle is constrained by the inequality, $-10° \leqslant \phi \leqslant 10°$. Figure 13 shows the trajectory through the atmosphere for the aeroglide simulation. The trajectory solution dramatically decreases the amount of time spent in the atmosphere after the second case; however this change does not dramatically impact the inclination change possible. Comparing Fig. 13 and Table 10, it can be shown that the differences in the inclination change possible is related to the TAVs ability to lower itself into the atmosphere. This can be observed in Case 9 where the inclination change sharply decreases with the increase of the minimum altitude achieved.

In Figs. 13 and 14, the trajectories for each of the nine cases is shown for the aeroglide and aerocruise, respectfully. The noticeable difference between the two figures is amount of time that is spent in the atmosphere as the problem is further constrained. In Fig. 13, the trajectories quickly transition solutions ending around 720s, to solutions ending between 300 and 400s. The opposite is true for aerocruise cases which slowly move leftward on the time axis as the problem is progressively restrained. In both solutions, the unconstrained case involves a long glide and a short, steep dip into the lower atmosphere. Further restricting the problem causes the flight path to shift towards a solution that resembles a "U" rather than a "V" shape. A more comprehensive look into Case 9 may allow for some deeper understanding of the differences between the aeroglide and the thrust vectoring aerocruise.

Table 8 lists the TAV constraints for this section with the following exceptions

- The mass of the aeroglide does not change and is set at 4500 kg

- The declaration, heating load, and heating rate limits are described in Table 9
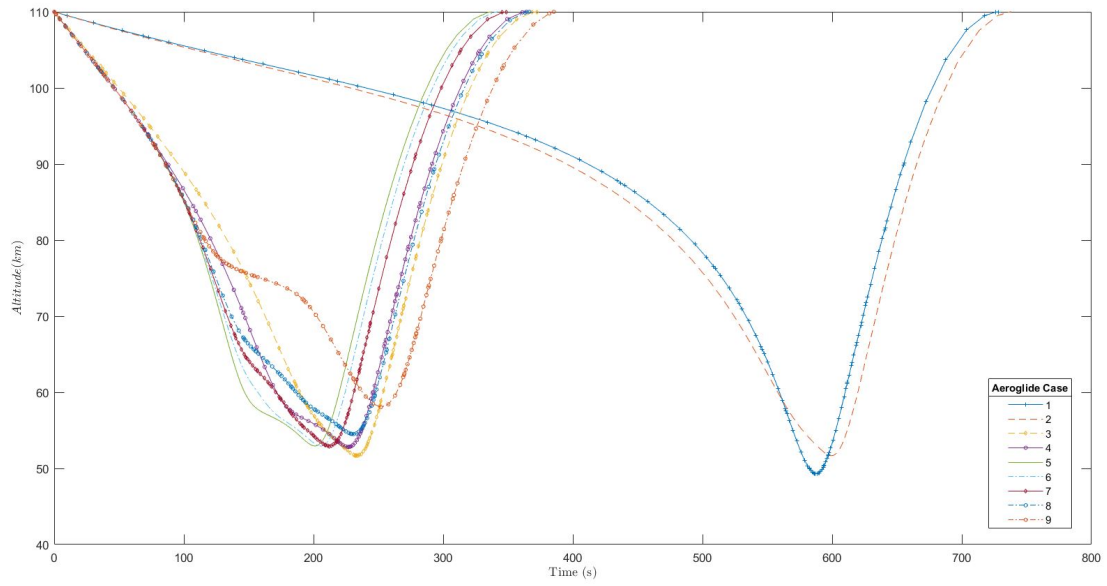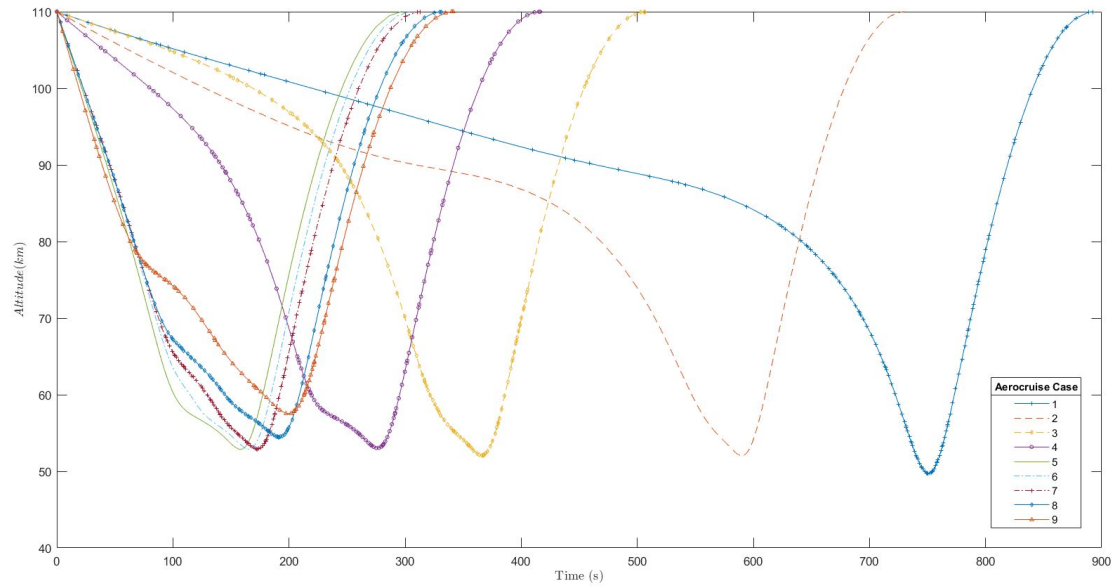
Figure 13. Aeroglide Flight Profile

Figure 14. Aerocruise Flight Profile

Table 9. Aeroglide vs Aerocruise Simulation Constraints

	Total Heat Load $\frac{MJ}{m^2}$	Heating Rate $\frac{MW}{m^2}$	Deceleration g_n
Case 1	1000	10	8
Case 2	300	2.5	5
Case 3	200	2	5
Case 4	200	2	4
Case 5	175	2	4
Case 6	175	1.75	4
Case 7	175	1.5	4
Case 8	175	1.25	3
Case 9	125	1	2

Table 10. Aeroglide vs Aerocruise Inclination Change

	Aerocruise	Aeroglide	Difference
Case 1	131.6	119.3	12.3
Case 2	130.5	118.2	12.3
Case 3	126.5	117.6	8.9
Case 4	125.1	116.5	8.6
Case 5	122.3	114.0	8.3
Case 6	121.6	113.4	8.2
Case 7	120.2	111.9	8.3
Case 8	115.7	106.9	8.8
Case 9	83.7	69.3	14.4

4.2.1 Trajectory Analysis: Case 9

This section takes a closer look at the different solutions between the aeroglide and the thrust vectoring aerocruise for the most constrained case. This section will highlight the differences between these two maneuvers; however, it is also appropriate to state that the research in this section significantly highlights the viability of skip entry maneuvers to alter the inclination of an orbit. In this highly constrained example the aeroglide achieved an inclination change of $69.3°$ without the use of any propellant through the atmosphere; by comparison, the aerocruise achieved an inclination change of $83.7°$.

Figure 15 shows the altitude profile for the aerocruise and aeroglide from the 9th case simulated. This case had the largest inclination change disparity, but the altitude flight-profiles appear very similar except for a time shift. The minor differences in the flight-profiles can actually reveal why the aerocruise is able to achieve a much larger inclination change over the aeroglide. The shape of both profiles can be explained by Fig. 16. The steep entry of both profiles is cut short by the deceleration limit, which causes a slight leveling off effect before another quick dip and lift out of the atmosphere. The slope of re-entry for aerocruise is much steeper than the aeroglide, and results from the initial trajectory angle being calculated as a free initial condition in the optimization software. The initial trajectory angle for the aerocruise and aeroglide was calculated as $-4.05°$ and $-1.69°$, respectively. The reason for this difference lies in the fact that the aerocruise can compensate for a loss of energy by thrusting. Once the solution reaches the deceleration rate limit, the thrust vector is used to augment the lift of the TAV. This change allows for a steeper entry, while also maintaining the deceleration limit. The thrust vector also shifts in the direction of the turn, which assists in providing additional force in the direction of travel. This can be deciphered from Figs. 17, 18, and 19. Specifically, Fig. 19 shows the bank

angle of the TAV, which is always positive and constant at $45°$ for the aerocruise case. This bank angle would indicate a right bank/turn on a non-point mass (see Fig.3 in Chap. III). Figure 20 confirms a turn to the right off of the equator and into the Southern Hemisphere, and depicts how the aerocruise is capable of a larger inclination change. Although the trajectories are similar, the aerocruise can use the thrust vector to influence the turn into the atmosphere.
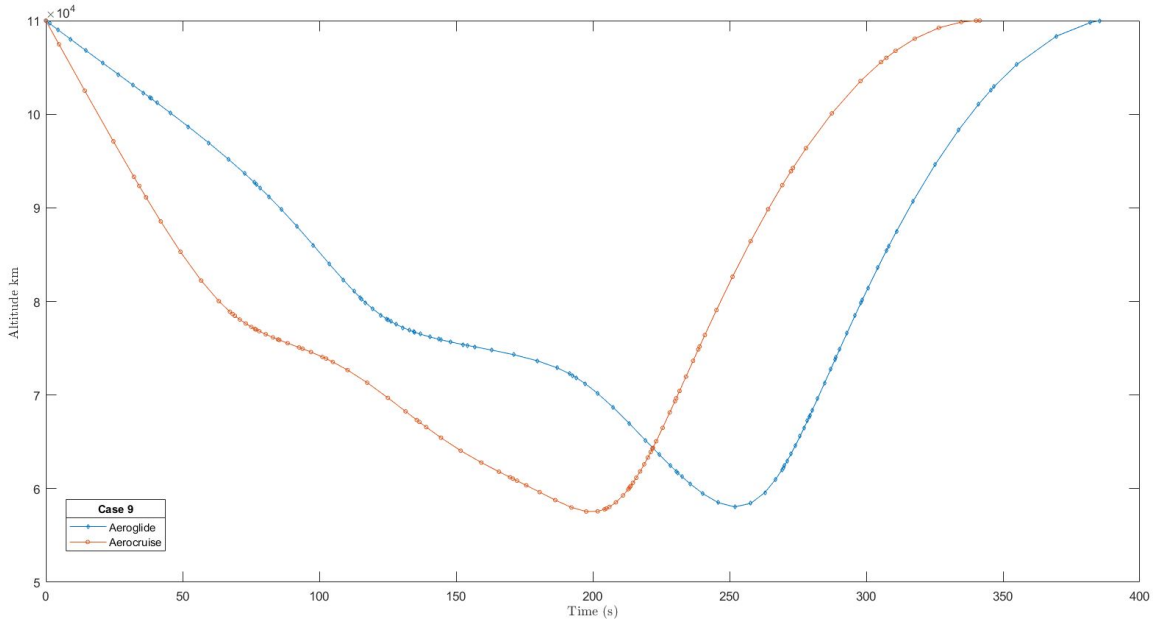

Figure 15. Altitude Flight Profile (Case 9)
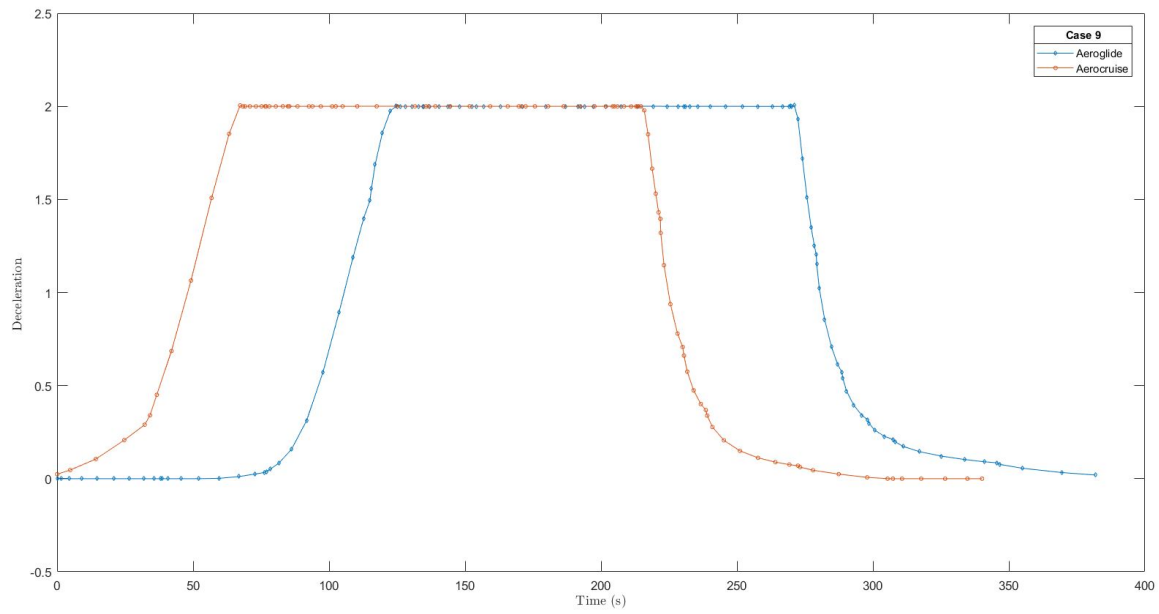
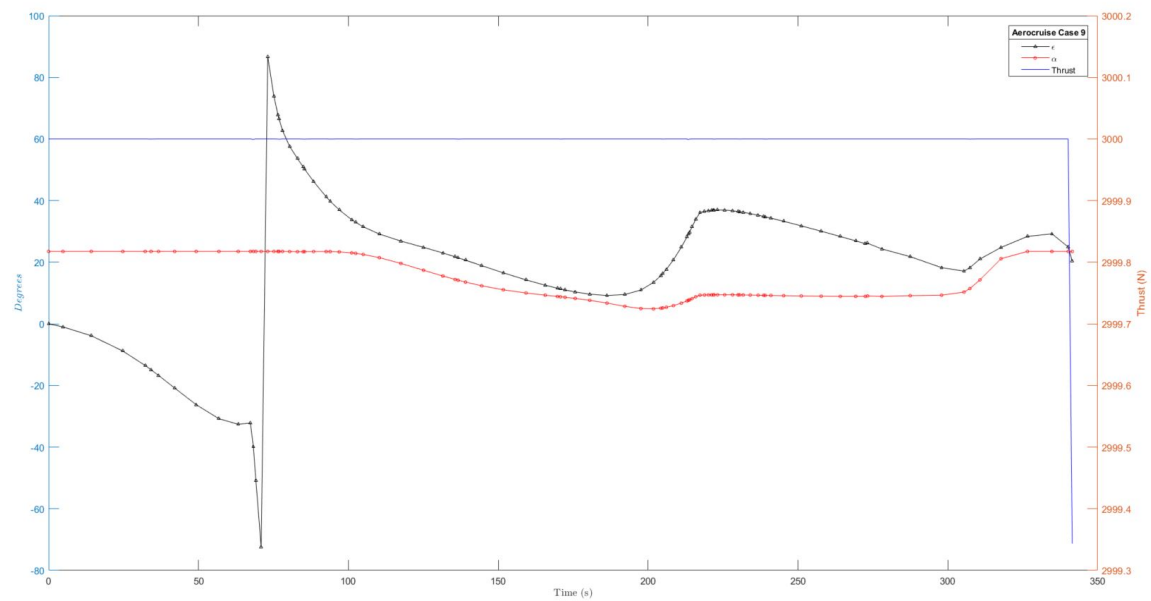**Figure 16. Deceleration Profile (Case 9)**

Figure 17. Thrust Vector Control Solution (Case 9)
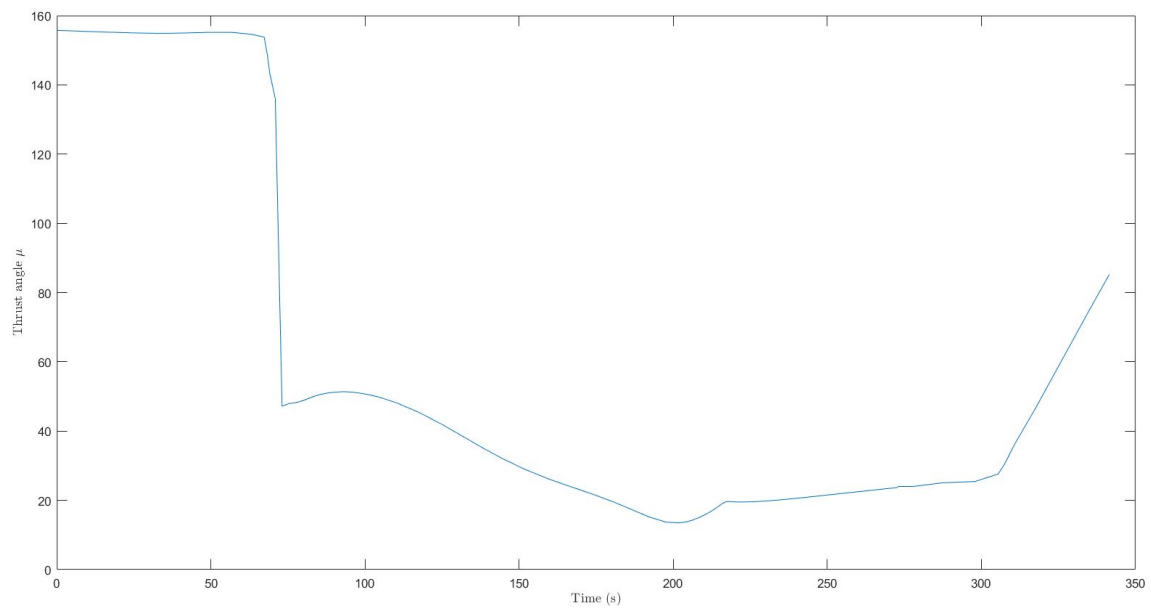
Figure 18. Thrust Vector Control Solution μ (Case 9)
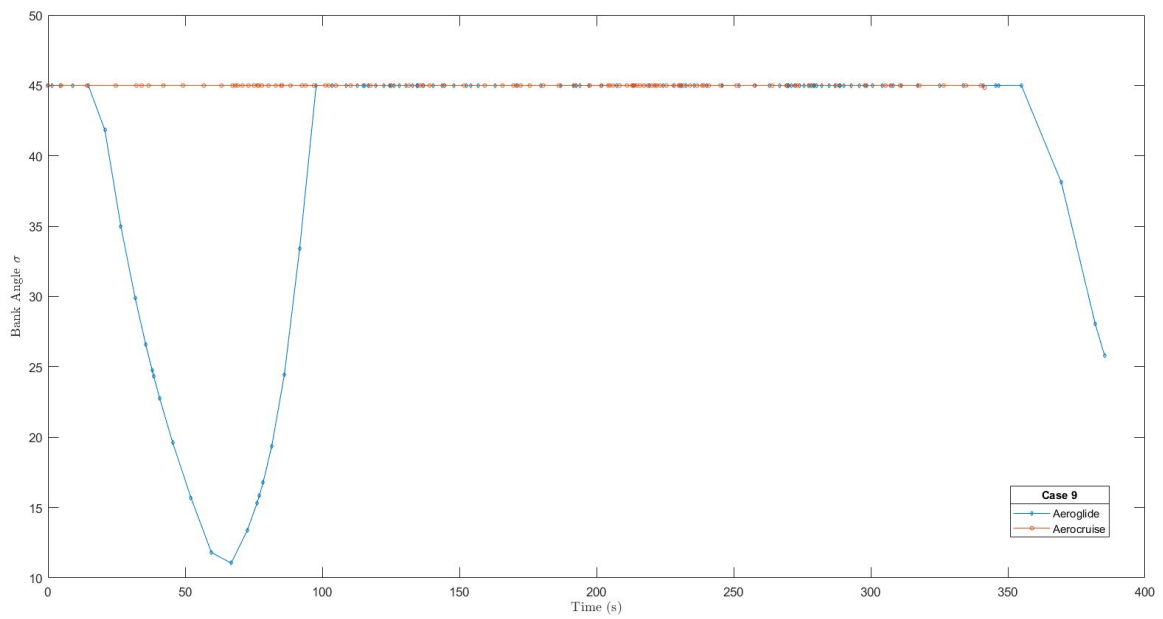

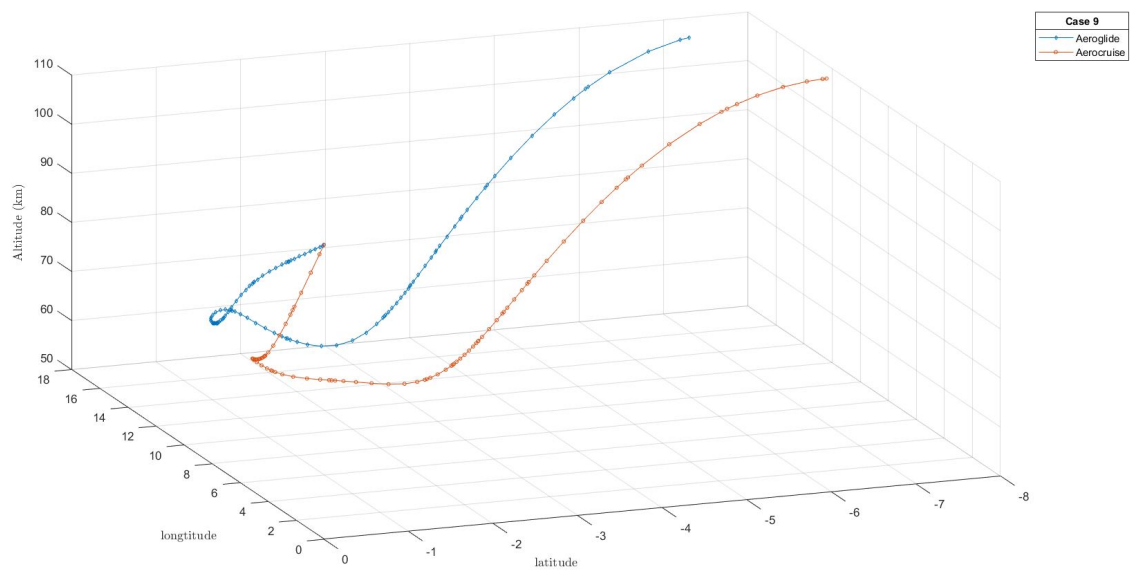**Figure 19. Bank Angle Solution σ (Case 9)**

51

Figure 20. 3-D Flight Profile for Aerocruise and Aeroglide Trajectories (Case 9)

4.2.2 Thrust Vector Angle Analysis

As discussed in Chapter 2, previous research of aerocruise maneuvers assume thrust equal to drag. The optimization of thrust vectoring simulations have not shown that thrust vectoring contained in the research herein has not shown equal to drag is indeed the optimal solution. Figures 21 and 29 (repeated figure for convenience), depicted the thrust vectoring solutions from Cases 1 and 9, respectively. These charts show that thrusting in the longitudinal plane is not the optimal solution. As discussed in Sec. 4.2.1, the thrust vectoring solution is often to thrust in the direction of lift, and in the direction of the atmospheric turn.

For Case 1, thrusting is not constant for the duration of the flight, and shown in Fig. 21, thrusting gradually increases between 100 and 500s. This solution, as well as all other solutions in this section, burn all available fuel to complete the maneuver. In Case 1 the trajectory segment before 500s achieves an inclination of change of $3.5°$. For Case 2, maximum thrust is reached at 300s, with $\Delta i = 2.5°$ up to this point. The Δi difference in this segment of the trajectory accounts for the entire Δi between the first two cases. The limiting constraints in Case 2 were the total heat load and deceleration. From research analysis presented in Sec. 4.3.5, the heat load is likely the more limiting of these factors. Alternatively, Case 3 has an unexpected thrust vectoring solution where the heat load and rate were further restricted, with the initial direction of the thrust vector aligned with the gravitational force, and in the direction of drag. This solution shows that the TAV needs to increase its energy loss in order to quickly lower itself into the atmosphere. The vector solution in Case 3 ends in a similar manner to Cases 1 and 2, using thrust to augment lift and exit the atmosphere. Case 4 shows a transition between Case 3 and 5, where the thrust vector briefly depletes energy in the beginning before augmenting the lift vector. Similarly, Cases 7 - 9 represented in Figs. 28-29, return to using the thrust vector as

an additional source of energy depletion. This is in response to quickly traversing the atmosphere and reducing the heat load while balancing the deceleration requirement thus causing a higher perigee altitude and a shallower trajectory slope.

Figure 30 shows the in-plane cant angle μ for all cases. For angles greater than $90°$ the thrust vector has some influence on the magnitude of the force against the direction of motion, or in the direction of the drag vector. If the angle is $180°$ then the thrust vector is completely in the drag direction. While Cases 4-9 begin in the drag direction, all solutions converge to a solution between $20 - 30°$ in the direction of the atmospheric turn. This result reinforces that the thrusting opposite to the direction of drag is not the optimal solution. A traditional TAV, with an engine thrusting opposite drag, may be designed to thrust near the optimal solution of $20°$. Cases 1 and 2 show how increasing allowable heat load dramatically improves performance. These cases have the lowest initial μ angle, which remains fairly constant after 100s until the end of the flight where the engine is out of fuel. The traditional TAV design may be adaptable to achieve the thrust vectoring solution given in Cases 1 and 2 but Cases 4-9 require a thrust vector beyond the scope of a single rear facing engine nozzle.
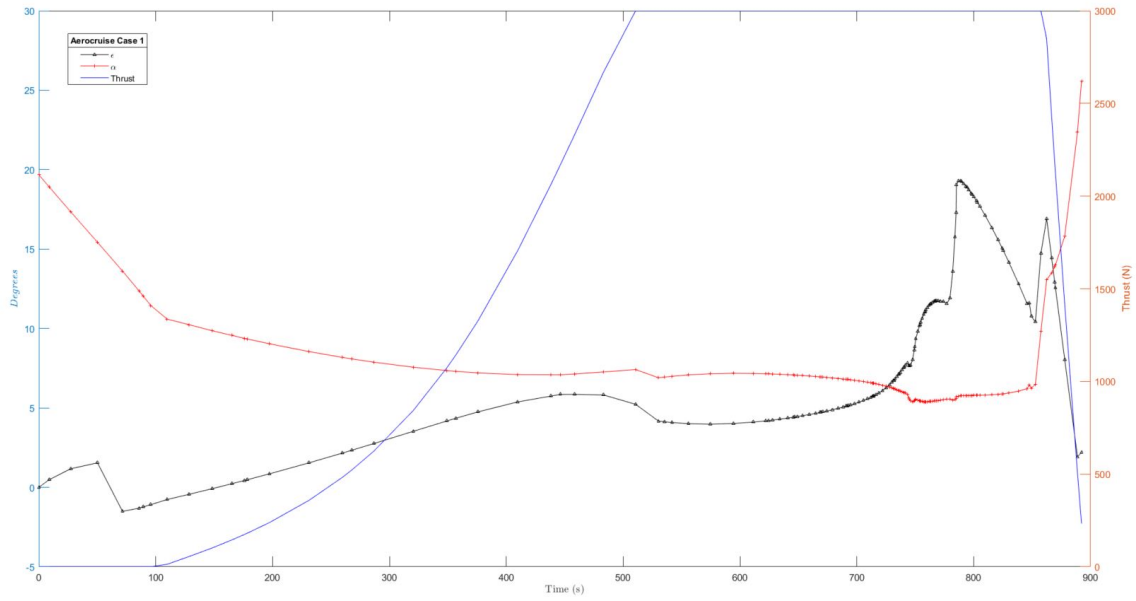
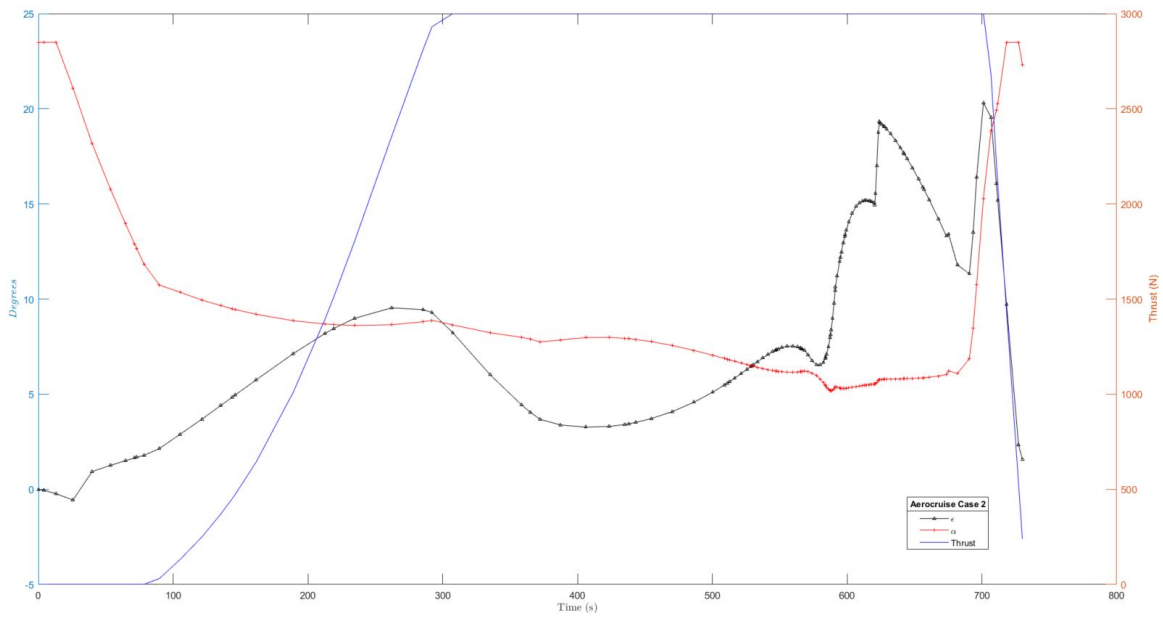**Figure 21.   Aerocruise Out-of-Plane Cant Angle (Case 1)**
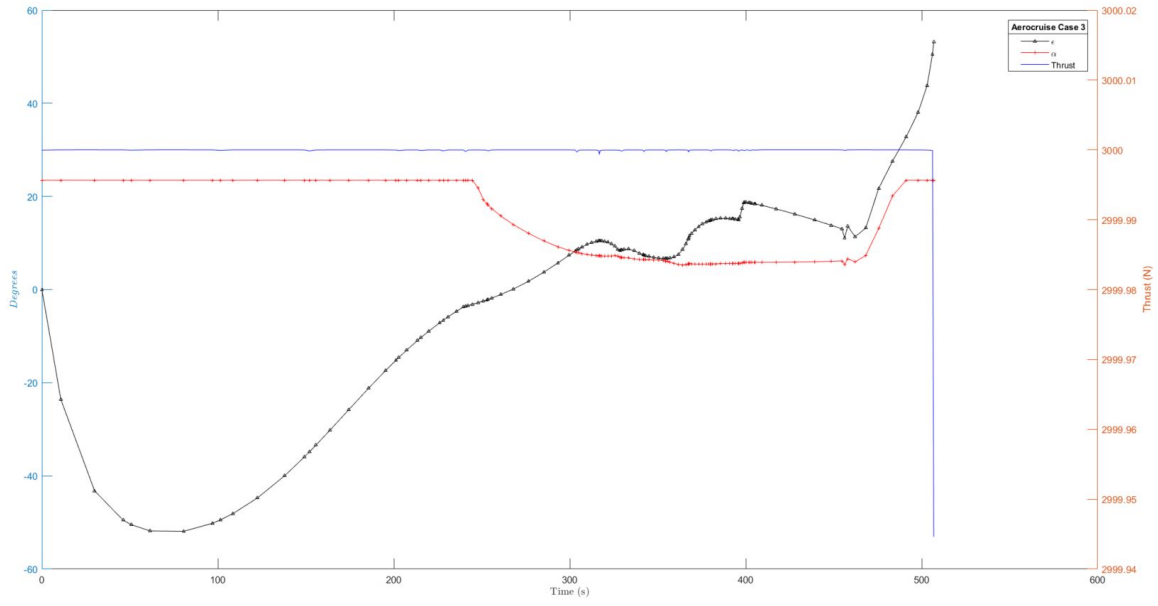

Figure 22.   Aerocruise Out-of-Plane Cant Angle (Case 2)

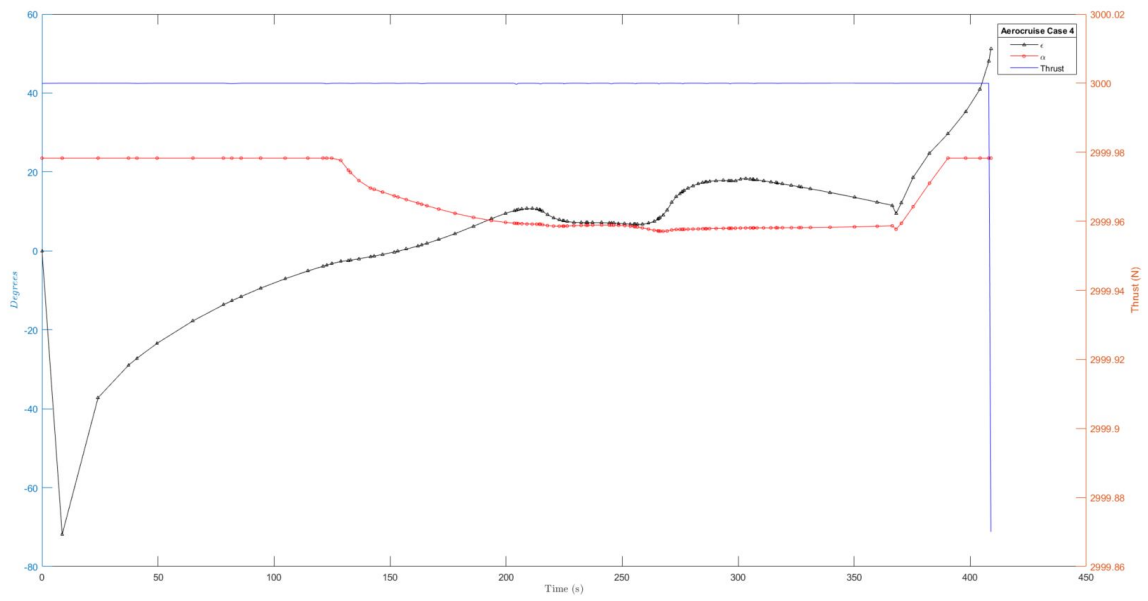**Figure 23.   Aerocruise Out-of-Plane Cant Angle (Case 3)**

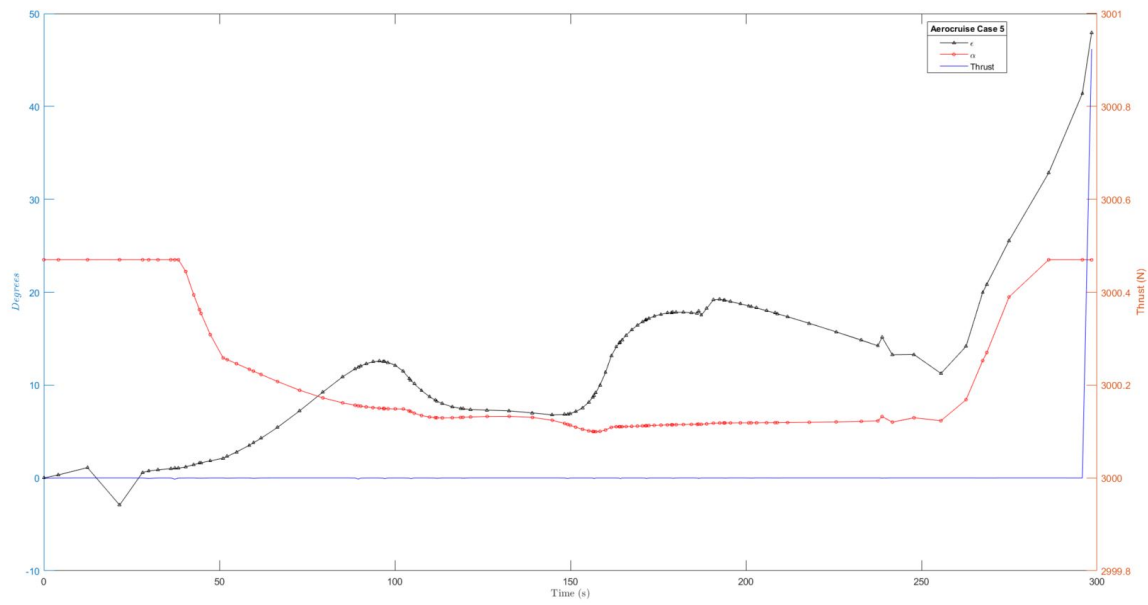**Figure 24.   Aerocruise Out-of-Plane Cant Angle (Case 4)**

Figure 25.   Aerocruise Out-of-Plane Cant Angle (Case 5)
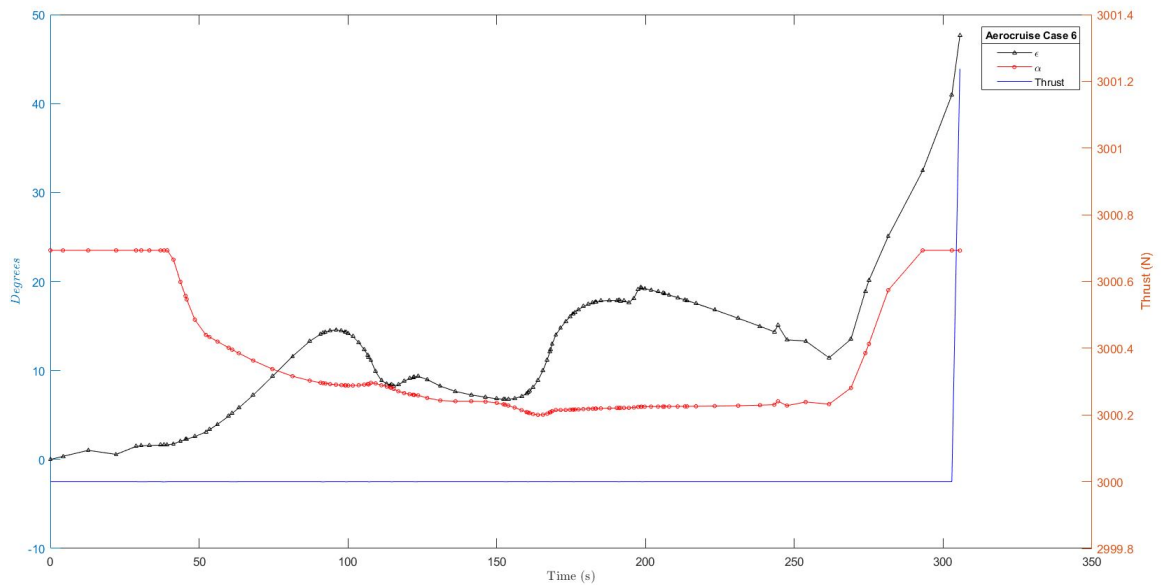

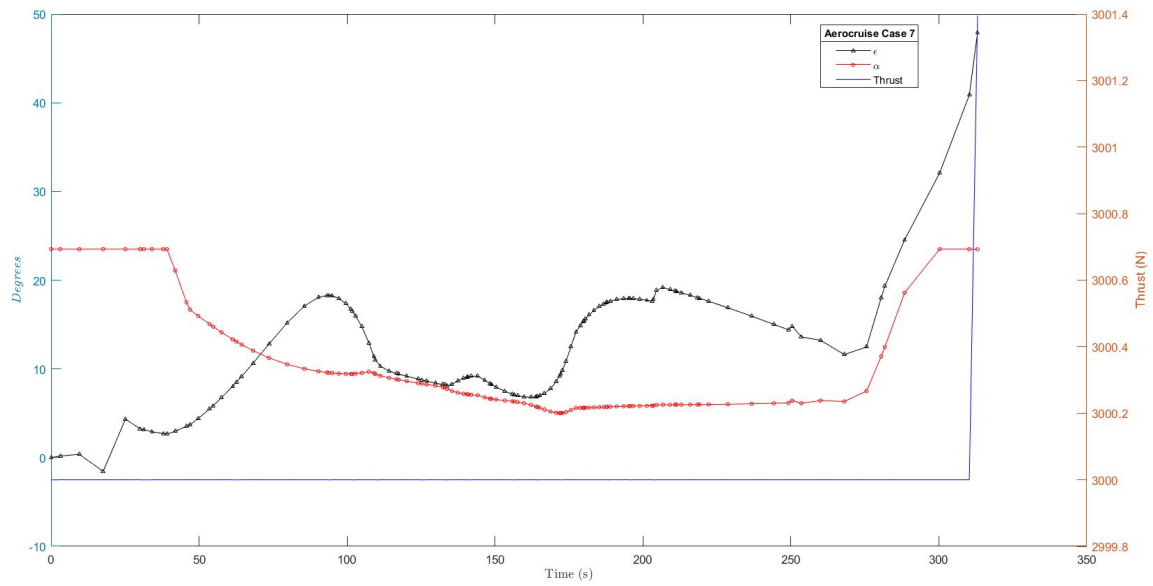**Figure 26.   Aerocruise Out-of-Plane Cant Angle (Case 6)**

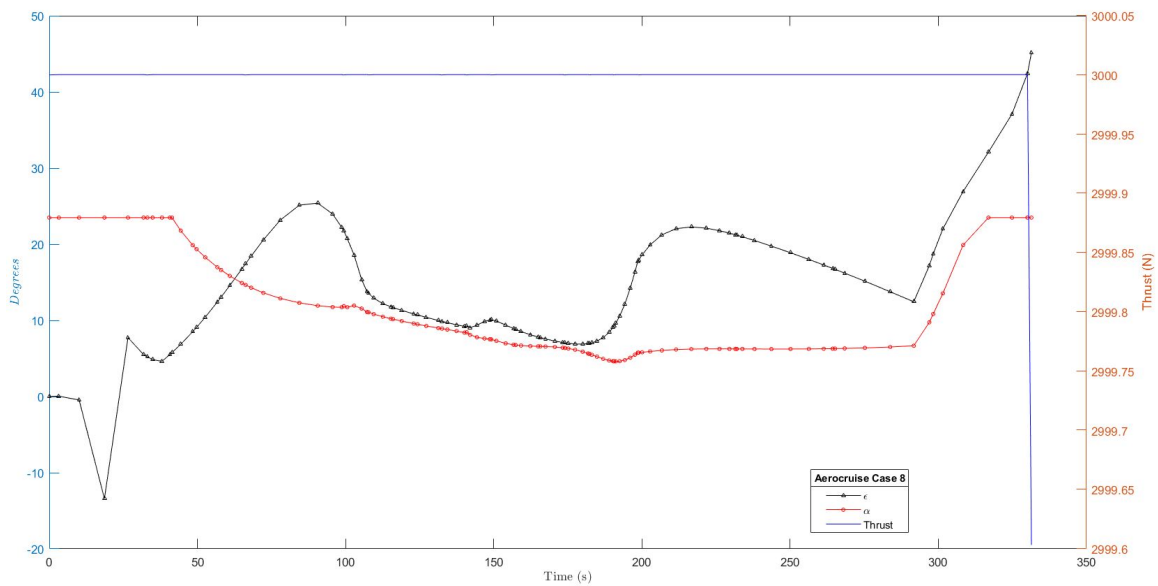**Figure 27. Aerocruise Out-of-Plane Cant Angle (Case 7)**
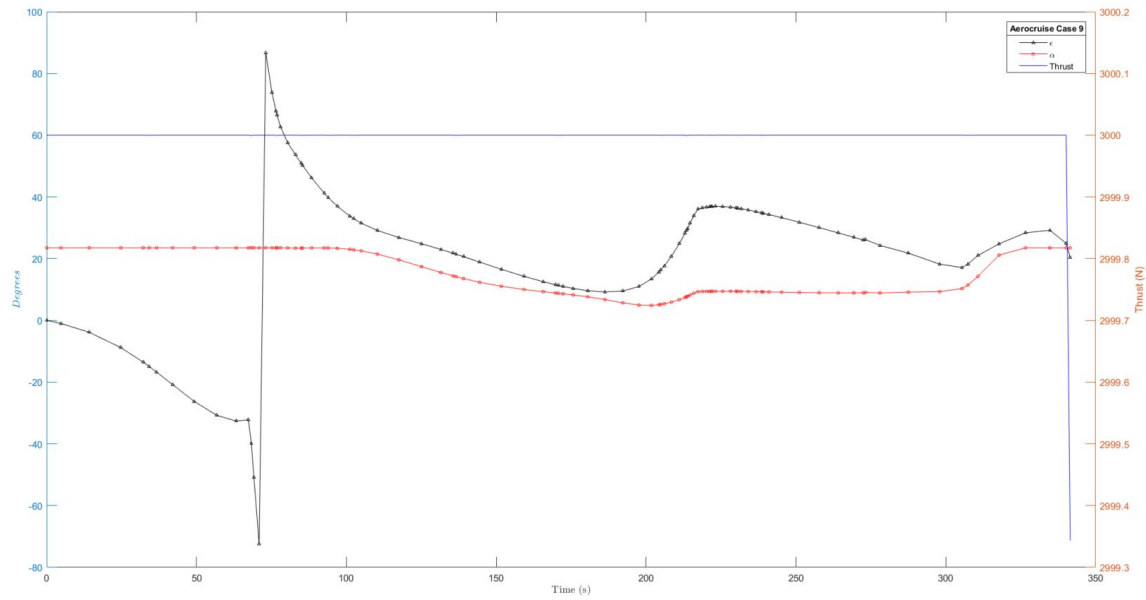

Figure 28. Aerocruise Out-of-Plane Cant Angle (Case 8)

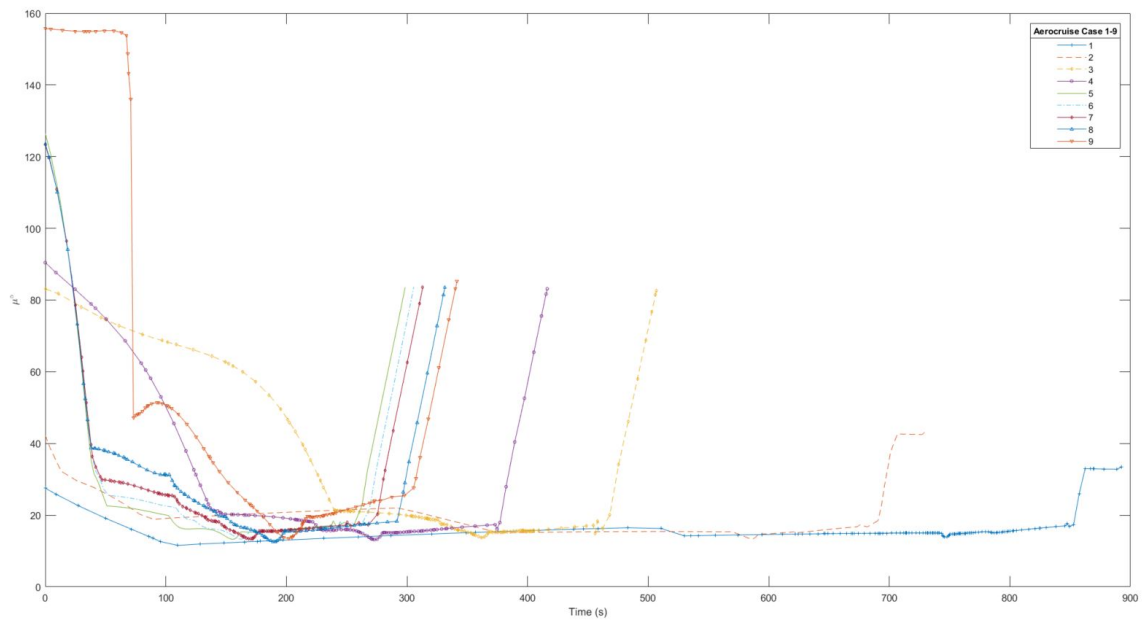**Figure 29. Aerocruise Out-of-Plane Cant Angle (Case 9)**

Figure 30. Aerocruise In-Plane Cant Angle (All Cases)

4.2.3 Limiting Energy Loss During Re-Entry

Perhaps the best reason to thrust during the skip entry is to maintain enough energy to escape Earth's gravitational pull and re-circularize in a LEO. Cases 1-9 allow the TAV to lose velocity down to 4 km/s. This is a significant loss of energy and would not be practical if all of the fuel has been expended, or if we have no fuel as in the aeroglide case. Therefore cases that constrained the final velocity were also studied for both the aerocruise and aeroglide maneuvers. Two cases for each maneuver type are compared below, with the final velocity to be $V_f \geqslant 6$ km/s and $V_f \geqslant 7$ km/s. The heating rate, deceleration, and total heat load limits for these cases are 2 MW/m^2,4 g$_n$, and 300 MJ/m^2, respectively. From Fig. 31, the aerocruise was able to maintain its initial velocity for a longer period of time which correlates to the late altitude drop in Fig. 32. From Fig. 33, it can be seen that decreasing V_f resulted in approximately a 20° difference in performance. Figs. 34 and 35 represent the thrust vector solutions where it is shown that the optimal thrust vector solution is to be approximately 10° off the longitudinal plane. In this study, the final inclination differences were roughly equivalent; the differences for the $V_f = 6.0$ km/s and $V_f = 7.0$ km/s were 11.04° and 10.66°, respectively.
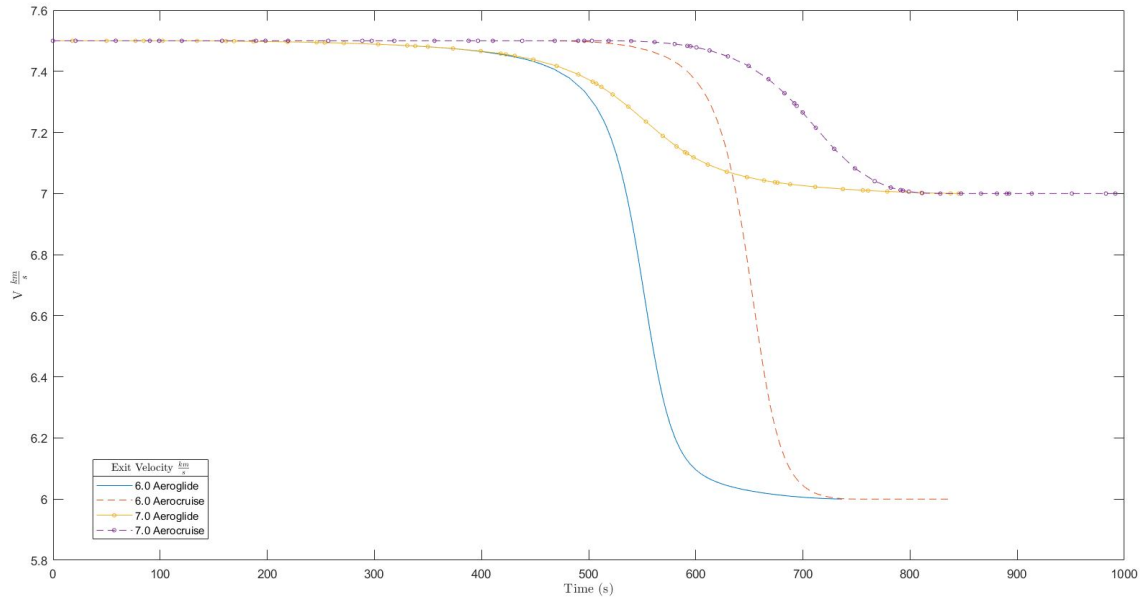
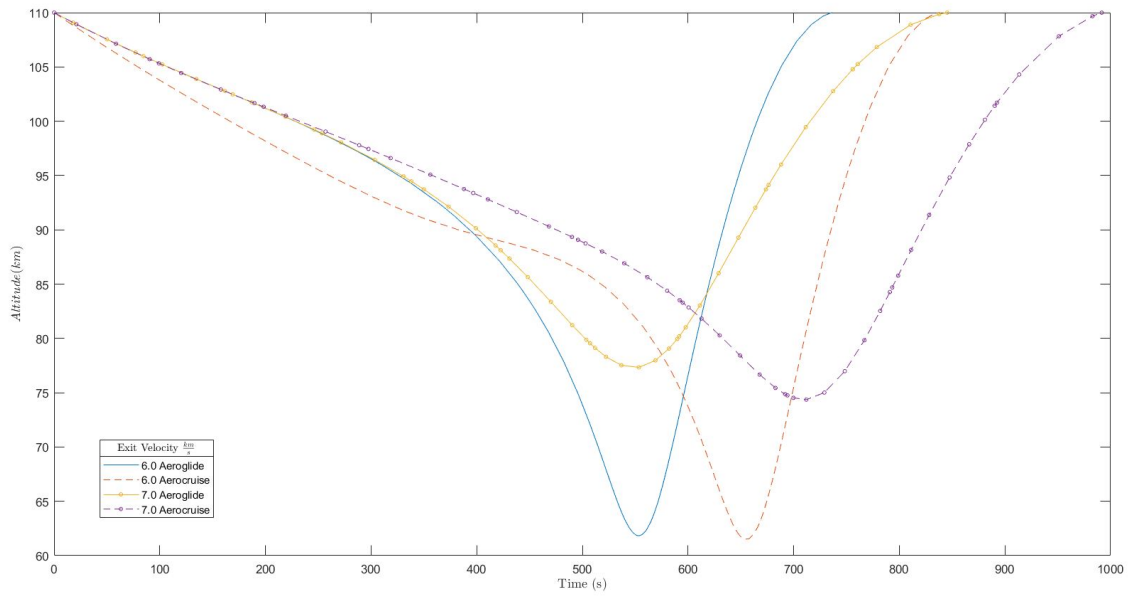**Figure 31. Velocity Loss During Skip Entry**

Figure 32. Altitude Profiles for Final Velocity Constrained Cases
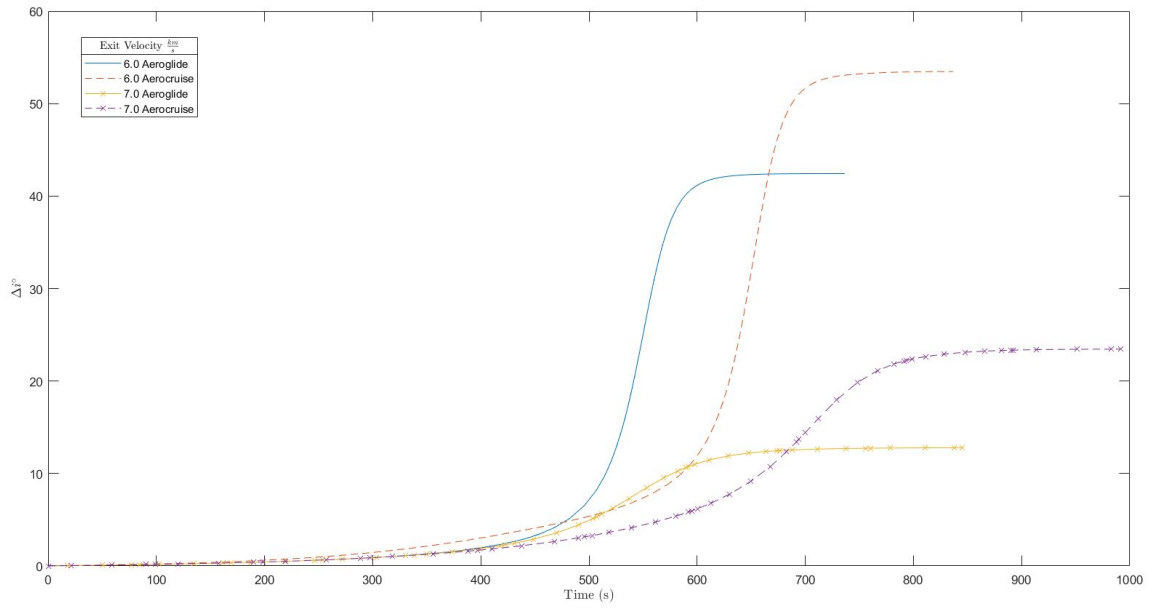
61

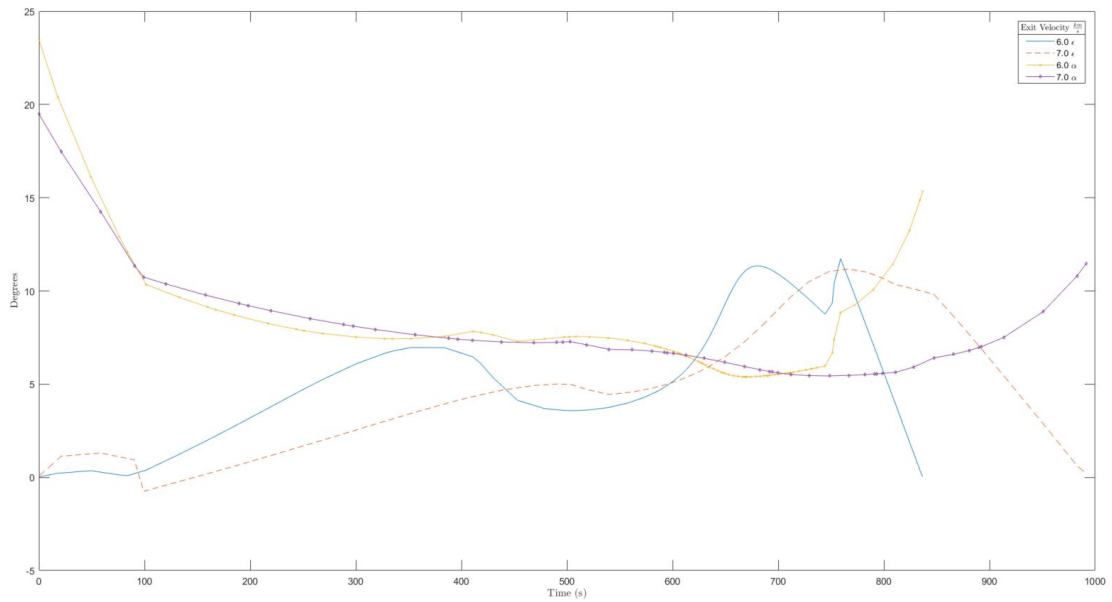**Figure 33. Inclination Change for Final Velocity Constrained Cases**

Figure 34. Out-of-Plane Cant Angle Compared to Angle-of-Attack
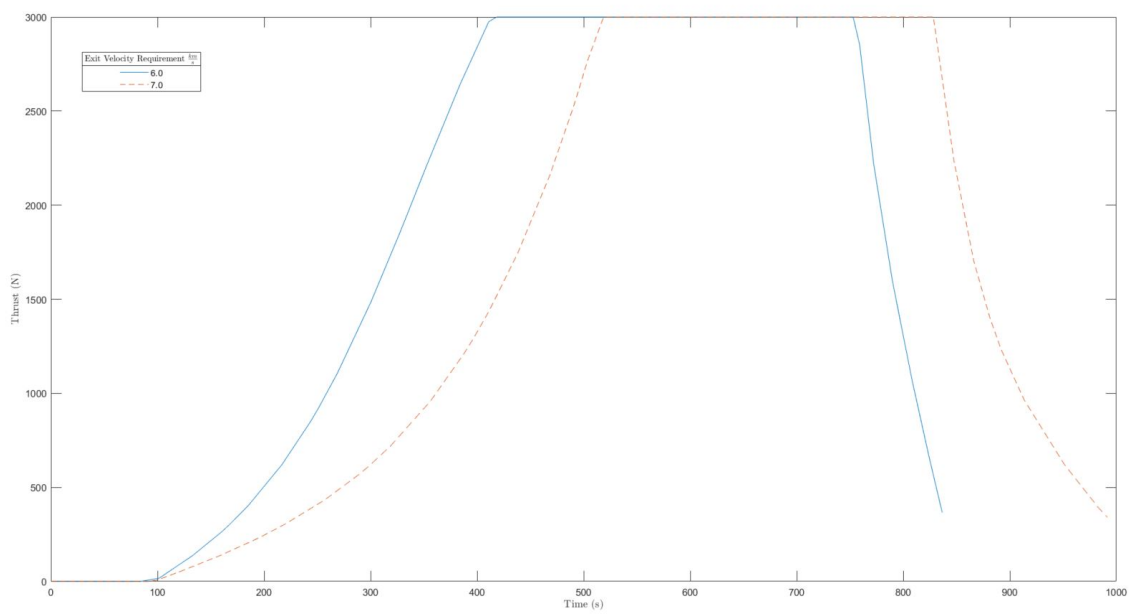
Figure 35.   Thrust Profile For Final Velocity Constrained Cases

4.2.4 Aeroglide vs Aerocruise: Summary

In this section it has been shown that the thrust vectoring aerocruise maneuver can increase the inclination change possible in a single skip entry. The thrust vectoring solution was studied thoroughly and it was shown that the optimal thrust vector solution is not opposite to the drag vector. Furthermore, it was shown that it was optimal solution, especially in the first few minutes, for thrust vectoring is in the direction of the drag and gravitational forces. Future sections will study the thrust vectoring aerocruise maneuver in more detail.

4.3 Study of How Design Constraints Affect the Thrust Vectoring Solution of the Synergetic Skip-Entry

This section will study the thrust vectoring solution exclusively. Each section describes which parameter is being varied, additional assumptions, TAV characteristic changes to Table 11, or state constraint modifications from Table 12 (repeated for convenience). The entry flight-path angle is free at the initial time. Also, the simulations upper altitude limit is 200 km allowing the TAV the ability to skip into and out of the atmosphere to reach the optimal solution.

Table 11. TAV Characteristics

Parameter	Value
Specific Impulse, I_{sp}	$310s$
Thrust, T	$3000N$
Reference Area, S	149.2 m^2
Deceleration Limit	8 g$_n$
Max Heating Load, q	$1000\frac{MJ}{m^2}$
Heating Rate Limit, $\dot{Q}$	$10\ \frac{MW}{m^2}$
Initial FPA, ϕ_0	$-20° \leqslant \lambda \leqslant 0°$
Initial Velocity, V_0	$7.5\frac{km}{s}$
mass, m	$4000 \leqslant m \leqslant 4500$ kg

Table 12. State Constraints

Parameter	Value
Position, r	$R_\oplus \leqslant r \leqslant 200(km)$
Velocity, V	$4 \leqslant V \leqslant 9(\frac{km}{s})$
Flight Path Angle, ϕ	$-20° \leqslant \phi \leqslant 20°$
Azimuth, A	$0 \leqslant A \leqslant 360°$
latitude, δ	$-90° \leqslant \delta \leqslant 90°$
longitude, λ	$0 \leqslant \lambda \leqslant 150°$
mass, m	$mass_{min} \leqslant m \leqslant mass_{max}$
time, t	$0 \leqslant t \leqslant 2000s$

4.3.1 TAV Structural Mass Variation Study

The first sub-section will compare solution results from varying the TAV initial mass from 4,500 kg to 15,500 kg, while keeping the propellant mass at 500 kg. All other parameters will be equivalent to Table 8. Figure 36 shows the resulting trajectories, which are similar to cases in the previous section featuring a long gliding entry, and dramatic dip. From previous study these features indicate a case where the heat load has not been constrained.

Looking at the flight-path angle throughout the simulation confirms a strong similarity between the trajectories. The initial flight-path angle varies slightly between the cases, but are otherwise indistinguishable. Figure 37 shows the inclination over time, and indicates the amount of inclination change is achieved by the steep dip into the atmosphere. It may first appear that a heavier TAV is just as capable to perform skip entry maneuvers as lighter TAVs given the same fuel mass, but a study of other parameters may reveal that heavier TAVs will be encumbered by other constraints more so than lighter TAVs. Interestingly, the lighter TAV achieves a greater inclination change with a higher perigee. It was discussed in Sec. 4.2 that a lower perigee height corresponded to a higher inclination change, but here the opposite is true due to the increase in mass.

One quantity that does not benefit a heavier mass is the aerodynamic heating. The limit on constraints other than those being studied were set arbitrarily high so that an accurate picture of changes to the solution caused by the parameter being studied could be observed. The more mass the TAV has, the higher the heating rate climbs in the simulation. Figure 39 shows the heating rate over time for all cases. The 15,500 kg simulation peaks at approximately 4 MW/m^{2}s while the 4500 kg case peaks at approximately 2 MW/m^{2}s. This is a large difference between the two cases and from a design standpoint it can be argued that lower mass requires less thermal

protection. The integral from Eq. (3.38) can be taken to calculate the total heat load to the TAV. The total heating load for each case is given in table 13, with each decrement in mass shown to reduce the total heat energy absorbed during re-entry.

Overall, the TAV structural mass study illustrated that lighter TAVs will have lower heating rates, heat load, and can achieve greater inclination changes for a single skip entry.
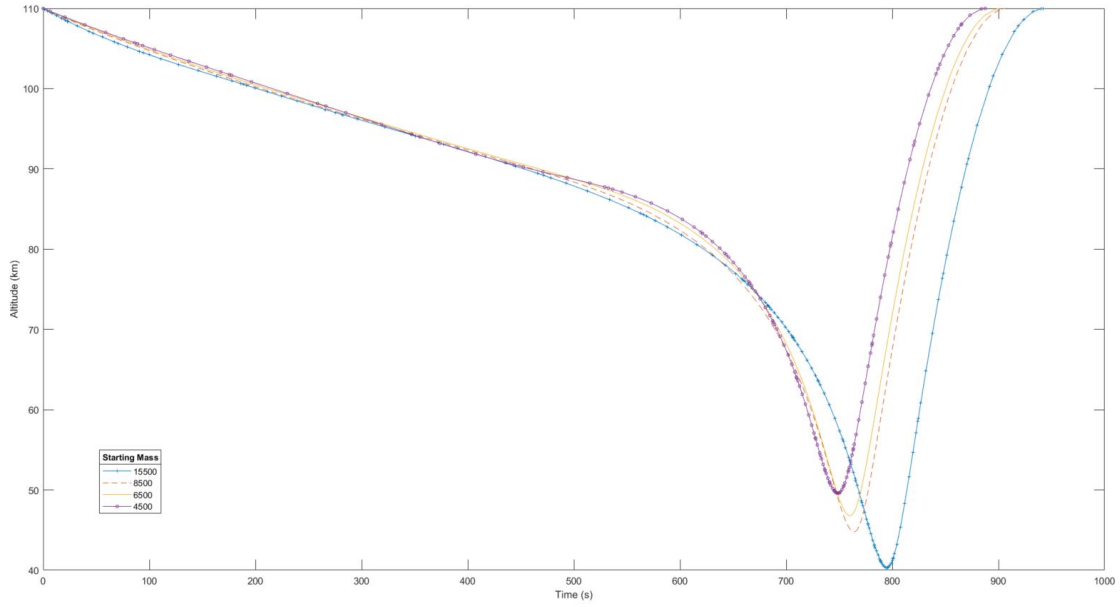

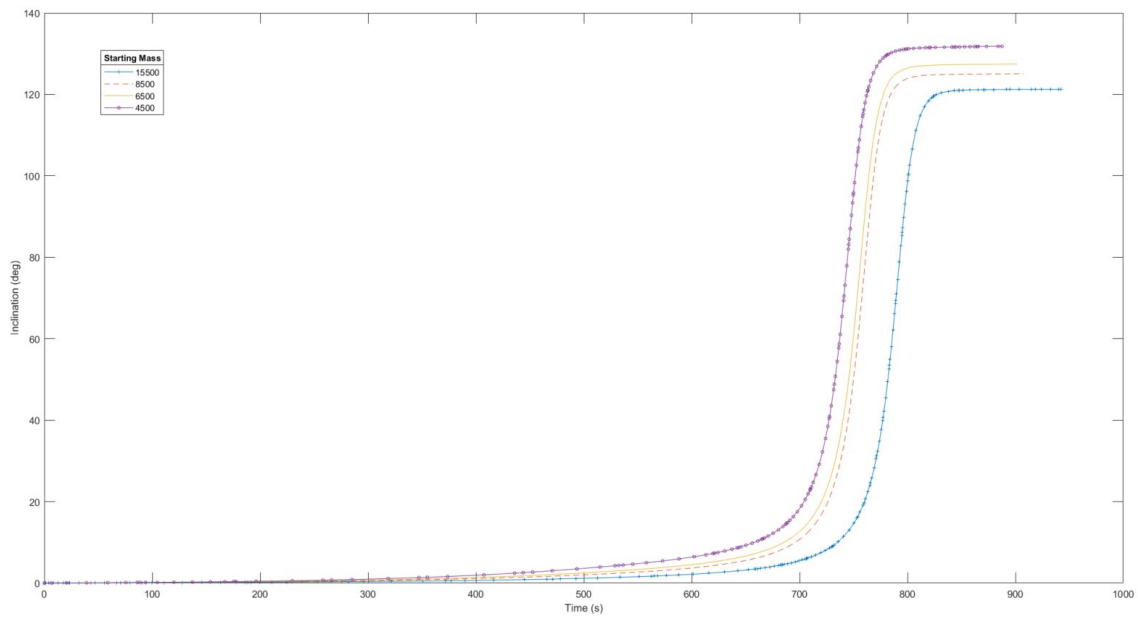Figure 36. Structural Mass Study: Altitude Trajectory

Figure 37. Structural Mass Study: Inclination Change
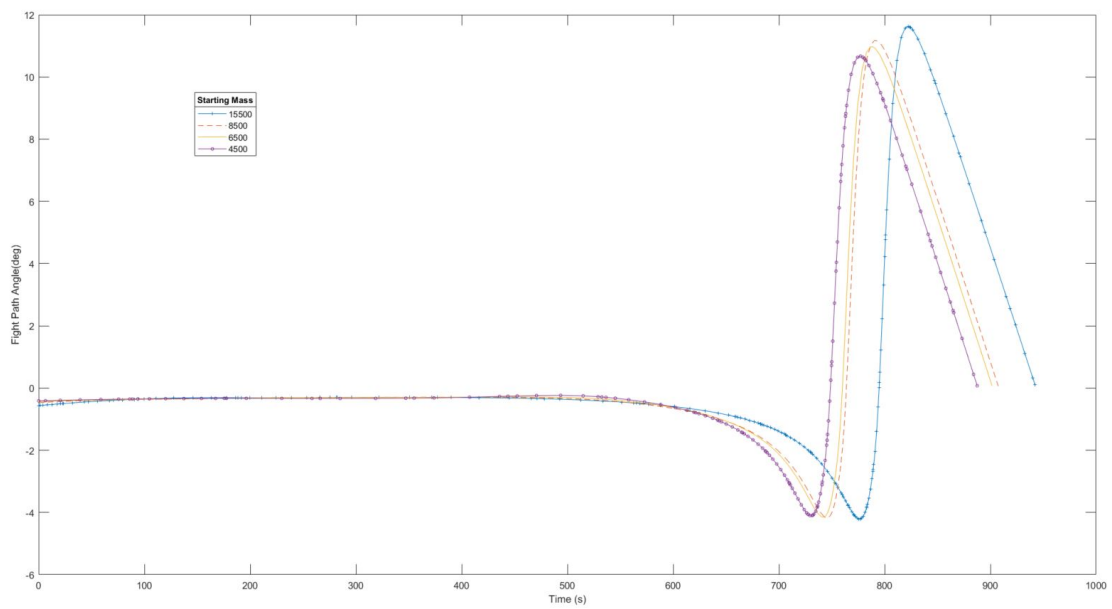
Figure 38. Structural Mass Study: Flight-Path Angle
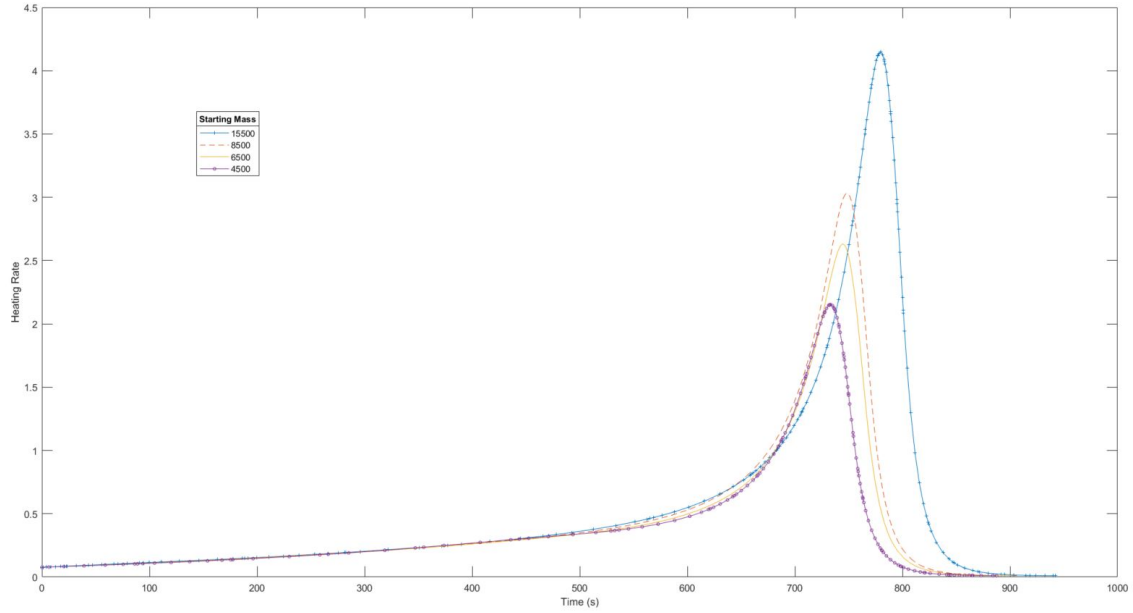
Figure 39. Structural Mass Study: Heating Rate

Table 13. Structural Mass Study: Total Heat Load

Starting Mass (kg)	Total Heat Load $\frac{MJ}{m^2}$
15500	513.624
8500	402.340
6500	365.211
4500	322.161

4.3.2 TAV I_{sp} Variation Study

This section will research varying the specific impulse (I_{sp}) from 300-2000 s. Table 12 describes the state constraints used for this section with two exceptions: The longitudes upper bound is 500°, and final time was changed to 5000s. These changes were made after initial research showed that 2000 s was not enough time to expend all available fuel at higher I_{sp}, a change in time may lead to a change in the longitudinal distance covered so this parameter constraints was increased.

Figure 40 shows the trajectory for the I_{sp} varying cases studied. For cases where the $I_{sp} \geqslant 700$ s the TAV makes two distinct skips into the atmosphere which significantly increases the inclination change possible. By increasing the I_{sp} and the time allotted for flight the final inclination achievable is nearly a complete reversal in the initial orbital motion. This is achieved through a combination of "best case" scenarios and with an I_{sp} and thrust combination that does not currently exist with current technology. However, an $I_{sp} = 400$ s with a max thrust of 3000 N is an achievable range for a chemical rocket engine, where a prograde to retrograde maneuver is still possible according to this simulation but with the trade off of high energy losses.

A study of the thrust vectoring solutions for these solutions reveals some interesting results not observed in other sections. As the TAV becomes more fuel efficient, the solution trends towards longitudinal thrust vectoring in the in-plane solution. Figure 41 shows the in-plane thrust vectoring solution for the $I_{sp} = 500$ s case this solution is similar to the results in other sections where the heat load is reduced. As the I_{sp} and total number of skips increases, the thrust vector solution aligns the thrust vector nearer to the longitudinal plane as shown in Fig. 43. Finally, a common trend observed during atmospheric exit is to increase the thrust's influence on the lift vector, regardless of I_{sp}.

This sub-section has shown the influence of high I_{sp} on the potential inclination change. Increasing I_{sp} in current day engine design typically reduces the available thrust which would impact the results of this study.

Table 14. Inclination Change for Varying I_{sp}

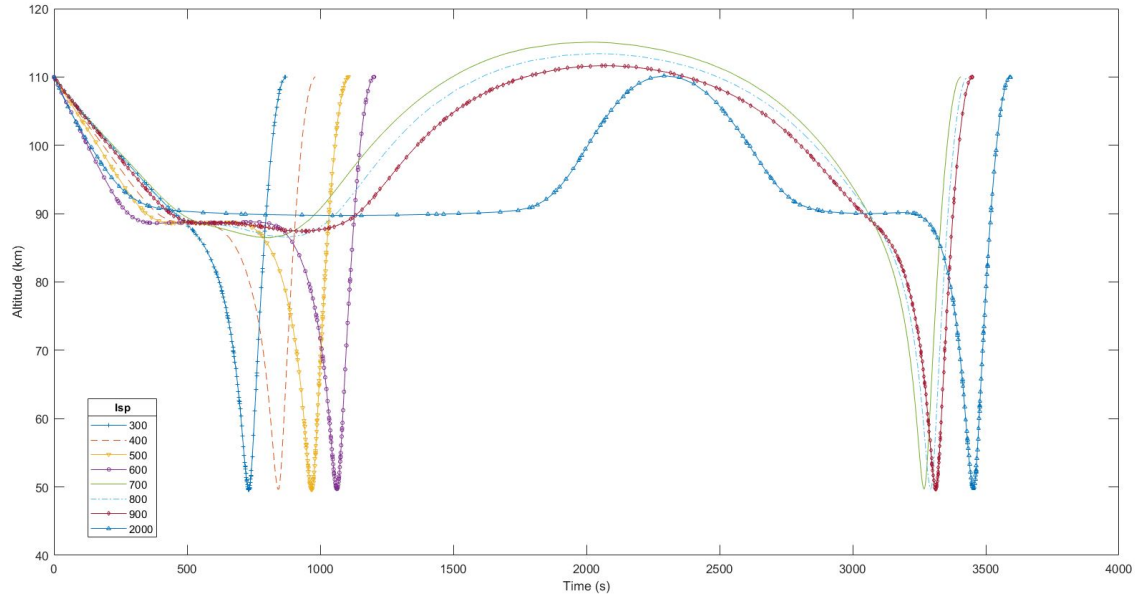| I_{sp}	Δi°	I_{sp}	Δi°
300	131.5	700	144.4
400	134.2	800	147.4
500	136.4	900	150.3
600	137.9	2000	168.0

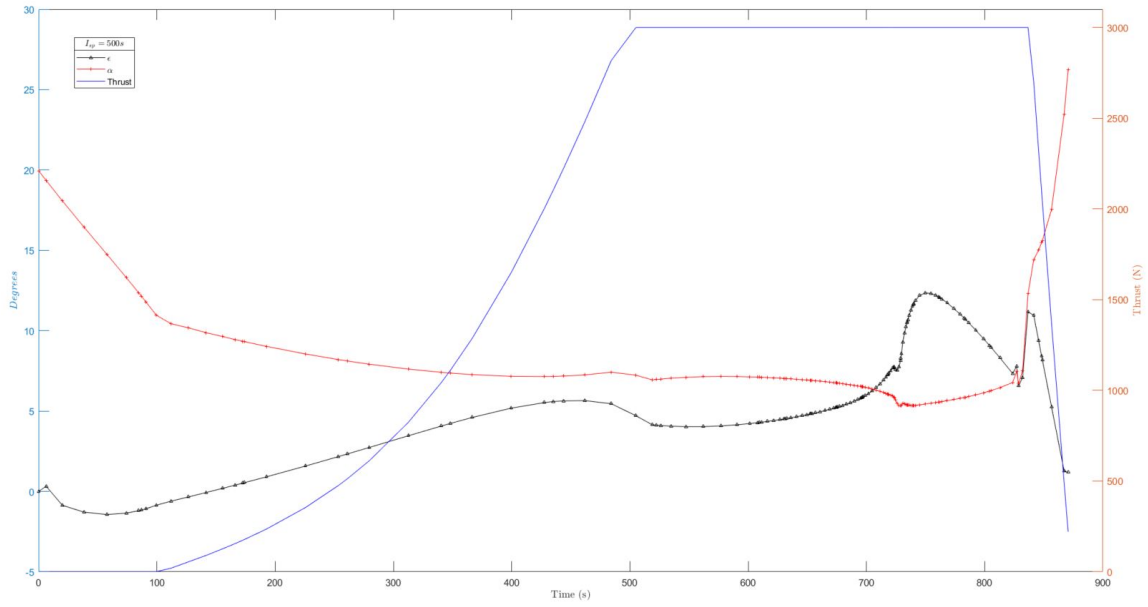**Figure 40.   Altitude Profile for Varying I_{sp}**

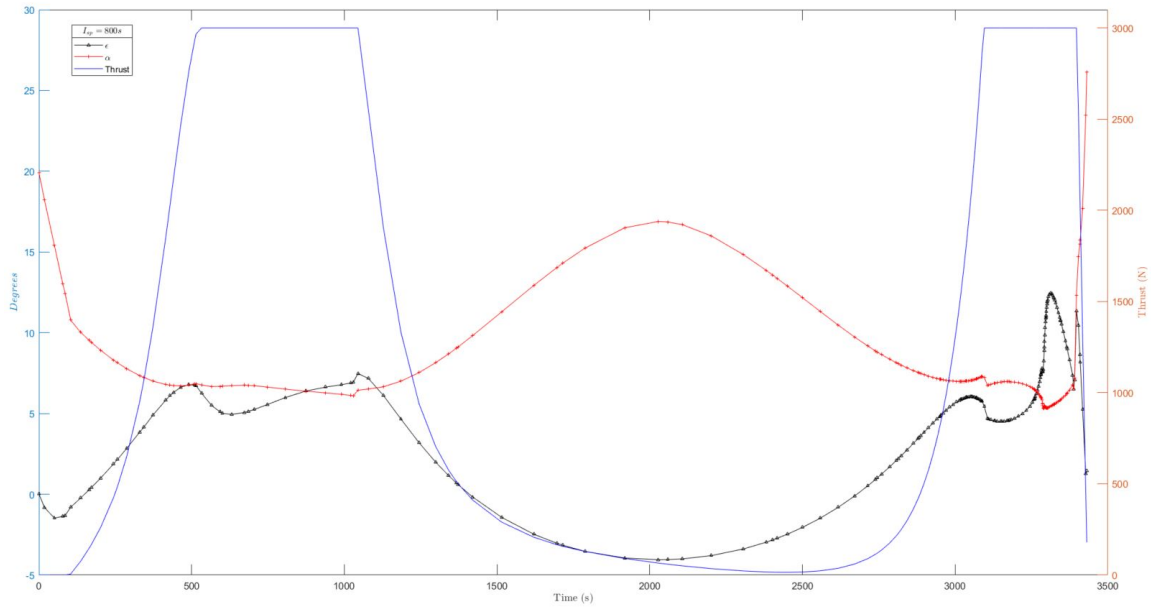**Figure 41.** Angle Comparison, $I_{sp} = 500 \ s$

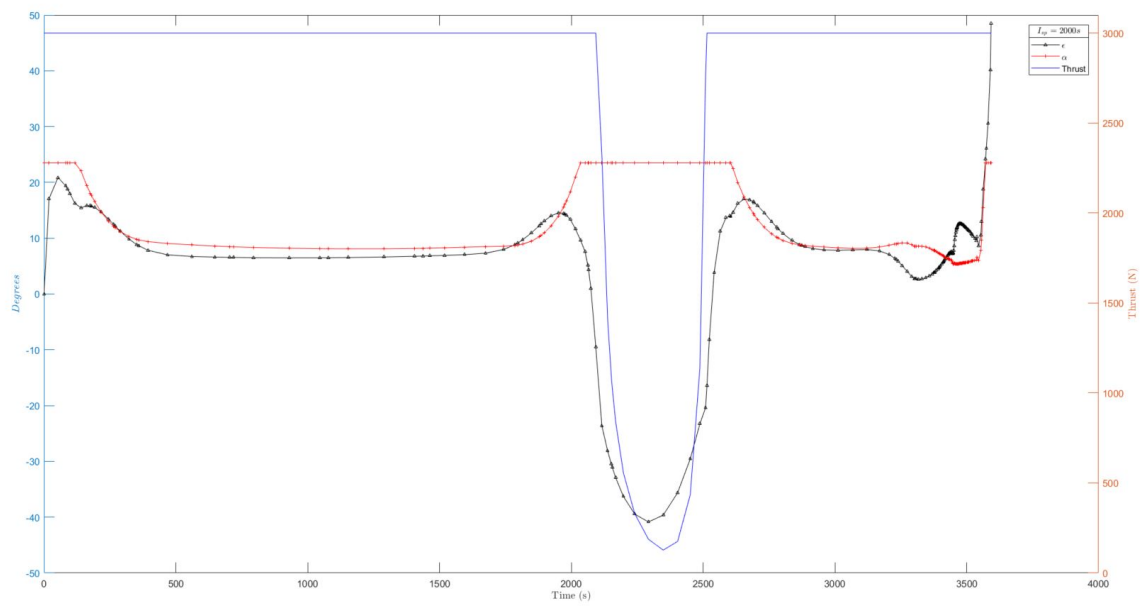**Figure 42.** Angle Comparison, $I_{sp} = 800 \ s$

72

Figure 43. Angle Comparison, $I_{sp} = 2000\ s$

73

4.3.3   TAV Deceleration Load Study

This subsection studies the impact of constraining TAV deceleration with limits of 8-2 times the force of Earth's gravity (g_n). Figure 44 shows the trajectory profile where as the g_n limit increases (8-2 g_n), the trajectory begins to flatten and the perigee altitude increases. This is similar to trajectories in Sec. 4.2 where the g_n increased. Figure 45 shows the velocity decrease through the maneuver and the subtle change that increasing the gravitational limit imposes on the velocity drop. The deceleration constraint also lowers the heating rate on the TAV as shown in Fig. 46. Table 15 compares the total heat load from each case which increases slightly as the deceleration limit increases, but all cases have significantly lower heat loads than those calculated from the Apollo 10 simulation. Interestingly the deceleration rate constraint does not significantly impact the inclination change possible. The final achievable inclination change for the maneuvers are 131°, 130°, 125°, respectively.

The thrust vectoring solution for the final case is shown in Fig. 47 which is nearly identical for all cases studied in this section with thrust gradually increasing during the initial glide before reaching full power at perigee. The thrust vector, ϵ, is mostly positive and increases at perigee point for the final rise out of the atmosphere.
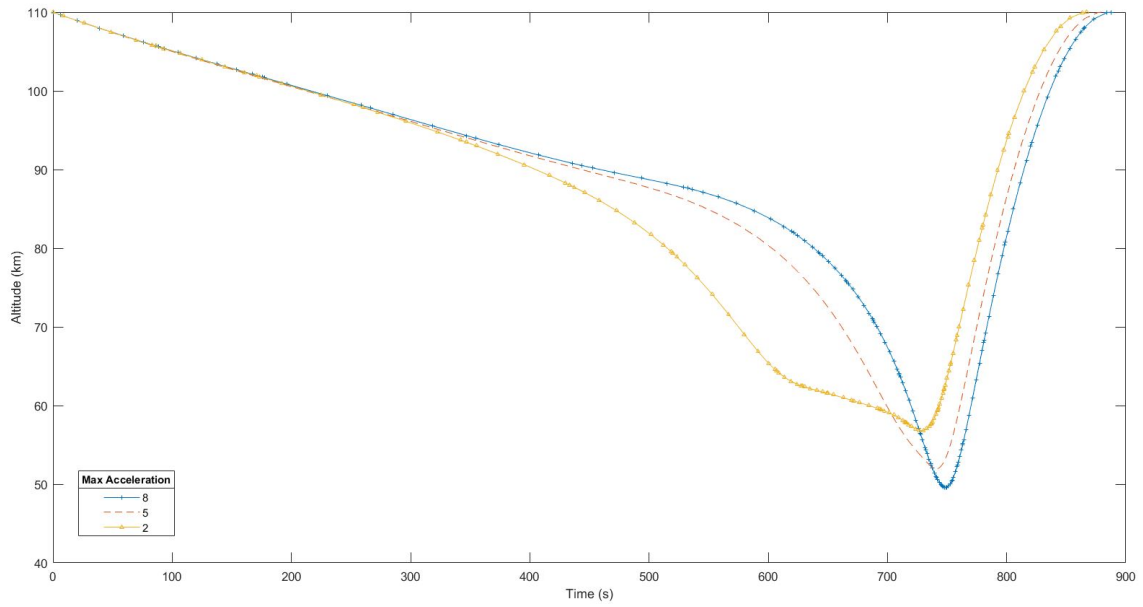
Figure 44. Altitude Profile for Varying Deceleration Limits g_n
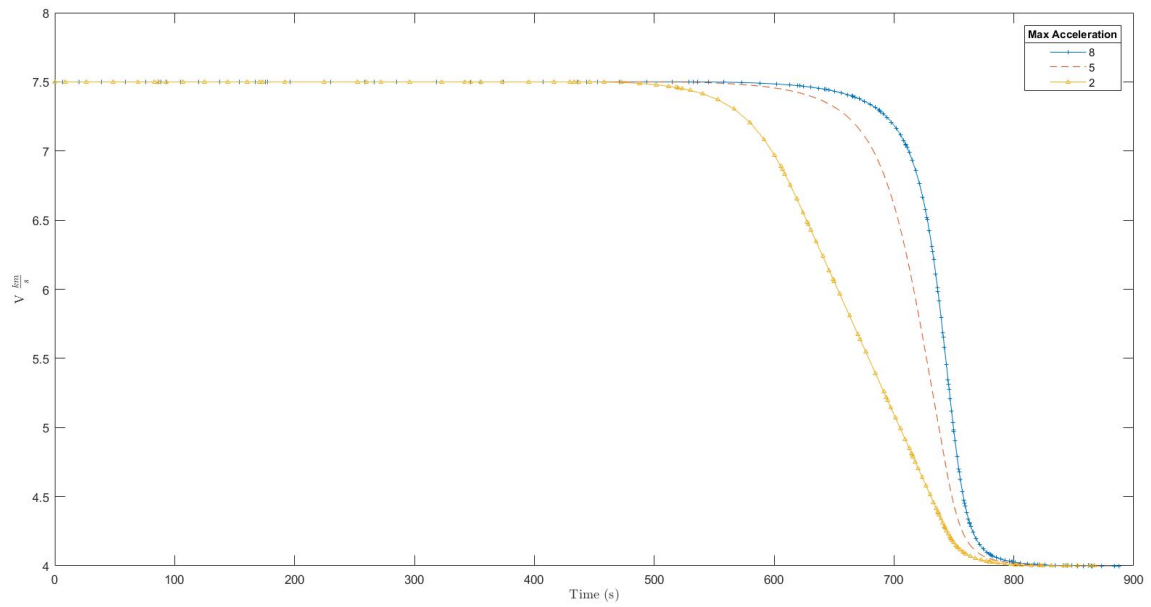
Figure 45. Velocity for Varying Deceleration Limits
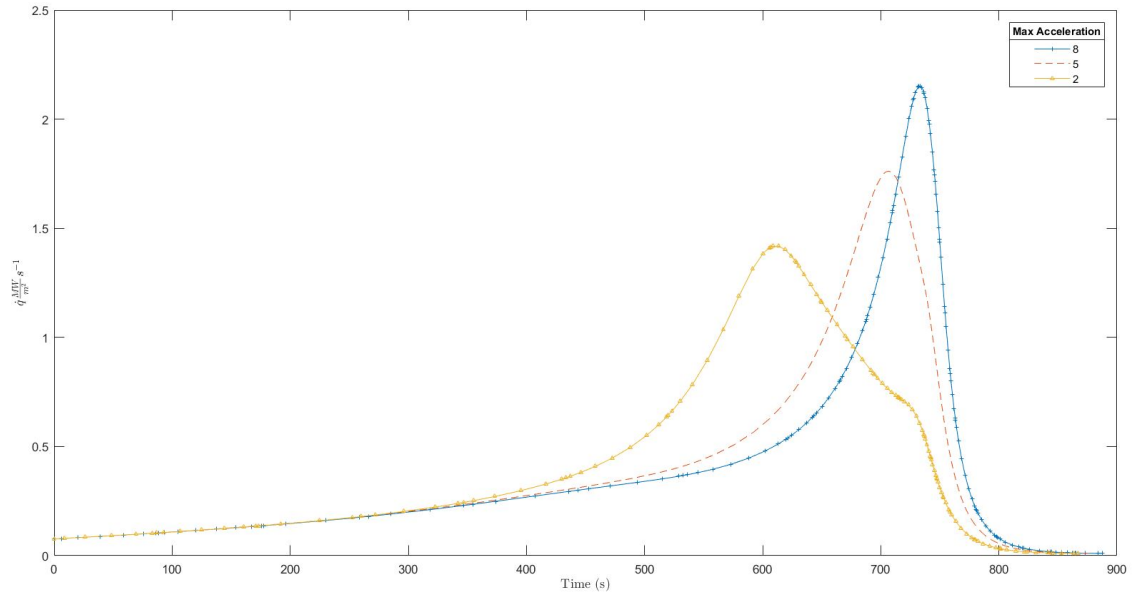
Figure 46. Heating Rate for Varying Deceleration Limits
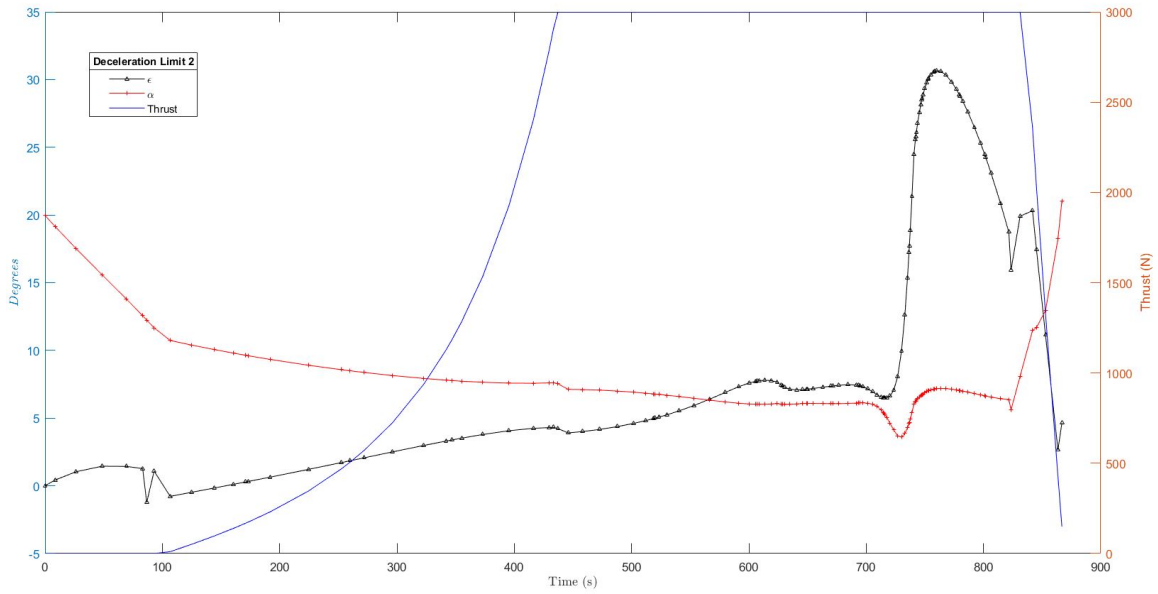
Figure 47. Thrust Vectoring Solution, $g_n = 2$

Table 15. Total Heat Load for Varying Deceleration limits

Starting Mass (kg)	Total Heat Load $\frac{MJ}{m^2}$
8 g	322.16
5 g	332.72
2 g	348.84

4.3.4   Study of Increasing the Allowable TAV Heating Rate

In this section, the allowable heating rate is progressively decreased down to 0.75 MW/m^{2}s while altering no other state or vehicle parameters. The inclination change difference from Case 1 to Case 9 is 7.7°. Shown in Fig. 48 the trajectories flatten as the heating rate constraint decreases which is a similar trend to increasing the allowable deceleration load constraint. In contrast, the heating rate limit constraint solution allows for a sharper dip at perigee than the deceleration cases. Figure 49 highlights how the inclination change is nearly asymptotic at the perigee point of the trajectory, but moves towards a more linear solution as the heating constraint decreases.

Figure 48.   Altitude Profile for Varying Heating Rate

Figure 49.   Inclination Change for Varying Heating Rate

78

4.3.5   Study of Decreasing TAVs Total Allowable Heat Load

Figure 50 demonstrates the optimal trajectory changes as the allowable total heat load decreases from 1000 to 100 MJ/m^2. Likewise, the time spent in the atmosphere decreases from 900 s for the upper heat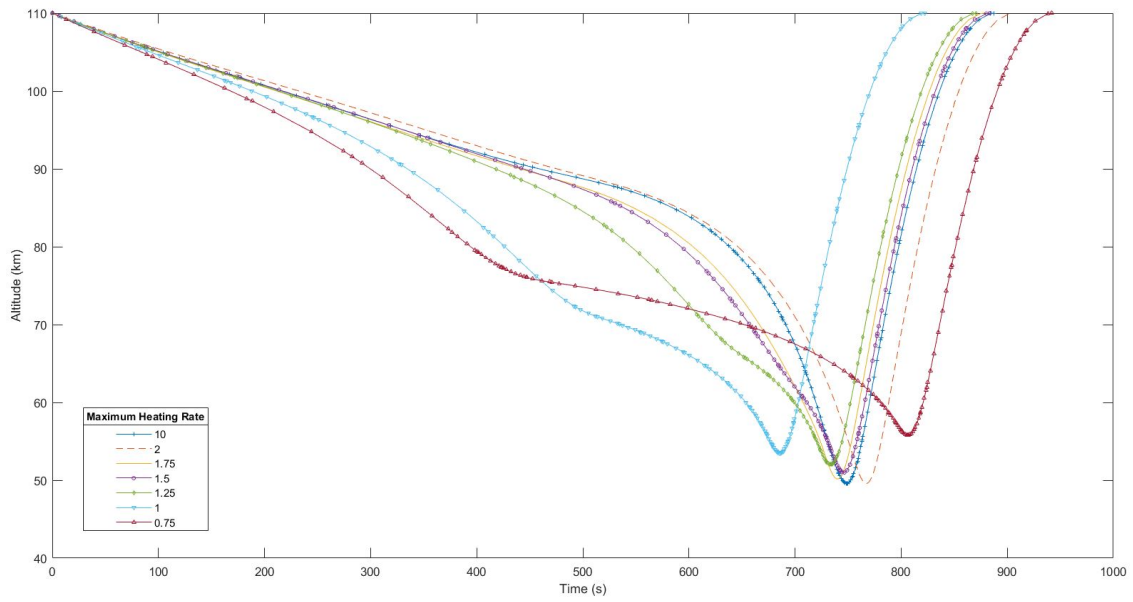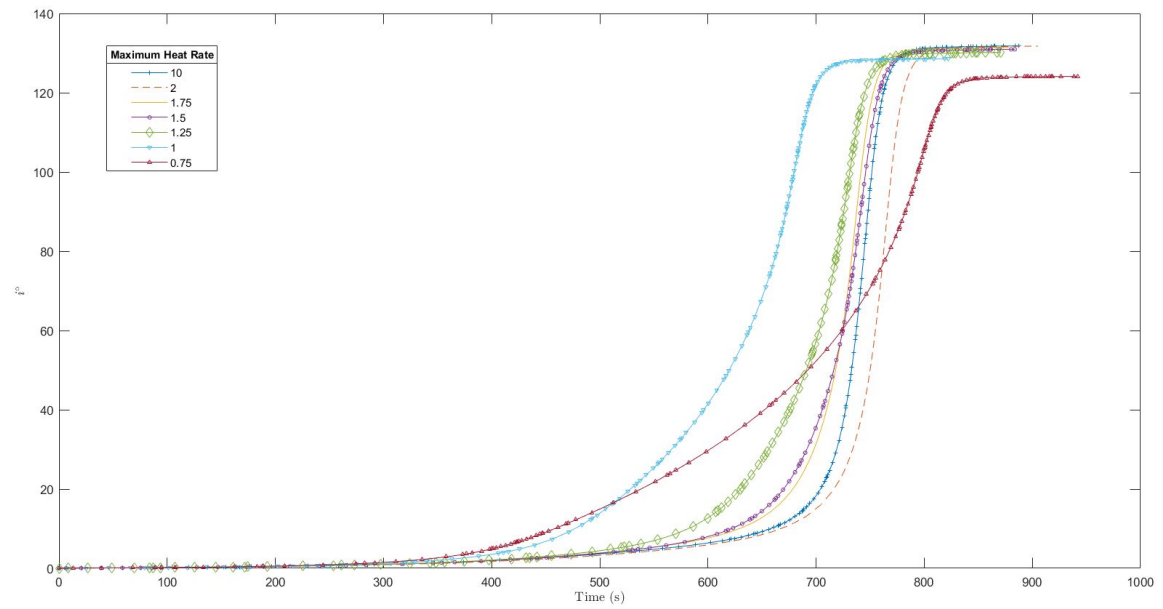 bound to 220 s for the lower heat bound. Table 16 shows the inclination changes, as well as the entry flight-path angle for each simulation studied. The flight-path angle increases sharply as the heating constraint is increased to allow a steep dive into the atmosphere. However, increasing the flight-path angle has draw backs for which the thrust vector compensates for. Figures 51 and 52 show how the thrust vector is used to augment lift during the steep dive observed in the most constrained case. In Fig. 52 the thrust vector behaves similarly to other cases, where the vector is not aligned with the longitudinal plane but still slightly in the direction of the lift vector. In the more constrained case, Fig. 51, the thrust vector increasingly points in the direction of lift until reaching a point close to perigee. At this location, it transitions to thrusting against the lift of the TAV before returning to a solution more closely aligned with the longitudinal plane. Besides this dramatic shift early in the trajectory this case represents the instance where the thrust vectoring solution comes closest to opposing the drag force almost exclusively.

Table 16. Final Inclination and Initial Flight-Path Angle for Varying Heat Load

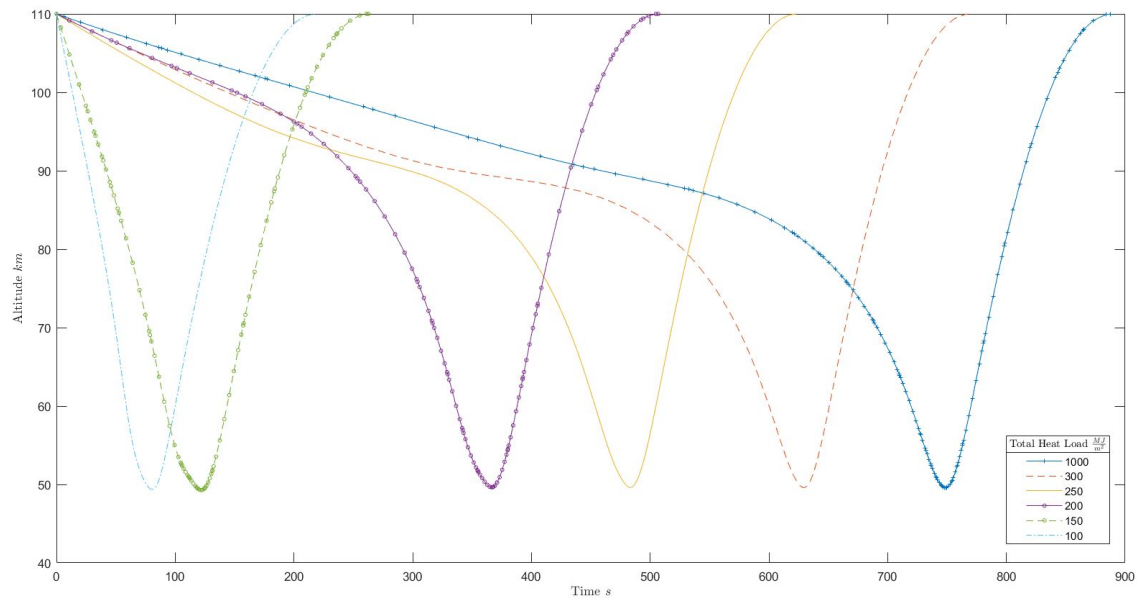| Heat Load $\frac{MW}{m^2}$	Δi_f°	Initial Flight-Path Angle$^\circ$
1000	131.8	-0.413
300	131.7	-0.570
250	130.7	-0.705
200	128.7	-0.595
150	123.9	-3.64
100	107.5	-5.75

Figure 50. Altitude Profile for Varying Total Heat Load
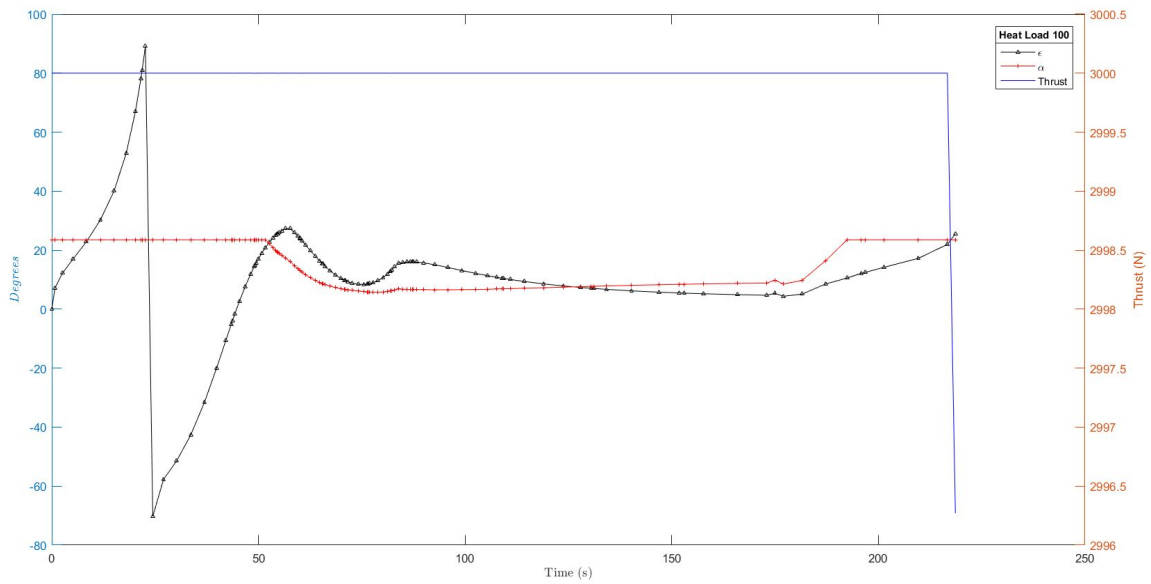

Figure 51. Thrust Vector Control for Varying Total Heat Load
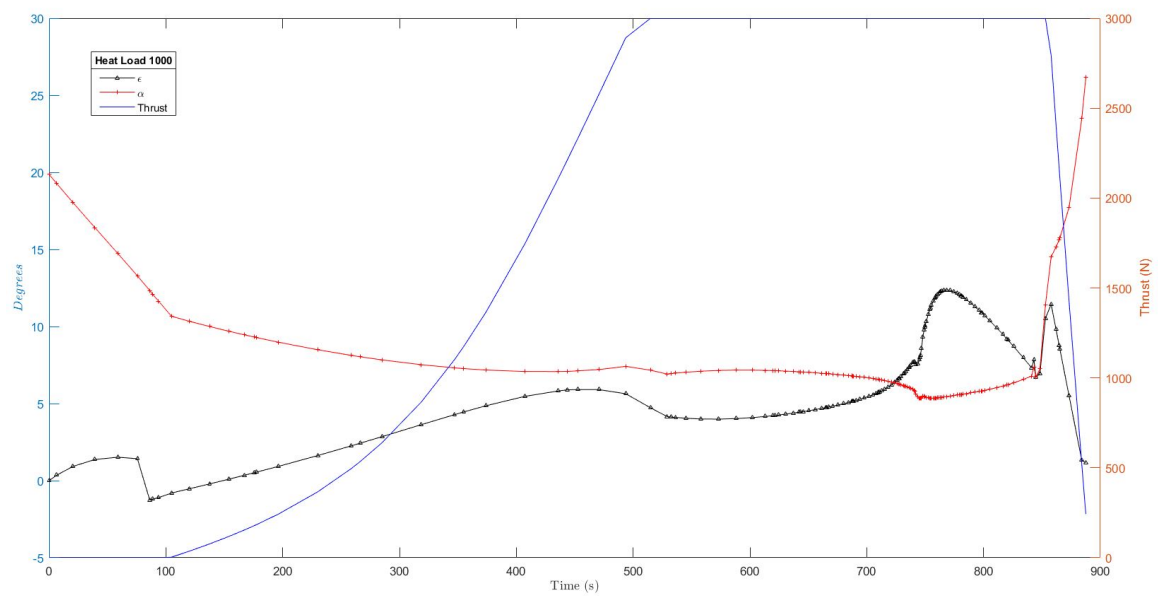
Figure 52.   Thrust Vector Control for Varying Total Heat Load

4.3.6 Study Increasing the Maximum Available Thrust of a TAV

The maximum thrust was varied between 500 N and 10000 N to understand the effects of increased thrust in the overall thrust vectoring solution. The difference in Δi between the lowest and highest maximum thrust case was $11.3°$. The primary advantage to increasing the thrust of a TAV is the amount of time required to complete the maneuver versus the inclination change available. The 500 N case took all 2000s to achieve a $\Delta i = 123.9°$ while the 10000 N case took just over 600s to achieve a $\Delta i = 132°$. Figure 53 depicts how increasing the thrust alters the trajectory from a solution that has two skips, to solutions with a single atmospheric dip, which takes place over shorter amounts of time. The solution for $f_{tmax} = 1000$ N is particularly interesting due to its distinctive skip.

A complete picture of the trajectory can be compiled from Figs. 54-57. Figure 54 shows the bank angle solution, while Fig. 55 gives the thrust vector angles, and angle-of-attack solution. The marked location on Fig. 54 indicates where the bank angle shifts from a left to a right bank. This appears on the graph to be a sudden change, but this is actually a smooth roll from left to right. In Fig. 55, the same location is marked which correlates to a shift in the in-plane thrust angle μ from port to starboard pointing. In Fig. 56, this takes place at the same time that the TAV is shifting from a left to a right bank. Referring back to Fig. 53, this shift occurs during the first skip through the atmosphere, before making a final dip into the atmosphere while thrusting to the starboard side of the TAV and banking right. This simulation shows how the optimal thrust vector solution for angle μ is in the direction of the atmospheric turn. This case was unusual, because of the shift in the bank angle from left to right, and it shows how the thrust vector makes a similar transition to aid in turning the spacecraft.
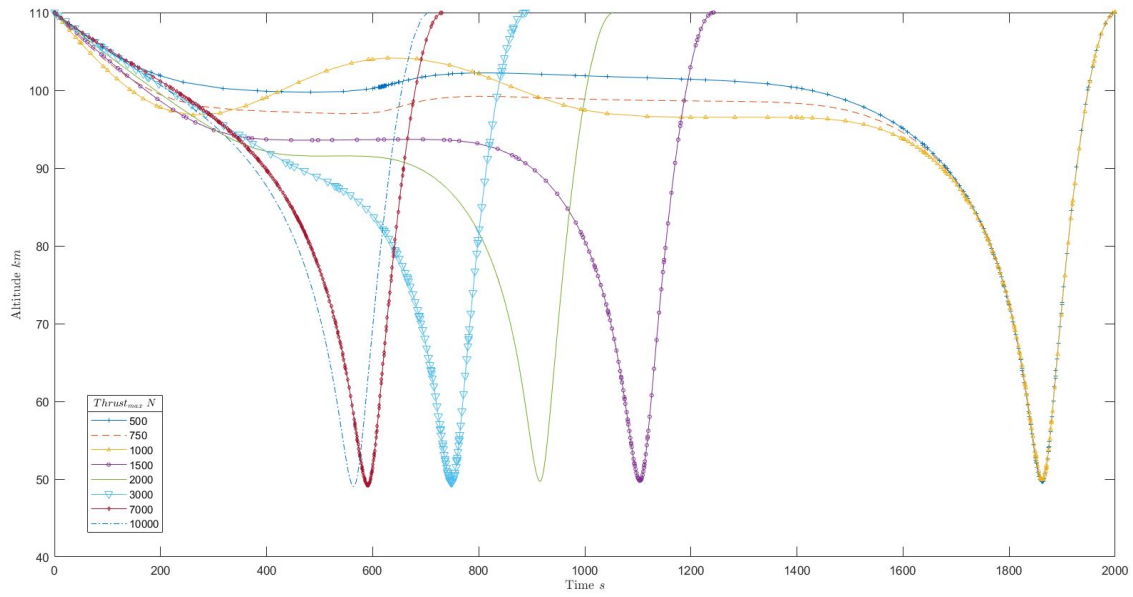
82

Figure 53. Altitude Profile for Varying Thrust Cases
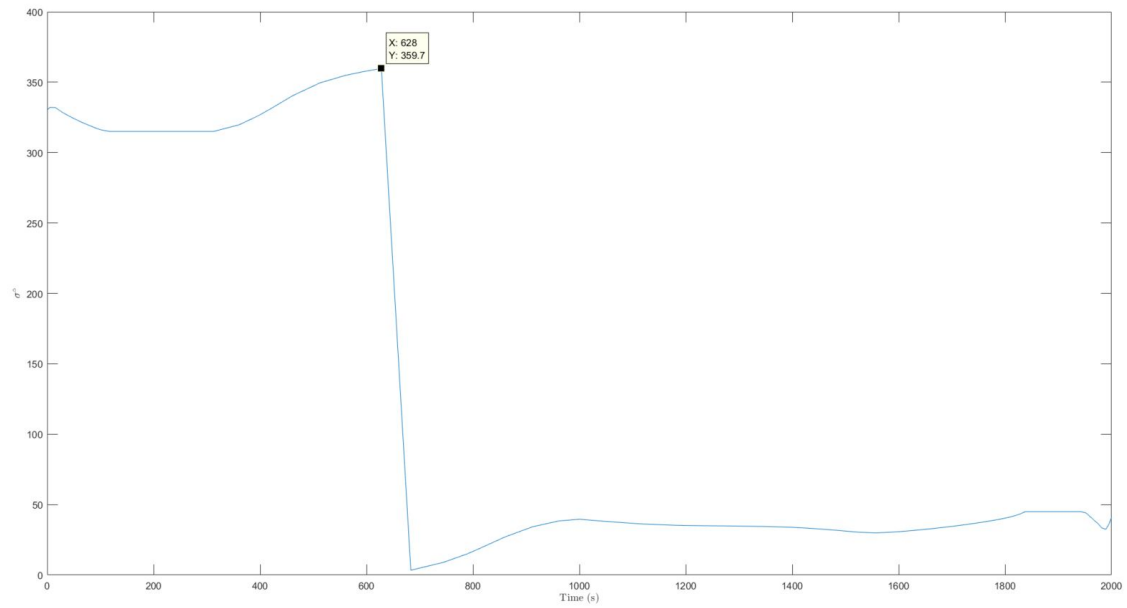

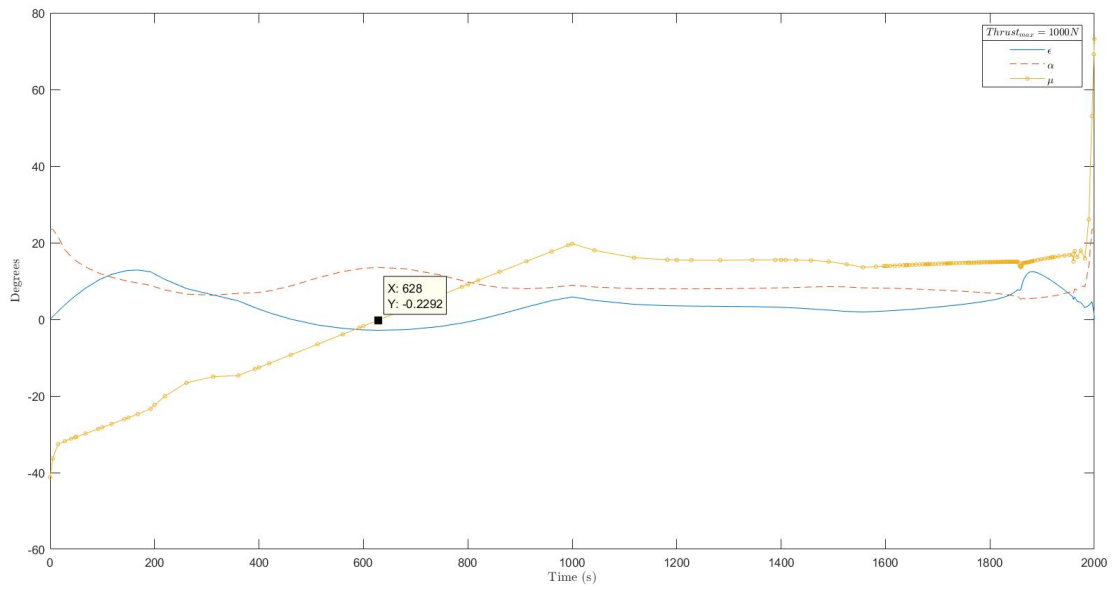**Figure 54. 1000 N Maximum Thrust: Bank Angle σ**

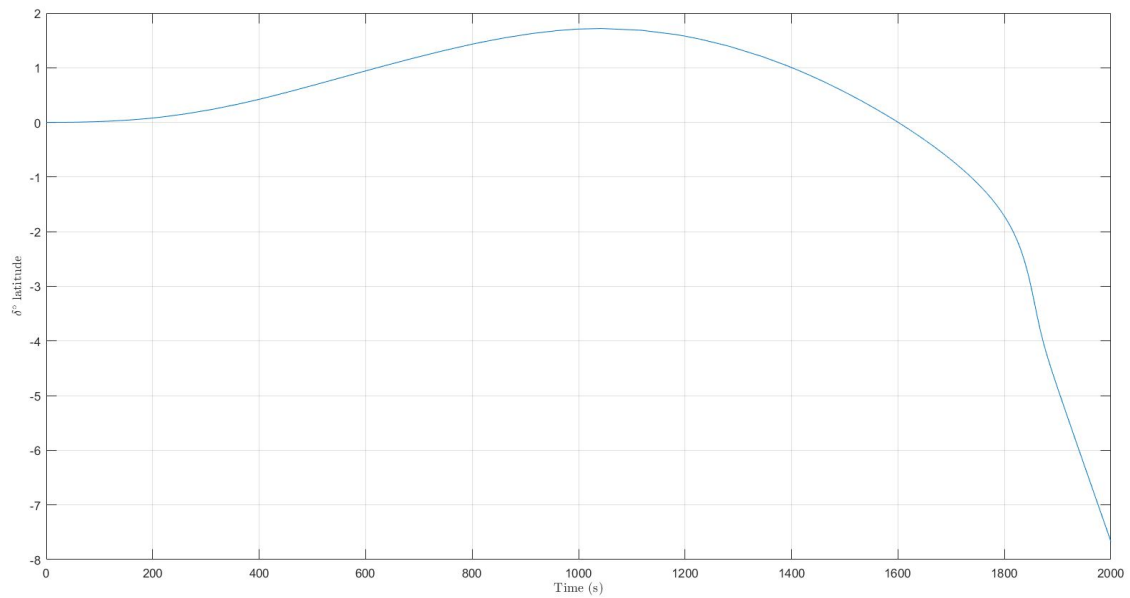**Figure 55.   1000 N Maximum Thrust: Thrust Angles**

Figure 56.   1000 N Maximum Thrust: Latitude vs. Time
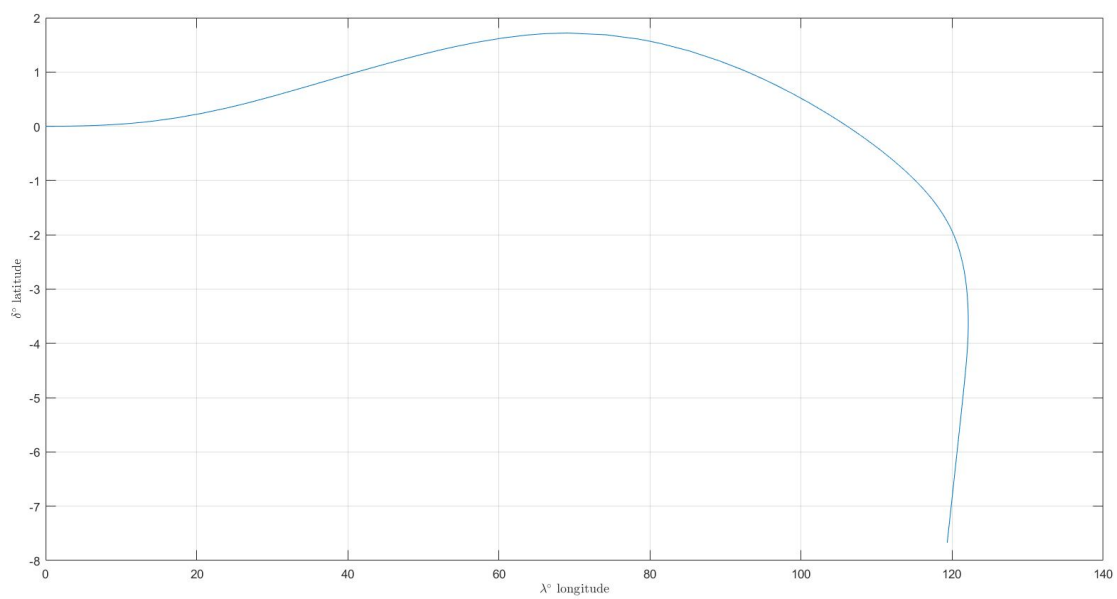
Figure 57.   1000 N Maximum Thrust: Latitude vs Longitude

4.3.7   Study of Increasing the Available Propellant Mass

The final parametric study focused on changing the available fuel mass of a TAV with an initial mass of 8500 kg. Figure 58 shows the trajectory for the all cases listed in the legend; however for, cases below 6900 kg the trajectories are indistinguishable, the reason for which can be found using Eqs. (4.1),(4.2),and (4.3). The amount of mass expended at maximum thrust for the 2000s time restriction of the problem is found to be 1973.0 kg which explains why the solutions are identical once the solution space has 2000 kg of available fuel mass.

$$V_{exit} = g_s I_{sp} \tag{4.1}$$

$$\dot{m} = \frac{f_T}{V_{exit}} \tag{4.2}$$

$$\dot{m} = \frac{m_0 - m_f}{t} \tag{4.3}$$

Where V_{exit} describes the exit velocity of a flow in an engine nozzle while the other variables have been defined previously.

Figure 60 depicts the out-of-place cant angle for the simulation with a fuel mass of 1400 kg. The thrust is plotted on the right y-axis so that the part of the solution which includes thrusting can be identified. It appears that ϵ initially peaks to $-60°$ shortly after the simulation begins, but after observing the thrust curve, it is shown that the thrust for the same portion of flight is zero. As a result this solution for ϵ does not have physical meaning for this portion of the trajectory. The TAV skips into the atmosphere twice for solutions greater than and equal to 1400 kg. In Fig. 60 the out-of-place cant angle is greater than the angle of attack at the local minimum of each dip into the atmosphere. Otherwise, the cant angle is below the angle of attack thus still positive and therefore contributing to the lift of the TAV. As observed in

the preceding cases, the out-of-place cant angle is relatively small for the majority of the solution. Figure 60 gives insight to how the thrust vector helps the TAV achieve the first skip, and how it then forces re-entry for the final skip.
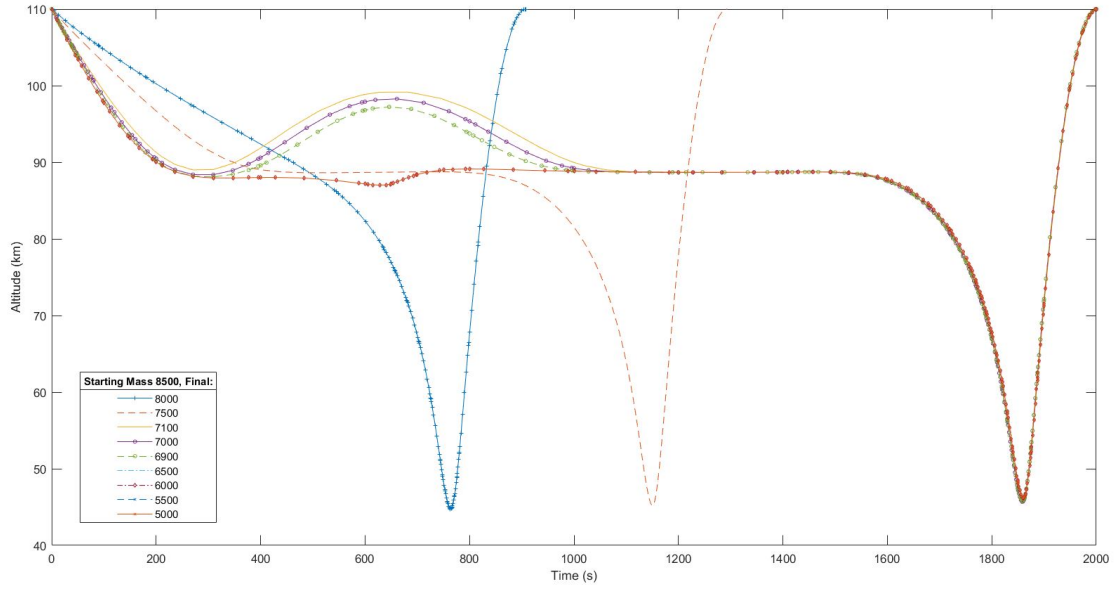

Figure 58.   Altitude Profile for Varying Fuel-to-Total Mass Ratios
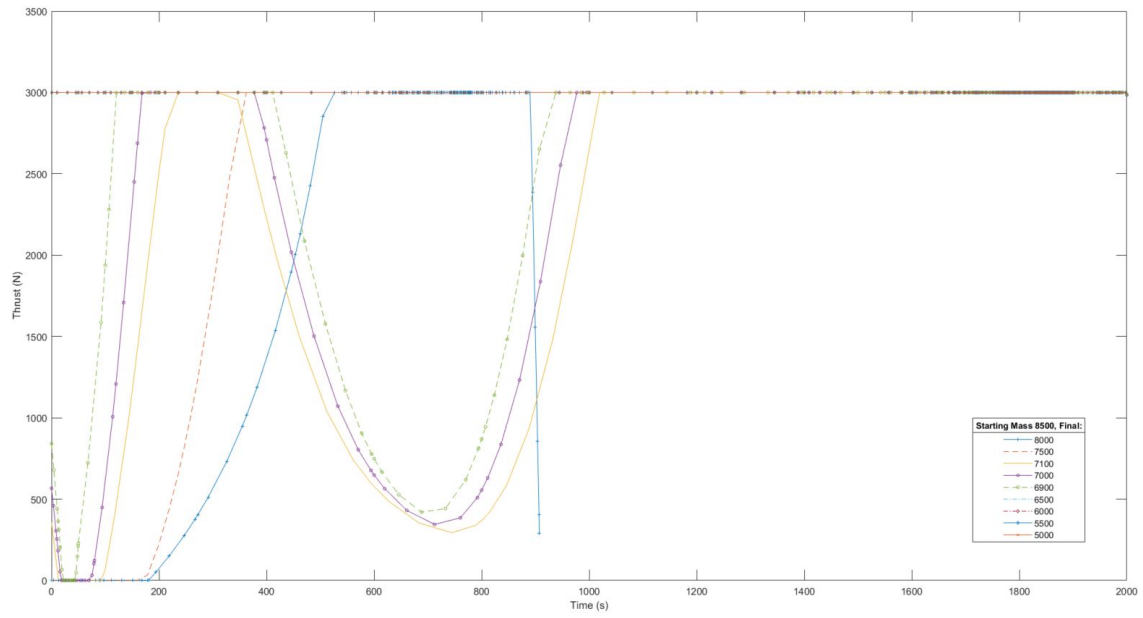
Figure 59.   Altitude Profile for Varying Fuel-to-Total Mass Ratios
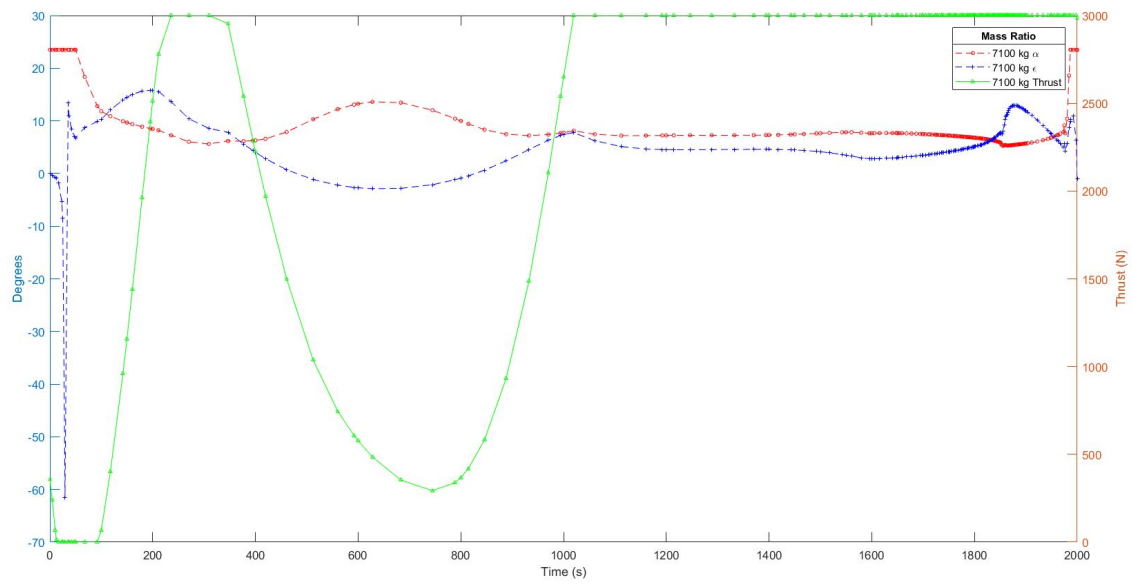
Figure 60.   Thrust Angles for 1400 kg Propellant Case

4.4 Exo-Atmospheric vs Thrust Vectoring Synergetic Maneuver: An X-34 Comparison

The aerodynamics of the X-34 TAV as been used throughout the present research. This section will seek to follow the TAV characteristics of the X-34 more closely so that a more realistic comparison can be made between an exo-atmospheric, and synergetic skip entry maneuver in order to change inclination. The X-34 TAV characteristics used in this simulation are given in Table 17 with the state constraints listed in Table 18. The results of this simulation will be compared to the simple plane change that is typically performed outside of the atmosphere, also referred to as exo-atmospheric maneuvers.

The exo-atmospheric maneuver can be calculated using equations from [27]. First, the ideal rocket equation can be implemented to calculate total ΔV capable of being produced by the X-34. Without making fuel efficiency a requirement of the objective function, it can be assumed that the simulation will produce a result that uses all of propellant available to the X-34. Here, the mass final is equal to the dry structural mass of the X-34, with $m_f = 8164.6627$ kg, and the initial mass is the propellant mass plus the structural mass, or $m_0 = 21772.434$ kg.

$$\Delta V = I_{sp}g_s \ln\left(\frac{m_0}{m_f}\right) = 2982.84\text{m/s} \tag{4.4}$$

The ΔV calculation using Eq.(4.4 can be used in the simple plane change equation to determine the Δi possible in the exo-atmosphere with the X-34.

$$\Delta i = 2\sin^{-1}\left(\frac{\Delta V}{2V_{orbit}}\right) \tag{4.5}$$

Using the circular velocity of 7.5 km/s corresponding to a radial orbit at 700 km, the inclination change possible is 22.94°.

Before a calculation can be performed using the synergetic skip entry model, a consideration of the ΔV required to de-orbit and re-circularize to the initial altitude must be computed. The entry velocity correlates to initial circular altitude 700 km, and the entry interface is assumed to equal 110 km. A Hohmann transfer can be used to approximate the ΔV needed to de-orbit, and to conservatively approximate the propellant mass that will be needed to re-establish a circular orbit at the initial altitude. Therefore, the initial and final masses that will be used are $m_0 = 19510$ kg and $m_{min} = 9111.274$ kg, respectively. From the thrust vectoring skip entry simulation, the final achievable inclination change is $51.24°$. Figure 61 shows the relationship between the trajectory profile and the Velocity, a value relative to a rotating reference frame. Overall, velocity can represent the amount of energy in the system, and the figure shows how this energy is depleted by skipping into the atmosphere.

A thrust vector analysis can be performed using Figs. 62-64. The resulting optimal solution is a turn toward the Southern Hemisphere as expected from the constraint and initial guess for azimuth. This turn correlates to a thrust vector solution that points in the direction of the bank. Figure 64 illustrates how ϵ is very high initially and primarily directed in the direction of lift. When thrusting continues after the dip through perigee, ϵ remains in the direction of lift but less so than before perigee. This solution differs from others studied because of the reduction in thrusting during the pass through perigee. This reduction is likely due to fuel mass constraints, and the increased weight of the spacecraft studied in this example compared to other simulations. The angle-of-attack α remains near the peak value for the duration of the flight which is equivalent to stating that the optimal solution is at C_{lmax}, a result observed by other research in literature.

Table 17. X-34 TAV Characteristics

Parameter	Value
Specific Impulse, I_{sp}	$310s$
Thrust, T	$268.927kN$
Deceleration Limit	2
Max Heating Load, q	$200\frac{MW}{m^2}$
Heating Rate Limit, $\dot{Q}$	2
Initial FPA, ϕ_0	$-2°$
Initial Velocity, V_0	$7.5\frac{m}{s}$
mass, m	$mass_{min} \leqslant m \leqslant mass_{max}$
Reference Area, S	$149.4m^2$

Table 18. X-34 Simulation State Constraints

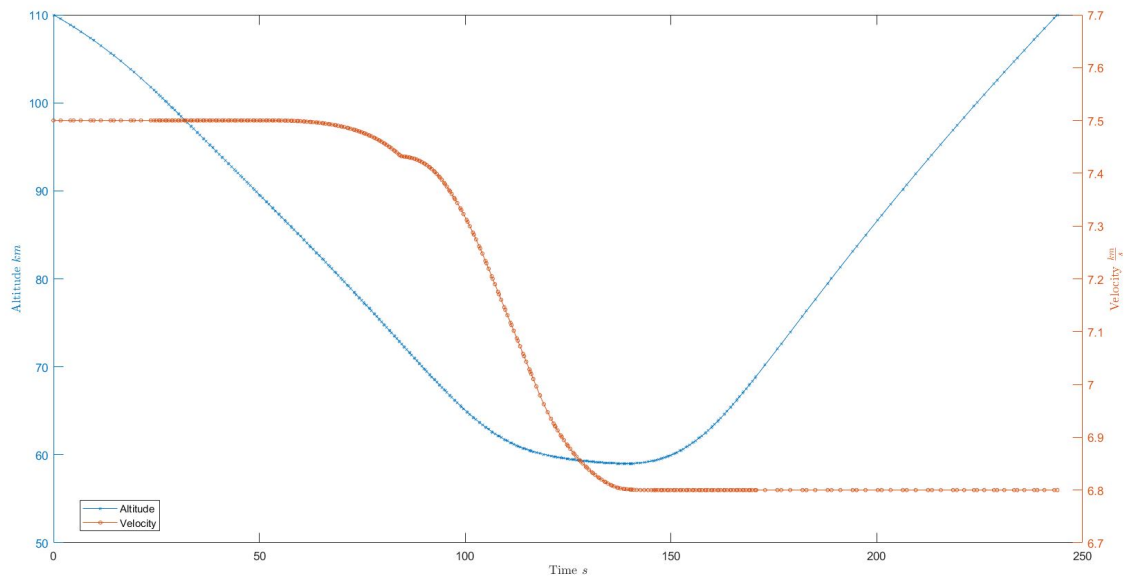| Parameter	Value
Position, r	$R_\oplus \leqslant r \leqslant 200(km)$
Velocity, V	$4 \leqslant V \leqslant 9(\frac{km}{s})$
Final Velocity, V_f,	$\geqslant 6.8\frac{km}{s}$
Flight Path Angle, ϕ	$-10° \leqslant \phi \leqslant 10°$
Azimuth, A	$0 \leqslant A \leqslant 2\pi$
latitude, δ	$-\frac{\pi}{2} \leqslant \delta \leqslant \frac{\pi}{2}$
longitude, λ	$0° \leqslant \lambda \leqslant 200°$
time, t	$0 \leqslant t \leqslant 2000s$

Figure 61. X-34 Simulation: Altitude and Velocity
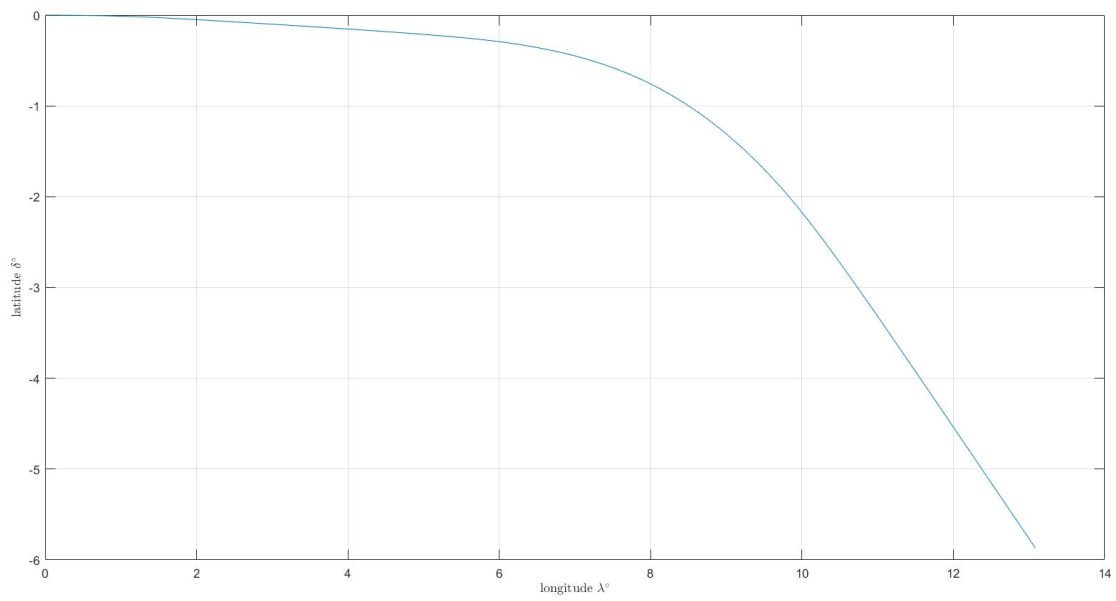

Figure 62. X-34 Simulation: Latitude vs Longitude
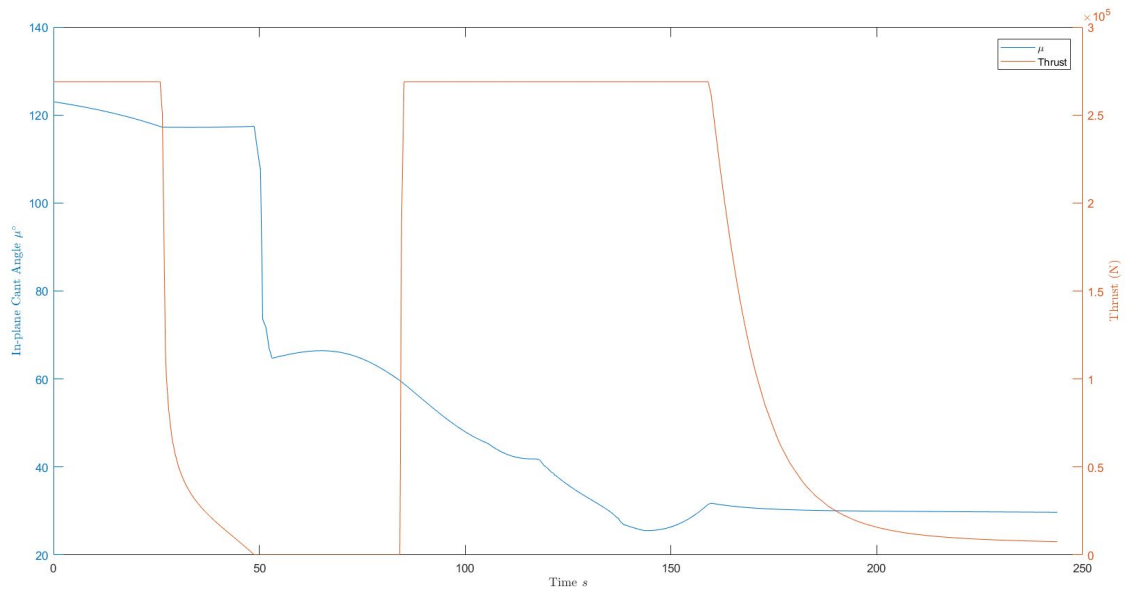
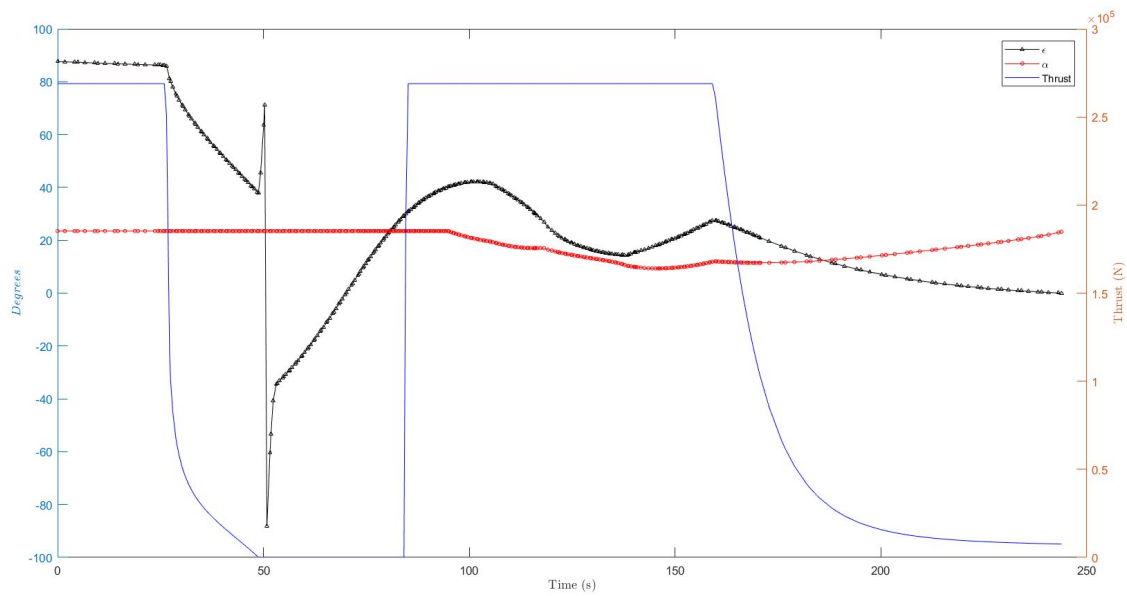**Figure 63. X-34 Simulation: In-Plane Cant Angle**

Figure 64. X-34 Simulation: Out-of-place Cant Angle and Angle of Attack

93

4.5 Optimization of the Synergetic Skip Entry with Constrained Dynamic Thrust Vectoring Control

To this point of the present research, the thrust vector controls have been unconstrained in the trajectory optimization with the objective to achieve the maximum inclination change. In previous sections, the thrust angle solutions have been compared to current TAV designs that restrict rear facing engine cant angles to minimal values. The current methodology must be refined to enable restriction of the thrust vector direction that would simulate current design limitations.

4.5.1 Methodology Alterations for the Constrained Thrust Vectoring Control Problem

It has been shown in [28] that "controls" may be included in the state vector X, while their derivative is captured as a control variable. Following this methodology, the state vector becomes $X = [r,\ V,\ \phi,\ A,\ \lambda,\ \delta,\ m,\ \epsilon,\ \mu,\ f_t]'$, and the control vector is, $u = [\dot{f_t},\ \dot{\epsilon},\ \dot{\mu}, u_4, u_5]'$. In this formulation the thrust vector control can be restricted by state constraints while their rates may be restricted by control constraints. By including f_t and $\dot{f_t}$ as a state and control, the thrust rate can be restricted resulting in smoother control solutions which realistically simulate engine throttle. To simulate small engine cant angles off the longitudinal plane a path constraint is used to limit the difference between ϵ and α. For comparison to the unconstrained solution, constraints from Case 4 in Sec. 4.2 will be used, which are repeated in Table 19.

4.5.2 Results and Analysis of the Constrained Thrust Vectoring Skip-Entry Problem

In Sec. 4.2, Case 4 achieved an $\Delta i = 125.1°$, while the constrained thrust vector solution achieved $\Delta i = 124.4°$. Figure 65 shows the constrained thrust vector solu-

tion where the solution has changed slightly from the unconstrained solution repeated in Fig. 66. In the first 200s the unconstrained ϵ solution was negative, similarly the constrained solution is at the lower bound at full throttle. After 200s the solutions are nearly identical. The optimal constrained solution does not begin throttling the engine until 9s into the flight in comparison which is the exact time that the ϵ solution in the unconstrained case reaches its lowest peak. Interestingly, the constrained solution had 170 kg of propellant mass at the end of the simulation due to this thrust delay and the shorter time-of-flight. In conclusion, the constrained case resulted in a 9% performance reduction since the available inclination change between the aeroglide and aerocruise was 8.6° and the simulations difference was .7°.

Table 19. Constrained Thrust Vector Simulation Parameters and Constraints

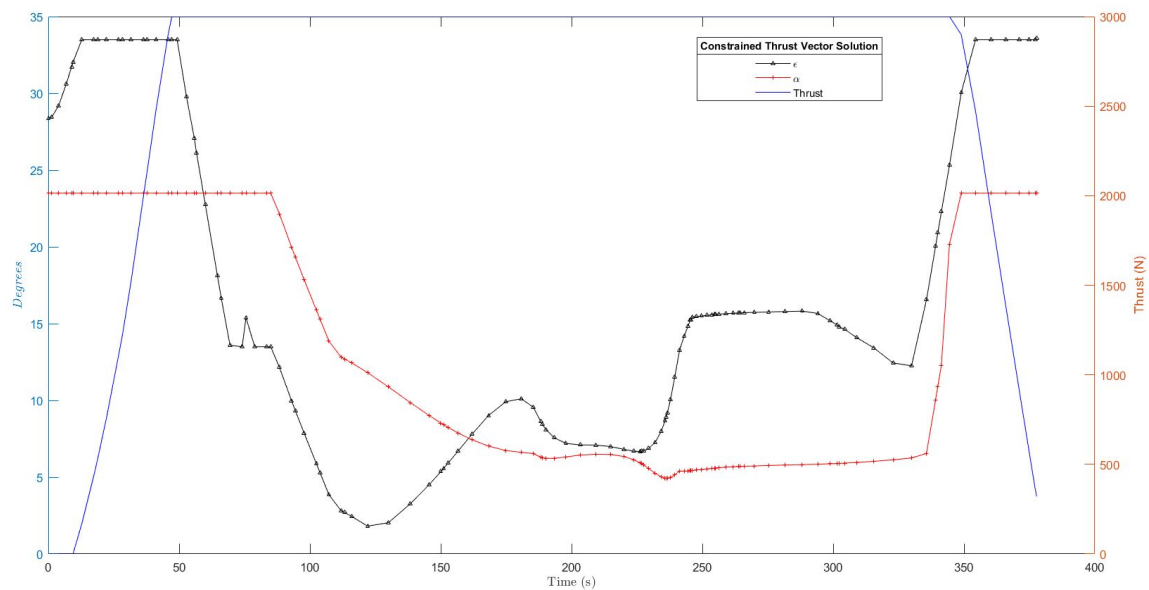| Parameter	Value
Heating Rate, $\dot{q}$	$2 \; \frac{MW}{m^2}$
Maximum Thrust, T_{max}	3000 N
Specific Impulse, I_{sp}	310 s
Heat Load, Q	$200 \; \frac{MJ}{m^2}$
Acceleration, a_{decel}	4 g_n
Propellant Mass,	500 kg
Vehicle Structural Mass,	4000 kg
Thrust Vector, μ	$-10° \leqslant \mu \leqslant 10°$
Thrust rate, $\dot{f}_t$	100 N
$\dot{\epsilon}, \dot{\mu}$	$-1° \leqslant \dot{\epsilon}, \; \dot{\mu} \leqslant 1°$
$\alpha - \epsilon$	+/- 10°

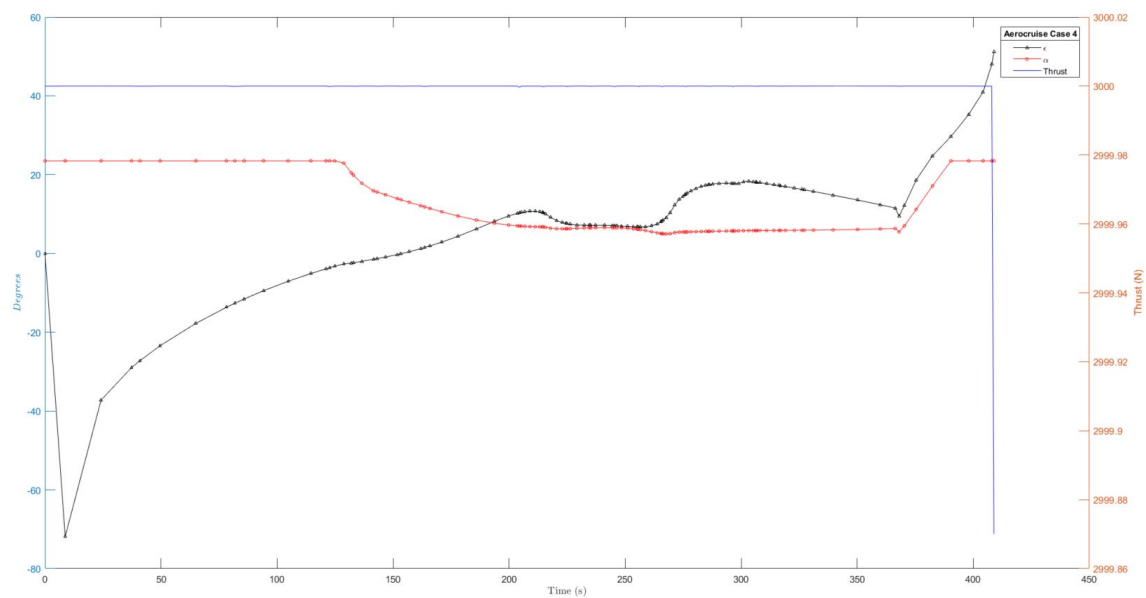**Figure 65. Constrained Thrust Vector Solution**

Figure 66. Unconstrained Thrust Vector Solution

96

4.6 Minimum Propellant Expenditure of the Constrained Dynamic Thrust Vectoring Skip-Entry

Using the modified control method established in the previous section, a minimum fuel solution can be simulated if a weighted objective functional as described by [15] is utilized. For this solution an endpoint function can be used to target a specific value for the final inclination that is reasonable to expect from the constraints placed on the vehicle. The objective function will be altered to find the minimal value of a weighted integral where the integrand is the thrust magnitude and the thrust vector angle derivatives described further in Eq. 4.6:

$$ J = \int_{t_0}^{t_f} W_1 f_t + W_2 \frac{1}{2}\dot{\epsilon}^2 + W_3 \frac{1}{2}\dot{\mu}^2 \tag{4.6} $$

Where, W_1=0.8, W_2=W_3=0.1. Including weights on $\dot{\epsilon}$ and $\dot{\mu}$ will help smooth the control solution while the weight from W_1 will ensure that the thrust magnitude is minimized thus limiting propellant expenditure. The minimum fuel solution of a skip-entry would involve some preservation of velocity in the atmosphere, therefore this case will limit the change of velocity in the atmosphere to 0.5 km/s. All other parameters for this simulation are consistent with Table 19, except that using the integral for the objective function prohibits limiting the total heat load.

Figure 67 illustrates the velocity loss, and trajectory for a minimum propellant expenditure case where $i_f = 20°$. From 4.2 it is known that the unconstrained thrust vector solution was able to achieve 23° of inclination change, so it is expected that 20° would consume nearly all of the propellant, or alter the trajectory. Here the proceeding is true, nearly all of the mass propellant was expended: 336.7 of 500 kg. Figure 68 illustrates the constrained thrust vector solution where μ is shown to be in the direction of the turn (towards the Southern Hemisphere) and at or near its

maximum bound for the duration of the thrust burn period between 100 and 650s. Out-of-plane thrust angle ϵ is not aligned with the longitudinal plane, but as seen before,ϵ is positive and increasing until reaching a maximum just after the perigee point. The constrained thrust vector minimum propellant simulation has again shown that, thrust vectoring is the optimal solution for synergetic skip entries.
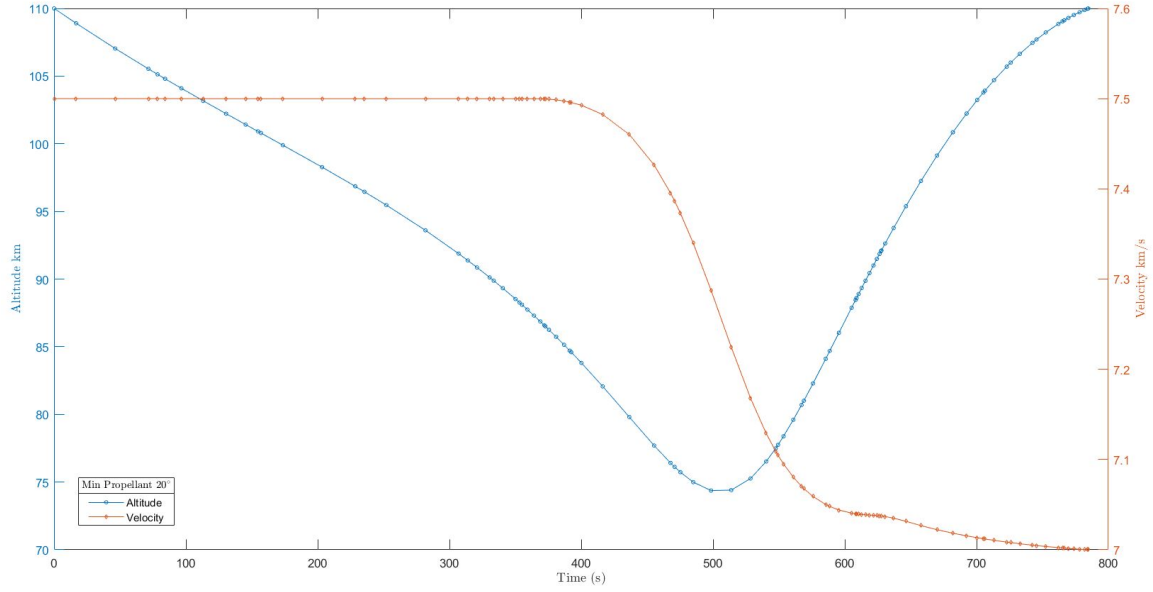
Figure 67. Minimum Propellant Expenditure: Altitude and Velocity
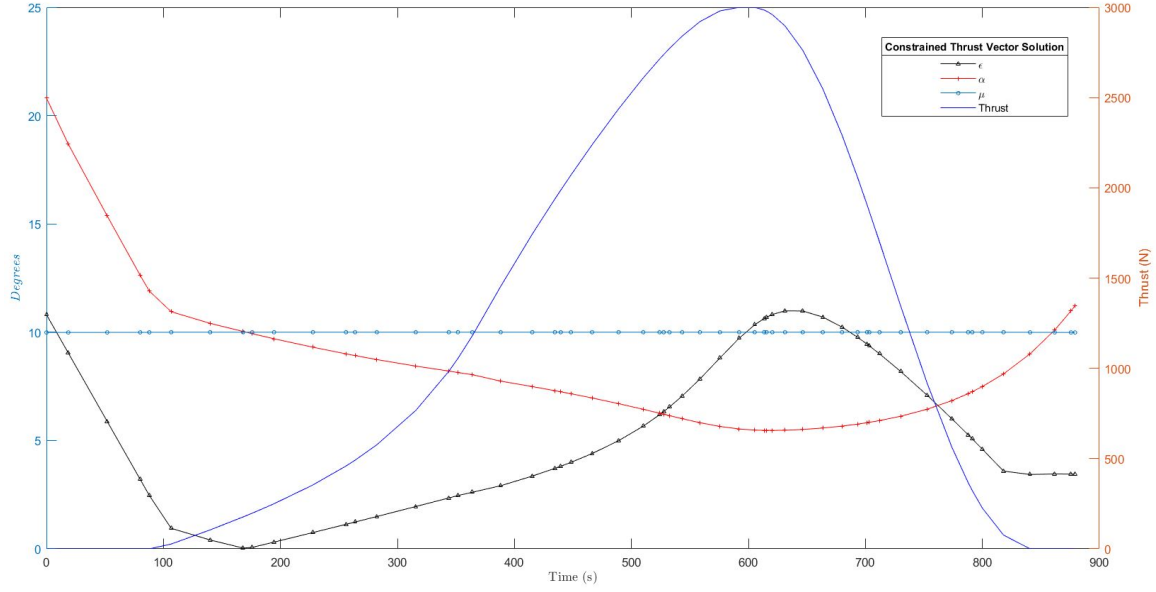
Figure 68. Minimum Propellant Expenditure: Thrust Vector Solution

4.7   Summary

In this chapter, the results and analysis of the thrust vectoring synergetic plane change skip entry was discussed for a variety of parametric cases. It has been shown that the aerocruise maneuver allows for a greater inclination change than the aeroglide maneuver, and that the optimal angle to thrust is not at an angle perfectly aligned with the drag vector. Through the X-34 simulation and various other parameter studies, it has also been determined that a small in-plane engine cant angles can achieve the optimal solution, but the unconstrained out-of-plane cant angle for the optimal solution is quite large compared to traditional TAV designs. When the thrust vector is constrained to a traditional design, performance dropped by 9% for the researched case.

99

V. Conclusions and Recommendations

5.1 Conclusions of Research

After verification of the EOM for atmospheric re-entry by simulation of the Apollo 10 capsule trajetory, the dynamics model was used in conjunction with the optimal control software GPOPS-II to optimize an aerocruise maneuver for maximum inclination change with the ability to use thrust vectoring. A comprehensive study of this problem was conducted to understand a wide range of parameters and their effects on the ability of a TAV to make rapid, dramatic changes to the inclination its orbit. In addition, the thrust vectoring aerocruise maneuver was compared to an un-powered aeroglide maneuver with the same objective. Results show that as expected powered flight achieved a greater inclination change due to thrust vectoring.

It was shown throughout the research that thrusting in the direction of drag was not the optimal solution. The out-of-plane cant angle ϵ is typically vectored $10°$ in the lift direction while the in-plane angle μ is typically more dramatic and in the direction of the atmospheric turn. It was shown that in certain conditions, the thrust vector could be used to add drag or increase the force towards the center of the Earth, for a more optimal solution. When compared to the aeroglide problem, a thrust vectoring aerocruise maneuver could increase the inclination change possible by an average of $10°$. When constraints on heating load, heating rate, and deceleration limits tightened, the inclination disparity increased between the two methods suggesting that TAV designs with lower tolerances could employ thrust vectoring to increase their effectiveness. Cases varying vehicle mass, fuel to mass ratio, specific impulse, heat load, heating rate, deceleration limits, and maximum thrust were studied. Various conclusions were developed through examination of these cases. First, increasing the maximum thrust was not shown to significantly increase the spacecraft's ability to

change inclination. Second propellant efficiency through variation of the specific impulse was shown to dramatically increase the overall inclination change. As expected, lighter vehicles were also capable of making greater inclination changes. Next, it was shown that limiting the deceleration naturally lowered the heating rate of the trajectory, and that deceleration limits as low as 2g's did not significantly impact performance. This is an important point for control surfaces that may be employed on TAVs that have low structural tolerances. The solution for the optimal path of a skip was highly dependent on a spacecraft's limiting physical conditions. For example, when the heat load was highly constricted or the maximum thrust greatly increased, a steep re-entry angle was desirable. Additionally, various situations arose where at least two skips in the atmosphere was deemed optimal. In situations of a fuel efficient or fuel heavy vehicles the solution resulted in one minor skip below 110 km before a more dramatic skip to end the trajectory.

Next a realistic case, using the X-34, of a thrust vectoring aerocruise was compared to an exo-atmospheric plane change where the difference in inclination change possible was $28.3°$. When observing the collective body of work herein, it can be definitively concluded that thrust vectoring atmospheric maneuvers are the superior method for changing the inclination of an orbiting TAV. This method, if properly considered, can dramatically alter the ability of TAVs to traverse the space domain, quickly, efficiently, and without the usual limitations of repeating orbital paths.

Finally, the thrust vector solution was constrained to be within common engine cant angle boundaries. In this study, including a minimum propellant case, it was shown that the optimal thrust vector solution is not in the direction opposite of the drag vector. Additionally, constraining the thrust vector had a negative impact on inclination change performance.

5.2 Significance of Research

Various improvements to previous research have been successfully implemented in this thesis. First and foremost, is the inclusion of in-and out-of-plane cant angles of the thrust vector in the problem, as well as the analysis of these angles to alter the direction of the thrust vector in the optimization of inclination change. This information can be utilized to re-approach the design of TAVs. It can also be utilized to understand how spacecraft not intended to conduct aeroassisted maneuvers may be able to traverse the Earth's atmosphere. Secondly, the dynamics model made few simplifications to describe re-entry dynamics:

- The rotation of the Earth was not ignored

- Earth's non-spherical shape was accounted for in the gravitational model to the fourth Jeffery constant

- The Aerodynamics model was extracted from a flight tested design where the directional variation to the body lift and drag forces was simulated by the angle-of-attack

Additionally, all controls considered (μ, ϵ, f_t, σ, α) are dynamically optimized in the solution. Rather than comparing a few cases, this research sought to be comprehensive, by including realistic case variation, and documenting trends of solutions so that future designs may understand various trade spaces in the design phase of development.

5.3 Recommendations for Future Work

Various avenues for future development in this field may be taken:

- Development of a study that more closely considers the ability of a more traditional satellite (i.e., non-spaceplane vehicle) to achieve a synergetic skip entry. This consideration may feature a lower lift coefficient, higher drag coefficients, and the utilization of thrust vectoring to augment low lift.

- A closer development of TAV design may certainly be considered. The present research does not attempt to prescribe how a vehicle may physically achieve results described. For example, is it possible to bank a TAV travelling 7.5 km/s? Discarding the point mass assumption of this problem is also necessary to determine whether such trajectory designs are practical.

- The objective function of this research focused on changing orbital inclination. Development of a weighted objective function to reduce propellant expenditure as in Sec. 4.6 may be researched more thoroughly. This type of research could be combined with various mission targets and answer questions concerning time of orbital availability solved using a thrust vectoring method.

Bibliography

[1] "Pathfinder Program X-37 Flight Experiment," 2004.

[2] W. J. Broad and D. E. Sanger, "Flexing Muscle, China Destroys Satellite in Test - The New York Times," 2007.

[3] K. D. Scott, "Joint Publication 3-14 Space Operations," tech. rep., Joint Chiefs of Staff, 2018.

[4] D. Gonzales, M. Eisman, C. Shipbaugh, T. Bonds, and A. T. Le, "Proceedings of the Rand Project Air Force Workshop on Transatmospheric Vehicles," 1997.

[5] H. S. London, "Change of Satellite Orbit Plane by Aerodynamic Maneuvering," *Journal of Aerospace Sciences*, vol. 29, pp. 323–332, 1962.

[6] G. D. WALBERG, "A survey of aeroassisted orbit transfer," *Journal of Spacecraft and Rockets*, vol. 22, no. 1, pp. 3–18, 1985.

[7] E. Dickmanns, "NASA TN- The Effect of Finite Thrust and Heating Constraints on The Synergetic Plane Change Maneuver for a Space Shuttle Orbiter-Class Vehicle.pdf," 1973.

[8] M. ROESSLER, "Optimal aerodynamic-propulsive maneuvering for the orbital plane change of a space vehicle.," *Journal of Spacecraft and Rockets*, vol. 4, no. 12, pp. 1678–1680, 1967.

[9] N. X. Vinh and D. M. Ma, "Optimal multiple-pass aeroassisted plane change," *Acta Astronautica*, vol. 21, no. 11-12, pp. 749–758, 1990.

[10] R. A. Bettinger and J. T. Black, "Comparative Study of Phasing, Atmospheric Skip Entry, and Simple Plane Change Maneuvers," *Journal of Spacecraft and Rockets*, vol. 51, no. 6, pp. 1965–1975, 2014.

[11] A. V. Rao, S. Tang, and W. P. Hallman, "Numerical optimization study of multiple-pass aeroassisted orbital transfer," *Optimal Control Applications and Methods*, vol. 23, no. 4, pp. 215–238, 2002.

[12] A. V. Rao, "A SURVEY OF NUMERICAL METHODS FOR OPTIMAL CONTROL," in *AAS/AIAA Astrodynamics Specialist Conference, AAS Paper 09-334*, (Pittsburgh, PA), 0.

[13] M. A. Patterson and A. V. Rao, "GPOPS II : A MATLAB Software for Solving Multiple-Phase Optimal Control Problems Using hp -Adaptive Gaussian Quadrature Collocation Methods and Sparse Nonlinear Programming," vol. 41, no. 1, 2014.

[14] M. A. Patterson and A. V. Rao, "GPOPS-II manual: A General-Purpose MAT-LAB Software for Solving Multiple-Phase Optimal Control Problems Version 2 . 1," no. December, pp. 1–72, 2016.

[15] A. Shirazi, J. Ceberio, and J. A. Lozano, "Spacecraft trajectory optimization: A review of models, objectives, approaches and solutions," *Progress in Aerospace Sciences*, vol. 102, no. August, pp. 76–98, 2018.

[16] R. Detra, N. Kemp, and F. Riddell, "Addendum to Heat Transfer of Satellite Vehicles Re-entering the Atmosphere," *Jet Propulsion*, vol. 27, no. 1, pp. 1256–1257, 1957.

[17] R. Fuhr and A. V. Rao, "Minimum-Fuel Low-Earth Orbit Aeroglide and Aerothrust Aeroassisted Orbital Transfer Subject to Heating Constraints," *2018 Space Flight Mechanics Meeting*, no. January, pp. 1–43, 2018.

[18] A. Tewari, "Atmospheric and Transatmospheric Trajectories," in *Atmospheric and Space Flight Dynamics*, ch. 12, pp. 283–294, New York: Birkhauser, Boston, 1st ed., 2007.

[19] A. Tewari, "Planetary Form and Gravity," in *Atmospheric and Space Flight Dynamics*, ch. 3, pp. 45–56, New York: Birkhauser, Boston, 1st ed., 2007.

[20] "U.S Standard Atmosphere 1976," tech. rep., Committee on Extension to the Standard Atmosphere (COESA), U.S Government Printing Office, Washington D.C, 1976.

[21] A. Tewari, "Planetary Atmosphere," in *Atmospheric and Space Flight Dynamics*, ch. 9, pp. 223–231, New York: Birkhauser, Boston, 2007.

[22] D. Szelc, ""Apollo 10 Entry Postflight Analysis" NASA MSC Internal Note NO.69-FM-283 (MSC-00126 Supplement 10)," tech. rep., NASA, 1969.

[23] ""Apollo 10 Mission Report" Manned Spacecraft Center Report MSC-00126," tech. rep., National Aeronautics and Space Administration, 1969.

[24] K. D. Hicks, *Introduction to Astrodynamic Re-Entry*. Lexington, KY: CreateSpace, second ed., 2014.

[25] K. D. Hicks, "Introduction to Astrodynamic Re-Entry," in *Introduction to Astrodynamic Re-Entry*, ch. 12, pp. 321–356, CreateSpace, second ed., 2014.

[26] C. Weiland, *Aerodynamic Data of Space Vehicles*. Springer-Verlag Berlin Heidelberg, 1st editio ed., 2014.

[27] W. E. Wiesel, "Spaceflight Dynamics," in *SpaceFlight Dynamics*, ch. 3.5, pp. 86–91, Beavercreek Ohio: Aphelion Press., second ed., 2010.

[28] E. R. Prince, *Optimal Finite Thrust Guidance for Constrained Satellite Proximity Operations Inspection Maneuvers*. PhD thesis, Air Force Institute of Technology, 2018.

Vita

1st Lieutenant Jeremiah M. Webb graduated Robert S. Alexander High School in Douglasville, Georgia in May 2010. He was awarded a prestigious scholarship from the United States Air Force to attend the University of Alabama (Tuscaloosa, AL) College of Engineering. Where he studied Aerospace Engineering, and graduated in May 2015 with a Bachelor of Science. Upon graduating he received a Regular Commission in USAF and relocated to his first assignment at Los Angeles Air Force Base (LAAFB). Lt Webb was assigned to the Launch Enterprise Directorate of the Space and Missiles Systems Center as a Structural Engineer on the United Launch Alliance Delta IV Evolved Expendable Launch Vehicle. After a brief two year stint at LAAFB, he entered the Graduate School of Engineering and Management, Air Force Institute of Technology (AFIT). Following completion of the Astronautical Engineering Masters program he will be assigned to the National Air and Space Intelligence Center (NASIC) for a three year assignment.